Ultrafast Laser Spectroscopy of Vibrational Energy Transport in Biomolecular Chains

---

Dissertation
zur
Erlangung der naturwissenschaftlichen Doktorwürde
(Dr. sc. nat.)

vorgelegt der
Mathematisch-naturwissenschaftlichen Fakultät
der
Universität Zürich

von
Marco Schade
aus
Deutschland

Promotionskomitee
Prof. Dr. Peter Hamm (Vorsitz)
Prof. Dr. Jürg Hutter
Prof. Dr. Stefan Seeger

Zürich, 2012

„Je planmäßiger die Menschen vorgehen,
desto wirksamer vermag sie der Zufall zu treffen.“

21 Points to *The Physicists*
Friedrich Dürrenmatt, Swiss author and dramatist (1921-1990)

List of Publications

Parts of the results of this thesis have been published in the following articles:

Journal Publications

- M. Schade and P. Hamm.
  Transition from IVR limited vibrational energy transport to bulk heat transport.
  Chem. Phys. **393**, 46-50 (2012).
- M. Schade, A. Moretto, P. M. Donaldson, C. Toniolo, and P. Hamm.
  Vibrational energy transport through a capping layer of appropriately designed peptide helices over gold nanoparticles.
  Nano Lett. **10**, 3057-3061 (2010).
- M. Schade, A. Moretto, M. Crisma, C. Toniolo, and P. Hamm.
  Vibrational energy transport in peptide helices after excitation of C-D modes in Leu-d_{10}*.*
  J. Phys. Chem. B **113**, 13393-13397 (2009).
- M. Schade and P. Hamm.
  Vibrational energy transport in the presence of intrasite vibrational energy redistribution.
  J. Chem. Phys. **131**, 044511 (2009).

Conference Proceeding

- M. Schade, P. M. Donaldson, E. H. G. Backus, A. Moretto, C. Toniolo, and P. Hamm.
  Vibrational energy transport in peptides.
  In M. Chergui, D. Jonas, E. Riedle, R. Schoenlein, and A. Taylor (Eds.), *Ultrafast Phenomena XVII*, pp. 538-540, Oxford University Press, New York (2011).

Contents

Abstract

The aim of this thesis was to investigate the vibrational energy transport properties of biomolecular chains, such as peptides and proteins. For this purpose, a combined approach of femtosecond infrared spectroscopy and numerical simulations was applied. Simulation studies were performed on a simple toy model mimicking the normal mode distribution of proteins. Vibrational energy was deposited into one site of the linear chain, and its flow through the system directly calculated as a function of time. Experimentally, the same concept was realized by using different ultrafast local heaters, which – upon excitation with femtosecond laser radiation – release vibrational excess energy at one defined site of a short peptide helix. The subsequent appearance of vibrational energy at any distant site of the molecular chain was detected by using isotope labeled carbonyl groups in the peptide backbone as local thermometers.

It was shown that the mechanism of vibrational energy transport – on length scales of a few chemical bonds and time scales of a few picoseconds – is distinctively different from heat diffusion on macroscopic scales, because energy does not thermalize completely within individual amino acid sites on the time scale of transport. This finding is the key to understanding several experimental observations, and also provides a guideline for how to modify molecular dynamics simulations to reproduce experimental findings. Fully deuterated leucine was introduced as a novel local heater, releasing a low amount of excess energy by vibrational relaxation of its side-chain carbon-deuterium modes. Vibrational energy propagation after excitation of the C–D modes was found to be diffusive; the measured heat diffusion constant of ≈ 2 Å^{2}ps^{-1} is in agreement with the result obtained after high-energy excitation of an azobenzene chromophore (Botan *et al.*, PNAS, **104**, 12749-12754 (2007)), showing that the linearity of vibrational energy diffusion is maintained over a wide range of initial temperature gradients. As another novel and very efficient local heating mechanism, plasmonically heated gold nanoparticles were used to initiate vibrational energy transport along biomolecular chains, again revealing a diffusive propagation process. This experiment, at the same time, demonstrates a new method for measuring the rates and efficiencies of energy flow across organic capping layers over nanoparticles; capping layers applied to small metal cores cool faster. To extend the underlying experimental concept to proteins folding into a tertiary structure, the 36-residue villin headpiece was chosen as a model system. In a preparatory study, cysteine-containing mutants of this protein were linked to either a water-soluble azobenzene chromophore or a spherical gold nanoparticle, and the response of the amide I band upon ultrafast laser excitation was observed.

In conclusion, the experimental and theoretical studies presented in this thesis have contributed to a better understanding of vibrational energy transport in biomolecular chains. Several open questions and apparent contradictions have successfully been resolved, leading to a unified picture of the topic.

Zusammenfassung

Das Ziel dieser Arbeit war es, die Eigenschaften des Transports von Schwingungsenergie in biomolekularen Ketten wie Peptiden und Proteinen zu untersuchen. Zu diesem Zweck wurde ein kombinierter Ansatz bestehend aus Femtosekunden Infrarotspektroskopie und numerischen Simulationen gewählt. Simulationsstudien wurden an einem einfachen Spielzeugmodell durchgeführt, das die Normalmodenverteilung von Proteinen nachahmt. Schwingungsenergie wurde an einer Stelle der linearen Kette eingebracht und der anschließende Fluss durch das System direkt als Funktion der Zeit berechnet. Experimentell wurde das gleiche Konzept mit verschiedenen lokalen Heizern realisiert, die – nach Anregung mit Femtosekunden Laserstrahlung – Schwingungsenergie an einer definierten Stelle einer kurzen Peptidhelix freisetzen. Das darauffolgende Auftreten der Schwingungsenergie an verschiedenen Stellen der molekularen Kette wurde mit Hilfe von isotopenmarkierten Carbonylgruppen in der Peptidhauptkette detektiert, die als lokale Thermometer fungieren.

Es wurde gezeigt, dass sich der Transport von Schwingungsenergie auf der Längenskala von wenigen chemischen Bindungen und der Zeitskala von wenigen Pikosekunden, deutlich von Wärmeleitung auf makroskopischer Skala unterscheidet, weil die Schwingungsenergie einzelner Aminosäuren auf der Zeitskala des Transports nicht thermalisiert. Dieses Ergebnis bietet die Grundlage für das Verständnis vieler experimenteller Beobachtungen, und zeigt gleichzeitig auf, wie Molekulardynamik-Simulationen angepasst werden müssen um experimentelle Ergebnisse reproduzieren zu können. Volldeuteriertes Leucin wurde als neuer lokaler Heizer eingeführt, der eine geringe Menge Überschussenergie durch Relaxation seiner Kohlenstoff-Deuterium Seitenketten freisetzt. Die Propagation von Schwingungsenergie nach Anregung dieser C–D Moden verläuft diffusiv; die gemessene Wärmediffusivität (auch Temperaturleitfähigkeit) von ≈ 2 Å^{2}ps^{-1} stimmt mit dem Ergebnis überein, das nach hochenergetischer Anregung eines Azobenzol Farbstoffs gemessen wurde (Botan *et al.*, PNAS, **104**, 12749-12754 (2007)), was zeigt, dass die Linearität der Schwingungsenergiediffusion über einen weiten Bereich von anfänglichen Temperaturgradienten erhalten bleibt. Als weiterer neuer und sehr effizienter lokaler Heizmechanismus wurden plasmonisch geheizte Gold Nanopartikel verwendet um den Transport von Schwingungsenergie entlang molekularer Ketten auszulösen; der folgende Propagationsprozess war wiederum diffusiv. Gleichzeitig demonstriert dieses Experiment einen neuen Ansatz zum Vermessen der Raten und Effizienz des Energieflusses durch organische Deckschichten auf Nanopartikeln; Deckschichten, die auf kleinere Metallkerne aufgebracht sind kühlen schneller. Um das zugrunde liegende experimentelle Konzept auf Proteine zu erweitern, die in eine Tertiärstruktur falten, wurde das sogenannte „villin headpiece“ bestehend aus 36 Aminosäuren als Modellsystem ausgewählt. In einer Vorstudie wurden Cystein enthaltende Mutanten dieses Proteins mit einem wasserlöslichen Azobenzol Farbstoff bzw. einem kugelförmigen Gold Nanopartikel gekoppelt, und das Verhalten

des Amid I Bands nach ultraschneller Laseranregung beobachtet.

Zusammenfassend haben die experimentellen und theoretischen Studien, die in dieser Arbeit präsentiert wurden, zu einem besseren Verständnis des Transports von Schwingungsenergie in biomolekularen Systemen beigetragen. Viele offene Fragen und scheinbare Widersprüche konnten gelöst werden, was zu einem vereinheitlichten Bild des bearbeiteten Themas geführt hat.

Chapter 1

Introduction

Proteins are molecular machines, which can efficiently convert chemical energy into useful work. As such, the structure of a protein is not static but dynamical, undergoing rapid conformational changes. The fundamental process linking the structure and dynamics of a protein to its function is vibrational energy transport [1]. Therefore, developing a microscopic picture of vibrational energy flow in biomolecules is the ultimate step for understanding, and possibly also controlling, protein dynamics and function [2].

The interplay between protein structure and functionality has been discussed for several decades; a special focus has been on the role of secondary structure motifs such as α-helices or β-sheets, both of which are stabilized by hydrogen bonds. In this context, a particularly interesting idea that has stimulated many debates in the biophysical community is the Davydov soliton. In the 1970s, Davydov suggested that vibrational solitons could propagate along the self-trapped C=O vibrations of α-helices, thus efficiently channeling vibrational energy through proteins [3]. Indeed, vibrational self-trapping in α-helices has meanwhile been directly observed in experiment [4]. However, the lifetime of these vibrational excitations was found to be on the picosecond time scale, which is too short to be of any biological relevance, at least in the sense of Davydov's initial proposal [5].

The role of specific vibrational energy transport pathways in proteins is often discussed in the context of allostery. Allostery is a concept that describes the coupling of conformational changes between two physically separated sites of a protein. As such, allosteric regulation is a fundamental process responsible for signaling in biological systems, and the hypothesis is that the underlying communication process is mediated by exchange of vibrational energy [6]. One example for the close relation between both phenomena are the communication pathways between active and distant sites, which Lockless and Ranganathan traced by applying evolutionary sequence analysis to proteins belonging to the so-called PDZ family [7]. Interestingly, using nonequilibrium molecular dynamics (MD) simulations for calculating the preferred channels of vibrational energy transport, a very similar connection was later found by Ota and Agard [8]. More recently, Sharp and Skinner [9] even identified a pathway along the very same amino acids as Lockless and Ranganathan. Hence, there must exist some kind of inherent connection between vibrational energy transport and specific allosteric communication channels in proteins. However, as already indicated above, vibrational energy in disordered condensed-phase systems dissipates on the time scale of a few picoseconds, so that its transport is a phenomenon intrinsically limited to ultrafast time scales. In contrast, allosteric signaling in proteins involves large-scale structural changes, which occur on a microsecond or even slower time scale [10]. Therefore, a naive picture of allosteric regulation, assuming that signaling is directly related to the propagation of vibrational energy that is released at the allosteric site after binding of a substrate, is certainly not correct. However, despite the clear separation of time scales, the ultrafast vibrational energy transport might still be a prerequisite for the much slower functional dynamics [11, 12], in the sense that the existence of fast fluctuations pinpoints the soft degrees of freedom in the biomolecule, along which conformational changes preferably occur.

Another vital function of vibrational energy transport is to regulate the temperature of proteins. Especially in photoactive biomolecules, the photon energy absorbed by the chromophore is rapidly converted to heat, causing the temperature of the protein to increase [13]. Since proteins generally function only in a very narrow temperature range, excess energy – once it did its job – must be removed efficiently to avoid overheating and enable the protein to serve as an environment for chemical reactions in cells [14].

To study vibrational energy transport from a theoretical point of view, a commonly used approach is based on the normal mode distribution of disordered media [15, 16], taking additionally into account anharmonic scattering terms, similar to the description of the physics of one-dimensional glasses [1, 17–22]. Another very intuitive method for studying vibrational energy transport properties is to run nonequilibrium MD simulations, depositing excess energy into one vibrational mode and calculating its flow through the system directly as a function of time [2, 23–29]. Alternatively, energy transfer can also be studied by applying linear response theory on static properties derived from equilibrium MD simulations [30]. A common finding of many of these theoretical studies is that the vibrational energy flow in proteins is highly anisotropic [6, 8, 9, 18, 19, 25, 27, 30], i.e. it is directionally dependent and occurs preferably along specific transport pathways. On the experimental side, especially the advance of ultrafast laser technology in the last two decades has contributed to a better understanding of vibrational energy transport phenomena. Energy transport on the microscopic scale has been studied in several different molecular systems, including long-chain hydrocarbon molecules [31], bridged azulene-anthracene compounds [32], small molecules in solution [33], single amino acids [34, 35], phospholipid bilayer liposomes [36], and reverse micelles [37]. Regarding proteins, however, only very few experimental studies exist, most of which focus on the vibrational energy flow in heme proteins [13, 38–41]. In this case, however, it has later been argued that vibrational energy transport into the surrounding solvent does not occur through the protein, but through its propionate side chain connecting it directly to the protein surface [27, 42]. Especially the theoretically predicted anisotropic nature of vibrational energy transport through proteins has not been confirmed in any experiment so far.

Therefore, the aim of this thesis is to develop new methods for studying the energy flow through biomolecules with ultrafast vibrational spectroscopy. For this purpose, an experimental concept is used that has recently been introduced by Hamm and coworkers [43], allowing for the measurement of vibrational energy transport with femtosecond time resolution and Ångström spatial resolution. Briefly, the idea is to locally deposit vibrational excess energy at one defined site of a biomolecule by means of an ultrafast local heater. The subsequent appearance of vibrational energy at any distant site of the molecule is detected by employing suitable vibrational probes as local thermometers. The most important components of such experiments – a stable model structure, local thermometers and a local heater – are discussed in the following.

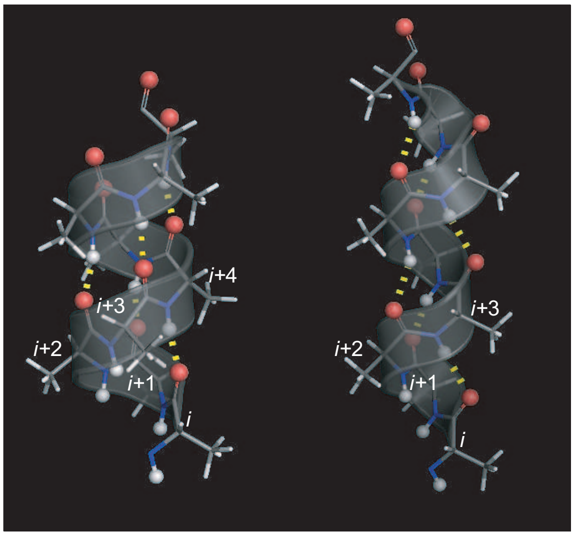

Figure 1.1: 9 Alanine residues folded into an idealized right-handed α-helix (left) and 3_{10}-helix (right). In the α-helix the hydrogen bonds (indicated as dashed yellow lines) are formed between the backbone C=O group of the ith amino acid and the backbone N−H group 4 residues later ($i \leftarrow i{+}4$ hydrogen bonding). Each loop formed by a hydrogen bond comprises 13 atoms and the helix needs 3.6 amino acid residues per full turn; therefore, in the systematic nomenclature this conformation is also described as a 3.6_{13}-helix. The tighter 3_{10}-helix is stabilized by $i \leftarrow i+3$ hydrogen bonding; a H-bonded loop consists of only 10 atoms and the helix has 3 residues per turn.

The ultimate aim of such a study is of course to apply this method to any arbitrary protein, and the results presented in one of the last chapters of this thesis will show first steps in this direction. However, for understanding the basic properties of vibrational energy transport, it is convenient to resort to simpler model structures such as short helical peptides. Helices are the most abundant secondary structure motif in proteins, in which the chain of amino acids adopts a spiral-like geometry stabilized by intramolecular C=O...H−N hydrogen bonds between different amino acids. In the most common helical structure, the α-helix, hydrogen bonding occurs between the backbone C=O group of the ith amino acid and the backbone N−H group four residues later ($i \leftarrow i+4$ hydrogen bonding, see Fig. 1.1, left). For most of the experiments presented in this thesis, the tighter 3_{10}-helix, which is stabilized by $i \leftarrow i+3$ hydrogen bonding, is chosen as a model structure (see Fig. 1.1, right). Although considerably less common than the classical α-helix, also the 3_{10}-conformation is a naturally-occurring motif found in globular proteins [44]. The reason for this choice is simply that the 3_{10}-conformation is very stable even for relatively short sequences of approximately eight amino acids [45], whereas the α-helix needs on the order of 20 amino acids to become stable [46].

To follow the flow of vibrational energy along the helix, one can use vibrational reporter groups in the peptide backbone as local thermometers. The underlying mechanism of such a vibrational thermometer is discussed in detail in Ref. [47]: upon heating, vibrational transitions become broader and shift to lower frequency due to anharmonic coupling to vibrationally excited lower-frequency modes. As long as these anharmonic shifts are small compared to the line width of the reporter mode, the response can be used as a linear measure of the amount of vibrational energy in the vicinity of the probe.

To obtain an ubiquitous and noninvasive vibrational reporter group in the backbone of a biomolecular chain, it is favorable to focus on the structural repeat unit of peptides and proteins, which is the $-C(=O)NH-$ linkage between neighboring amino acids. This so-called peptide bond has nine characteristic infrared (IR) absorption bands − referred to as amide A, B, and I-VII (from high to low frequency) [48,49] − the most prominent of which is the amide I vibration, mainly involving the carbonyl ($C=O$) stretch. The amide I absorption band of a protein comprises the $C=O$ vibrations of all peptide bonds in the molecule, and can as such only provide global information averaged over the entire structure. However, it is possible to identify individual carbonyl bonds by site-selective isotope labeling so that local information can be obtained. Increasing the mass of the carbon, the oxygen or both atoms, downshifts the frequency of the respective $C=O$ vibration, which decouples the labeled group from the remaining main amide I band giving it a pronounced local-mode character [50]. Then, by placing the isotope label at different positions in the peptide (one at a time), one obtains local vibrational reporter groups allowing to measure the local temperature at various distances from the heat source as a function of time.

For a local heater to be useful it must satisfy some general criteria: first of all, since the heater determines the time resolution of the experiment, it should be ultrafast, i.e. the localized release of vibrational excess energy should occur on the $\lesssim$1 ps time scale. Second, to ensure that the excitation is local, the optical absorption of the heater must not overlap with those of biomolecules, a number of whose constituent amino acids absorb UV light at wavelengths below $\approx$300 nm. Third, the conversion of light into thermal energy must be efficient so that the generated heat signals are sufficiently large to be followed over large distances in the biomolecule. In a first study demonstrating the experimental concept described above, Botan *et al.* initiated vibrational energy transport through a short helical peptide by means of an azobenzene chromophore that was covalently attached to one end of the molecular chain [43]. Upon UV excitation, this local heater undergoes an ultrafast *cis-trans* isomerization, releasing a large amount of vibrational excess energy on a 200 fs time scale.

The experiments by Botan *et al.* showed that vibrational energy transport in helical peptides occurs in a diffusive manner, with a thermal diffusivity of 2 $\mathrm{\AA}^2\mathrm{ps}^{-1}$ [43]. In two follow-up papers, Backus *et al.* studied the dependence of the vibrational energy transport properties on the amount of initially deposited energy and the dependence on solvent temperature, showing that direct IR pumping of peptide $C=O$ groups leads to a much higher thermal diffusivity of 8 $\mathrm{\AA}^2\mathrm{ps}^{-1}$ [51], and that energy transport at lower temperatures occurs ballistically but less efficiently [52]. This series of papers [43, 51, 52] laid the ground for a better understanding of vibrational energy transport in biomolecules but also left several unexplained results, which designate the starting point of this thesis. Therefore, the experimental and theoretical studies presented in the following chapters of the text aim to answer the following questions:

- Why is the experimentally measured thermal diffusivity so low?

  The thermal diffusivity of 2 $\mathrm{\AA}^2\mathrm{ps}^{-1}$ observed by Botan *et al.* after UV pumping of the azobenzene chromophore [43] is significantly lower than values known for bulk materials (10-20 2 $\mathrm{\AA}^2\mathrm{ps}^{-1}$) [18, 19]. For instance, the thermal diffusivity is 14 $\mathrm{\AA}^2\mathrm{ps}^{-1}$ for bulk water [53] and varies only little with material; in case of proteins, values of 10-15 $\mathrm{\AA}^2\mathrm{ps}^{-1}$ have been reported [54]. Furthermore, accompanying MD simulations could only qualitatively reproduce the experimental observations, but show a value for the thermal diffusivity that is five times faster and would agree with experimental bulk values. Furthermore, the MD result is consistent with other theoretical works [2, 6, 14, 18, 19, 23–27].

- Does the thermal diffusivity depend on how and how much energy is deposited?

  Backus *et al.* compared the high-energy (UV) excitation result to that after excitation of a single C=O oscillator in the peptide backbone with low-energy (IR) photons [51]. In the latter case, they seemed to observe a significantly faster heat transport efficiency (thermal diffusivity $\gtrsim 8$ Å^{2}ps^{-1}) that is in agreement with bulk values. Accompanying MD simulations, however, did not reproduce any dependence of the thermal diffusivity on the amount of heating.

- Why does heat transport change from diffusive to ballistic at low temperatures, and at the same time becomes less efficient?

  Backus *et al.* showed that one can switch the mechanism of vibrational energy transport after UV pumping from diffusive at high solvent temperatures to ballistic at low solvent temperatures [52]. Counterintuitively though, transport becomes less efficient as it becomes ballistic. This effect, again, could not be reproduced by accompanying MD simulations.

This thesis is organized in the following way: after this introduction, an overview of the relevant theoretical concepts for describing vibrational energy flow in biomolecular chains is given in Chapter 2. The two following Chapters 3 and 4 present simulation studies on vibrational energy transport, performed on a simple toy model mimicking the normal mode distribution found in proteins. In particular, it is demonstrated that the mechanism of vibrational energy transport on length scales of a few chemical bonds and time scales of a few picoseconds is distinctively different from heat diffusion on macroscopic scales, because vibrational energy does not thermalize on the ultrafast time scale of transport. Before studying vibrational energy transport from an experimental point of view, the necessary methods and setups are introduced in Chapter 5. Chapter 6 presents an experiment, in which fully deuterated leucine is used as an alternative local heater to study vibrational energy transport after excitation with pulsed laser radiation. It is demonstrated that vibrational energy transport is linear on the given length and time scales, i.e. the transport properties of a peptide helix do not depend on the amount of transported energy. Another novel heating mechanism is introduced in Chapter 7, showing for the first time the use of plasmonically heated gold nanoparticles as local heaters for energy transport studies. The results of the different energy transport experiments on short helical are shortly summarized in Chapter 8, before moving on to studying energy transport in a larger, three-dimensional molecular structure: Chapter 9 presents a preparatory study on energy transport in the 36-residue villin headpiece protein, using both a specifically-designed water-soluble azobenzene chromophore, and a small plasmonically heated gold nanoparticle as local heating mechanisms. Finally, the results of this work are summarized in Chapter 10. Some mathematical supplements and details of important synthesis steps are given in the Appendix.

Chapter 2

Theory of vibrational energy transport in biomolecular chains

Biomolecules are regular but aperiodic structures. Although their individual molecular repeat units can be rather complicated, a useful analog for understanding their transport properties is to conceptually compare them to a one-dimensional glass, i.e. a linear disordered chain of anharmonically coupled atoms. The aim of this chapter is to provide the theoretical background necessary for describing the vibrational modes of such low-dimensional amorphous media, and vibrational energy redistribution between them. First, the effects of disorder and anharmonicity are discussed in detail, and summarized in a model for describing vibrational energy transport in biomolecular chains. Then, within the framework of this model, the theory developed by Leitner and coworkers [1,6,14,17–19] for calculating macroscopic heat transport coefficients of peptides and proteins is introduced.

2.1 Introduction

According to the law of heat conduction, also known as Fourier's law, the heat current density $\vec{j}$ is proportional to the gradient of the temperature T

$$\vec{j}(\vec{r},t) = -\kappa \nabla T(\vec{r},t)\,, \tag{2.1}$$

where the underlying proportionality constant κ is referred to as the thermal conductivity, and the minus sign indicates that the direction of heat flow counteracts the temperature difference. With the definition of the volumetric heat capacity, which is the product of the mass density ρ and the specific heat capacity c,

$$\frac{\partial q}{\partial T} = \rho c \tag{2.2}$$

the continuity equation for the heat density q can be formulated as

$$\nabla \vec{j} = -\frac{\partial q}{\partial t} = -\rho c \frac{\partial T}{\partial t}\,. \tag{2.3}$$

Then, with Equations (2.1) and (2.3) the general heat diffusion equation can be obtained as follows:

$$\begin{aligned}\frac{\partial T(\vec{r},t)}{\partial t} &= -\frac{1}{\rho c}\nabla\vec{j}(\vec{r},t) \\ &= -\frac{1}{\rho c}\nabla(-\kappa\nabla T(\vec{r},t)) \\ &= \frac{\kappa}{\rho c}\nabla^2 T(\vec{r},t) \\ &= D\Delta T(\vec{r},t)\end{aligned} \tag{2.4}$$

Hence, Fourier's law directly implies that heat transport is diffusive, with a thermal diffusivity, or heat diffusion constant D:

$$D = \frac{\kappa}{\rho c} \tag{2.5}$$

On a microscopic level, the diffusive nature of heat transport can be understood from the motion of the heat carriers, e.g., electrons or lattice vibrations, which suffer random collisions and therefore move diffusively [55]. As a consequence of the randomness of the heat transport process, the mean square displacement $\langle r^2 \rangle$ of the energy increases only linearly with time

$$\left\langle r^2 \right\rangle (t) \propto Dt\,, \tag{2.6}$$

whereas in the case of directed, ballistic transport it would increase with the square of time. This characteristic behavior can be observed for any diffusive process; a detailed derivation of this relation for the one-dimensional case can be found in Appendix B.

The heat diffusion equation (Eq. (2.4)), as immediately becomes clear from its name, implicitly assumes that the transported energy is thermalized, i.e. that the system can be completely described by its local temperature $T(\vec{r},t)$. However, as will be shown in the later parts of this thesis, such macroscopic concepts do not necessarily apply for describing heat transport on the microscopic scale. For example, it is obvious that the very concept of a local temperature breaks down on ultrashort length and time scales, when vibrational energy does not have time to adopt an equilibrium Boltzmann distribution.

2.2 Effects of disorder

It is a common finding that disorder decreases the mean free path of collective excitations, which induces localization effects that hamper transport processes [56]. The same is true for proteins, in which the vast majority of the vibrational normal modes are spatially localized and cannot carry vibrational energy, while only a relatively small subset of the lowest frequency normal modes are extended over the entire molecular structure [17–19]. In this respect, the vibrational modes of proteins very much resemble those of a one-dimensional glass, in which almost all modes are localized − in contrast to a three-dimensional glass, where the situation is basically inverted [18]. Therefore, an important concept for describing the vibrational normal modes of disordered biomolecules is to compare them with those of an aperiodic chain of atoms [18]. In the case of a periodic harmonic chain, the vibrational normal modes are phonons that can transport energy without resistance from one end of the chain to the other, i.e. vibrational energy can propagate ballistically and the thermal conductivity κ has an infinite value [57]. However, in the presence of disorder − which can have its origin in random masses and/or random force constants − vibrational energy transport becomes diffusive and can be described by finite thermal transport coefficients κ or D.

For calculating the energy transport properties of disordered chains, it is important to know how many of the N vibrational normal modes are actually delocalized, and thus able to contribute to energy transport. This question was first answered by Matsuda and Ishii [15], who could analytically show that all vibrational modes above a certain demarcation frequency ω_d are spatially localized, and that only a few remaining low-frequency modes, the number of which scales as the order of $\sqrt{N}$, have localization lengths longer than the chain itself. The proof of this finding can be found in great detail in Refs. [15, 16], the most important steps of which are summarized in the following:

Consider a finite, one-dimensional chain consisting of N sites (with consequently N normal modes), the nearest neighbors of which are coupled to each other by harmonic springs with equal force constants k. Disorder is introduced by using a random distribution of the masses m_n, but the same effect could also be achieved with random force constants. If u_n is the displacement of the nth atom from its equilibrium position, the system is described by the following equation of motion:

$$m_n \frac{d^2 u_n}{dt^2} = k\left(u_{n+1} - 2u_n + u_{n-1}\right) \ \text{, with } (n = 1, 2, ..., N) \tag{2.7}$$

Assuming that all masses oscillate at the same mode frequency ω (i.e., $u_n \propto \exp(-i\omega t)$) the stationary equation of motion is obtained:

$$-m_n \omega^2 u_n = k\left(u_{n+1} - 2u_n + u_{n-1}\right) \tag{2.8}$$

A crucial step is to reformulate Eq. (2.8) by means of a so-called transfer matrix T_n, which connects the displacements at sites $n+1$, n, and $n-1$:

$$\begin{pmatrix} u_{n+1} \\ u_n \end{pmatrix} = T_n \begin{pmatrix} u_n \\ u_{n-1} \end{pmatrix} \ \text{, with } T_n = \begin{pmatrix} 2 - m_n\omega^2/k & -1 \\ 1 & 0 \end{pmatrix} \tag{2.9}$$

Hence, if the initial values of u_0 and u_1 at one end of the chain are known, the displacement at any other position n can be obtained by repeated multiplication with the transfer matrix:

$$\begin{pmatrix} u_{n+1} \\ u_n \end{pmatrix} = T_N T_{N-1} ... T_1 \begin{pmatrix} u_1 \\ u_0 \end{pmatrix} \quad \text{or} \quad \vec{u}_n = T_N T_{N-1} ... T_1 \vec{u}_0 \tag{2.10}$$

The asymptotic properties of such a product of random matrices are treated in Furstenberg's theorem [58]: briefly, it can be shown that if at least two of the nonsingular, identically distributed (2x2)-matrices T_n do not have common eigenvectors, then there always exists a constant number λ such that, for each $\vec{u}_0 \neq 0$

$$\begin{aligned} \lambda &= \lim_{N\to\infty} \frac{1}{N} \log|\vec{u}_n| \\ &= \lim_{N\to\infty} \frac{1}{N} \log|T_N T_{N-1} ... T_1 \vec{u}_0| > 0\,. \end{aligned} \tag{2.11}$$

This number λ is referred to as the Lyapunov exponent[a] and characterizes the average rate of exponential growth of the norm of the state vectors $\vec{u}_n$ for large N [59,60]. A result

---

[a] In the original papers by Matsuda and Ishii [15, 16], the term Lyapunov exponent does not explicitly appear; instead the authors calculate the squared value of the norm which gives them a number 2λ.

of the positivity of λ is the localization of vibrational normal modes: the displacement u_n grows exponentially from each end of the large but finite chain and matches at the maximum [60]. That means, if a vibrational normal mode is localized at some position n_l of the chain, its amplitude decays exponentially to both sides according to:

$$|u_n| \propto e^{-\lambda|n-n_l|} \tag{2.12}$$

Hence, the physical meaning of λ is the inverse of the localization length ξ of a vibrational normal mode.

It can be shown that in the limit of $\omega \to 0$, the localization length ξ as a function of the mode frequency can be calculated as follows (Eq. (2.7) in Ref. [15]):

$$\xi(\omega) = \frac{1}{\lambda} = \frac{8k\langle m_n\rangle}{\omega^2 \left\langle (m_n - \langle m_n\rangle)^2\right\rangle} \tag{2.13}$$

Hence, the spatial confinement of vibrational normal modes increases with frequency as ω^{-2}. Note that in the absence of disorder, the mass variance $\langle (m_n - \langle m_n\rangle)^2\rangle$ in the denominator of Eq. (2.13) disappears, so that the localization length approaches infinity, which is the expected result for the vibrational modes of a periodic harmonic chain, i.e. phonons.

A vibrational normal mode can be considered as localized if its localization length ξ is smaller than half the length of the chain $N/2$, which, according to Eq. (2.13), is the case for all modes above a certain demarcation frequency ω_d:

$$\omega > 4\sqrt{\frac{k\langle m_n\rangle}{N\left\langle (m_n - \langle m_n\rangle)^2\right\rangle}} \equiv \omega_d \tag{2.14}$$

In the low-frequency regime, where Eq. (2.13) is valid, the frequency of a normal mode can be approximated by the dispersion relation of a phonon

$$\omega_n \approx \sqrt{\frac{k}{\langle m_n\rangle}}\frac{n}{N}\pi\,, \tag{2.15}$$

where n labels the normal modes with increasing frequency. Then, the corresponding demarcation mode number n_d, up to which all vibrational normal modes are delocalized over the entire structure, can be written as:

$$n_d = \frac{4}{\pi}\frac{\langle m_n\rangle}{\sqrt{\left\langle (m_n - \langle m_n\rangle)^2\right\rangle}}\sqrt{N} \tag{2.16}$$

From this equation one can conclude that from the N vibrational normal modes of the disordered chain, all but the lowest-frequency modes, the number of which scales as the order of $\sqrt{N}$, are localized.

In a hypothetical one-dimensional silicon glass, the demarcation frequency ω_d, which separates the extended from the localized vibrational excitations, lies somewhere around 15 meV [20], corresponding to approximately 120 cm^{-1}. Similarly, in the concrete example of a real protein, in which the molecular repeat units are amino acids with many internal degrees of freedom, mode localization starts around 150-200 cm^{-1} [1,18,19] and increases with frequency as predicted by Eq. (2.13). Figure 2.1 shows the localization length ξ

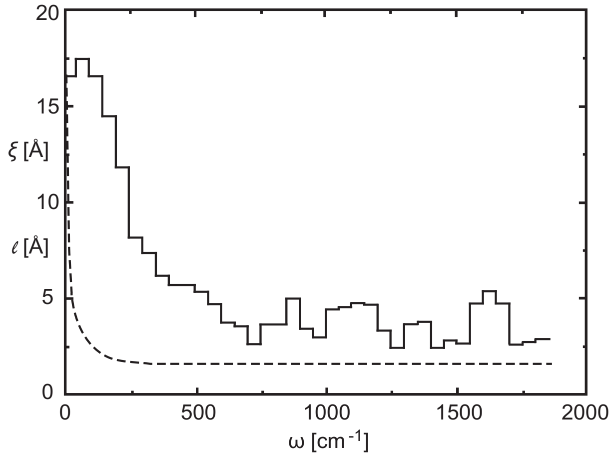

Figure 2.1: Localization length ξ (solid) and mean free path ℓ (dashed) of the vibrational normal modes of myoglobin calculated by Leitner and coworkers [18]. The vibrational normal modes below 150 cm^{-1} have localization lengths around 16-17 Å and are consequently extended over the entire protein molecule. Above 150 cm^{-1} the localization length declines with increasing frequency to values between 2.5 and 5 Å, which corresponds to some chemical bonds. Figure reprinted with permission from Ref. [18]. Copyright © (2003), American Chemical Society.

and the mean free path ℓ of the vibrational normal modes of myoglobin as a function of their oscillation frequency ω, as calculated by Leitner and coworkers [18]. Basically all vibrational normal modes above a frequency of $\approx$150 cm^{-1} are spatially confined to small regions of the protein, spanning only some chemical bonds. Only the remaining lowest-frequency modes have localization lengths of 16-17 Å, which is comparable to the size of the protein, and thus can be considered as delocalized over the entire molecular structure.

An important consequence of strong localization, which has been emphasized by Fabian [20] and Leitner [17,18], is that localized vibrational normal modes show a propensity to repel each other, i.e they are either close in space *or* close in frequency. A simple explanation of this effect is given in Ref. [61]: consider just two oscillators whose vibrational frequencies differ by $\Delta\omega$. As long as these oscillators are far apart in space, their coupling will be negligible and their energies will remain localized at each of the sites, even if their oscillation frequencies are resonant, i.e. $\Delta\omega = 0$. However, if the oscillators are brought close in space, the coupling between them will increase and possibly exceed $\Delta\omega$, so that the vibrational eigenstates become delocalized [61]. Hence, spatially overlapping vibrational normal modes only remain localized as long as $\Delta\omega$ is larger than the coupling between them, which is on the order of several 100 cm^{-1}. As a result, frequencies of localized modes that overlap in space must be rather different [18], which will have consequences for their anharmonic decay behavior that is discussed in the following section.

2.3 Effects of anharmonicity

In the previous section it was demonstrated, how introducing disorder into a harmonic periodic chain of atoms leads to localization of vibrational normal modes. In this section another mechanism, relevant for the redistribution and transport of vibrational energy is taken into account, which is anharmonicity.

It is obvious that any perfectly harmonic model of coupled oscillators is unphysical, because an initial excitation will not evolve toward an equilibrium state [62]. This is because harmonic vibrations can be described in terms of normal modes, which form an orthogonal basis of eigenstates. As such, vibrational normal modes are decoupled, i.e. noninteracting, and energy deposited into one mode will not appear in any other mode. In such a scenario, only the few delocalized low-frequency modes of a disordered chain can contribute to vibrational energy transport [17], while energy contained in a higher-frequency mode will stay confined at the position n_l, where the respective mode is localized. Transferring this situation to a protein would imply that a significant fraction of the vibrational energy available at physiological temperatures – which corresponds to approximately 215 cm^{-1} – would be trapped in localized higher-frequency modes [18]. Based on similar considerations, Debye suggested already one century ago that nonlinearity must be included in the description of lattices to be able to explain the observed equilibration and transport properties [62].

In 1953, following this line of thought, Fermi, Pasta and Ulam (FPU) performed their famous numerical simulations on the problem of vibrational energy equilibration in a periodic (i.e., equal masses and force constants) weakly anharmonic chain of oscillators [63], which nowadays is considered as one of the first computer experiments ever. In their simulations FPU observed that vibrational energy, which is initially deposited into one vibrational mode, does not equilibrate among all degrees of freedom of the system, but instead is only exchanged among a few modes before returning to its initial value, showing almost periodic behavior [63]. Hence, despite the presence of anharmonicity, the FPU system does not show any tendency toward a thermalization of vibrational energy! This infinite relaxation time directly implies that the thermal conductivity κ is also infinite [62], thus making the weakly anharmonic periodic chain a perfect energy conductor, like the harmonic periodic chain. This surprising behavior could later be explained by Zabusky and Kruskal [64], who described the FPU system with the Korteweg-de Vries equation, which shows solitary-wave solutions. Since these solitons behave like harmonic particles they do not irreversibly scatter with each other, i.e. they do not exchange energy, so that the FPU system cannot equilibrate. More recently, it was demonstrated that if the nonlinearity of the system is increased, e.g. by increasing the energy density, the FPU system undergoes a transition into a chaotic regime, where energy quickly relaxes to equipartition [65].

The pioneering studies considering disorder and anharmonicity simultaneously were the numerical simulations by Payton, Rich and Visscher [57] as well as Jackson, Pasta and Waters [66], both starting from the anharmonic FPU chain but adding disorder in the form of a random binary mixture of masses or random nonlinear coupling constants [67]. In a naive picture, one would expect that anharmonicity and disorder constitute two independent, and therefore additive, scattering mechanisms, both of which decrease the thermal conductivity [57]. On the contrary, the simulations revealed that, except in the case of weak disorder, where adding anharmonicity indeed leads to a further decrease of κ, most other systems are affected in the opposite way: in the presence of strong disorder, when most of the normal modes are localized, the addition of anharmonic scattering enhances the thermal conductivity as compared to the respective harmonic system. From this result the authors of Ref. [57] concluded that anharmonic coupling allows localized modes, which otherwise are frozen out of the energy transport process, to decay into lower-frequency propagating modes.

With this interpretation, Payton *et al.* anticipated a picture, later formulated in the context of amorphous solids by Alexander, Orbach and coworkers [21,22], and elaborated in more detail by Leitner and coworkers [14,17,18] to describe the energy transport properties of peptides and proteins. The main idea is to separate vibrational modes into delocalized phonon-like low-frequency modes, and localized high-frequency modes; the former carrying heat, the latter only taking part in the transport process after anharmonic decay into spatially extended modes. Then, also the transport properties can be divided into two contributions, one which is governed by propagation along the phonon-like modes, and the other by anharmonicity-induced, phonon-assisted transport between localized modes (compare Sec. 2.4, below).

To elucidate the role of anharmonic scattering in vibrational energy redistribution in disordered systems, Leitner *et al.* calculated the anharmonic decay rates $W(\omega)$ (i.e., the inverse lifetimes) of the vibrational modes in a one-dimensional glass [17], α-helices [1] and entire proteins [18,19]. For this purpose they considered only cubic anharmonic terms, i.e. scattering processes with three vibrational modes involved, and neglected all higher-order contributions. At low temperatures, vibrational energy transfer is dominated by processes that involve the decay of a vibrational excitation with frequency ω_α, into two others with lower frequencies ω_β and ω_γ, such that $\omega_\alpha = \omega_\beta + \omega_\gamma$. Then, the corresponding energy transfer rate is given by Fermi's Golden Rule [1]:

$$W(\omega_\alpha) = \frac{\hbar\pi}{8\omega_\alpha} \sum_{\beta,\gamma} \frac{|\Phi_{\alpha\beta\gamma}|^2}{\omega_\beta\omega_\gamma} \left(1 + n_\beta(T) + n_\gamma(T)\right) \delta\left(\omega_\alpha - \omega_\beta - \omega_\gamma\right), \tag{2.17}$$

where the temperature-dependent occupation numbers $n_i(T)$ of modes with frequency ω_i are given by

$$n_i(T) = (e^{\hbar\omega_i/k_BT} - 1)^{-1} \tag{2.18}$$

and the corresponding matrix elements $\Phi_{\alpha\beta\gamma}$ are obtained as the coefficients of the cubic terms, when expanding the coupling potential of the chain V in normal coordinates Q:

$$\Phi_{\alpha\beta\gamma} = \frac{\partial^3 V}{\partial Q_\alpha \partial Q_\beta \partial Q_\gamma} \tag{2.19}$$

Calculation of the vibrational energy transfer rates $W(\omega)$ at different temperatures, leads to the remarkable result that above a frequency of about 500 cm^{-1} the decay rates hardly show any temperature dependence [1, 18, 19]. In Eq. (2.17), the temperature dependence enters through the occupation numbers of the final states $n_\beta(T)$ and $n_\gamma(T)$. Hence, a strong temperature dependence of the anharmonic decay rate $W(\omega)$ implies that energy flows into vibrational states, that are sufficiently low in frequency to be thermally populated, i.e. $n_\beta(T), n_\gamma(T) \neq 0$. Therefore, from the observed temperature invariance, Leitner *et al.* conclude that there can be only little *direct* energy transfer from localized modes with $\omega >$500 cm^{-1} into delocalized low-frequency modes [1, 18, 19].

This finding can be explained as follows: for energy redistribution to occur, energy between the involved modes must be conserved, as expressed by the resonance condition in Eq. (2.17). This means, if a localized vibrational excitation with frequency ω_α decays into two other modes – one of which is delocalized with accordingly low frequency $\omega_\beta <$150 cm^{-1} – then the remaining energy must end up in another localized mode, whose frequency ω_γ is only slightly lower than ω_α. However, it has been discussed above that

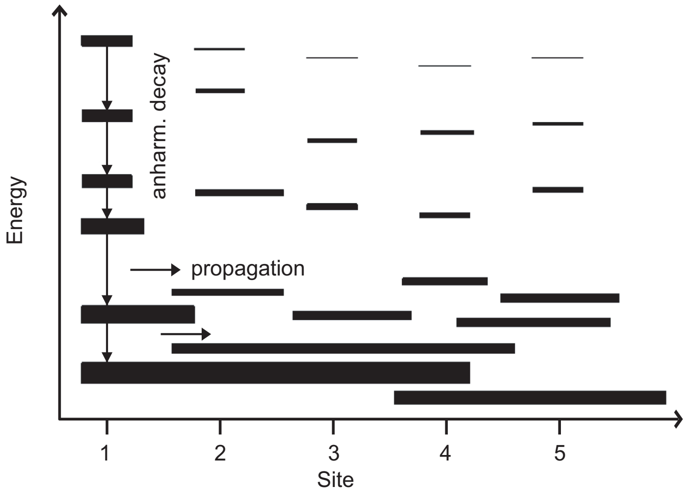

Figure 2.2: Schematic representation of energy transport between the vibrational modes of an anharmonic aperiodic chain of five coupled oscillators, in which site #1 carries an excess of vibrational energy as indicated by the thickness of the lines. Disorder leads to localization of vibrational modes, the effect of which increases with frequency; only the lowest-frequency modes are delocalized over various sites and can transport energy along the chain. Anharmonicity couples the localized modes to the propagating modes, so that energy can relax in a cascade-like process and equilibrate among all degrees of freedom. Figure adapted from Ref. [51].

localized vibrational modes tend to spatially repel each other [17, 18, 20]. Hence, the spatial overlap of two localized modes with similar frequencies $\omega_\alpha \approx \omega_\gamma$ must be small, and so is the matrix element $\Phi_{\alpha\beta\gamma}$ of the underlying anharmonic scattering process among the three modes. Consequently, the rate of energy transfer from a localized mode into another localized mode with similar frequency, and the remainder into a delocalized mode with low frequency, must be small [18].

This in turn means that the contribution of anharmonicity to thermal transport is almost entirely given by vibrational energy transfer among spatially overlapping localized modes [17], which accordingly must have significantly different frequencies. It has been shown that the modes that couple most strongly to a localized mode with frequency ω_α have frequencies in the range $\omega_\alpha/3$ to $2\omega_\alpha/3$ [17]. As an optimal case, one can imagine Fermi-resonant transitions, in which a localized vibrational excitation with frequency ω_α decays into two quanta of a spatially overlapping mode with frequency $\omega_\beta = \omega_\alpha/2$. Hence, vibrational energy contained in a localized mode does not relax into a propagating mode in just one single anharmonic decay, but instead cascades down the vibrational ladder via several localized modes with intermediate vibrational frequency.

The effects of anharmonicity and disorder being discussed in this and the previous section, motivate a model for the description of vibrational energy transport in biomolecular chains, which is schematically illustrated in Figure 2.2. It depicts the vibrational mode distribution of an anharmonic aperiodic chain of coupled oscillators, in which one site carries an excess of energy. Since disorder decreases the localization length ξ of vibrational excitations – the effect of which increases with frequency according to Eq. (2.13) – the majority of vibrational modes is spatially confined to individual sites of the chain.

Only the remaining lowest-frequency modes are delocalized over the entire system and can contribute to energy propagation along the chain. The addition of anharmonicity allows localized high-frequency modes to decay into lower-frequency propagating modes. The underlying equilibration process predominantly takes place between spatially overlapping modes of dissimilar frequency. Hence, anharmonicity gives rise to vibrational energy redistribution, occurring in a cascade-like process within individual sites.

2.4 Calculation of thermal transport properties

Within the framework of the model derived in the two previous sections to describe vibrational energy transport in the presence of disorder and anharmonicity, it is now possible to estimate the transport properties of biomolecular chains. For systems large enough, e.g. proteins, this problem can be addressed in macroscopic terms, such that thermal transport coefficients can be calculated [14]. These coefficients, however, must be understood as effective values, because the flow of vibrational energy transport in proteins is expected to be anisotropic. The following discussion is based on the theory developed by Leitner and coworkers [6, 14, 17–19].

The thermal conductivity κ, which describes the ability of a material to conduct heat (compare Eq. (2.1)), can be calculated as

$$\kappa = \int d\omega n(\omega) c(\omega) D^v(\omega) \,, \tag{2.20}$$

where $n(\omega)$ is the density of states, $c(\omega)$ the contribution of a vibrational mode to the total heat capacity (see Eq. (2.22) below), and $D^v(\omega)$ is the frequency-dependent energy diffusion coefficient [18, 21].

The thermal diffusivity D is obtained as the ratio of the thermal conductivity and the heat capacity per unit volume (compare Eq. 2.5), i.e. it describes how rapidly a material can adapt to a temperature change:

$$D = \frac{\kappa}{\int d\omega n(\omega) c(\omega)} = \frac{\int d\omega n(\omega) c(\omega) D^v(\omega)}{\int d\omega n(\omega) c(\omega)} \tag{2.21}$$

The contribution of a vibrational mode with frequency ω to the total heat capacity per unit volume is given by:

$$c(\omega) = \frac{\hbar^2 \omega^2}{V k_B T^2} \frac{e^{\hbar\omega/k_B T}}{\left[e^{\hbar\omega/k_B T} - 1\right]^2} \tag{2.22}$$

This function depends on the occupation of the particular mode, and therefore increases strongly with temperature until it reaches its classical limit of $\hbar^2\omega^2/Vk_BT^2$.

In the harmonic limit, only the extended vibrations with frequencies $\omega < \omega_d$ can carry heat. Because vibrational energy transport in these modes is phonon-like, energy will propagate with the speed of sound c_s over a distance given by the mean free path ℓ. Hence, the diffusion coefficient can be calculated by [18]

$$D^v_{harm}(\omega) = \frac{1}{3} c_s(\omega) \ell(\omega) \,. \tag{2.23}$$

Taking again myoglobin as an example, one finds a value $c_s \approx$20 Å ps^{-1} [18], and ℓ varies as a function of ω as displayed in Figure 2.1, i.e. between lengths spanning the entire

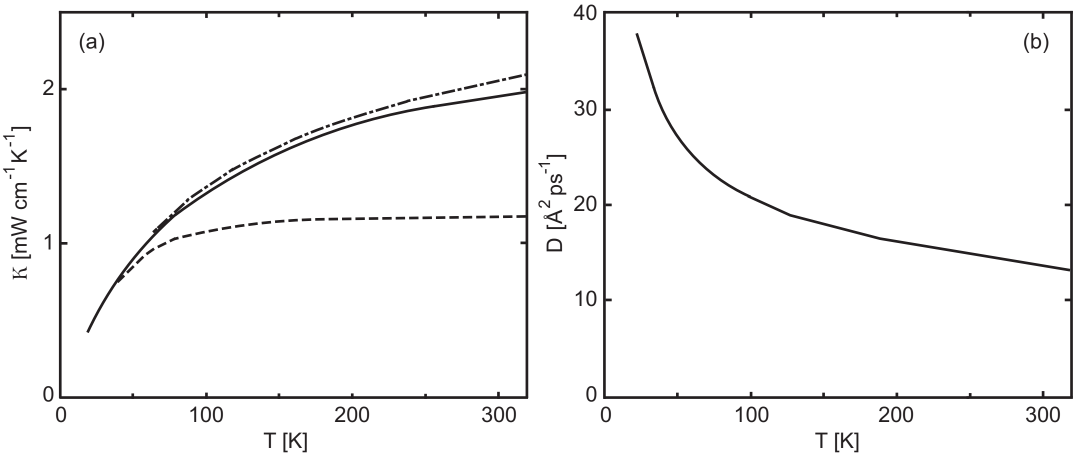

Figure 2.3: (a) Thermal conductivity κ and (b) thermal diffusivity D of myoglobin, as calculated by Leitner and coworkers [18], plotted as solid lines in the temperature range from 20 K to 320 K. For comparison, the dashed curve in (a) gives the thermal conductivity if no anharmonic coupling is included in the calculation, and the dot-dashed curve the same if all normal modes were delocalized over the protein and could contribute to heat transport. Figure reprinted with permission from Ref. [18]. Copyright © (2003), American Chemical Society.

protein and a chemical bond. Then, the thermal conductivity in the harmonic limit can be obtained by using the diffusion coefficient D^v_{harm} as defined in Eq. (2.23) and integrating Eq. (2.20) up to the demarcation frequency $\omega_d \approx$150 cm^{-1}:

$$\kappa_{harm}(T) = \int_0^{\omega_d} d\omega n(\omega) c(\omega) D^v_{harm}(\omega) \tag{2.24}$$

The result obtained by Leitner and coworkers is displayed as a dashed line in Figure 2.3a, showing that κ_{harm} increases with temperature until it saturates to a value of $\approx$1.2 mW cm^{-1} K^{-1}. The initial increase of the thermal conductivity is due to the fact that with increasing temperature more modes are thermally populated and can contribute to transport − the effect of which enters through the heat capacity $c(\omega)$ (Eq. (2.22)). However, if the temperature increases even further, the additionally populated modes lie above the cutoff frequency ω_d and are not regarded in the harmonic limit, which leads to the saturation of κ_{harm}. In order to estimate to what extent localization effects lower the thermal conductivity of a protein, it is interesting to calculate κ_{harm} for the hypothetical situation, in which all vibrational modes of myoglobin would be delocalized and could carry heat. The result for this case, which is obtained by integrating Eq. (2.24) over the entire spectrum of vibrational normal modes $0 \leq \omega \leq \omega_{max}$, is displayed as a dot-dashed line in Figure 2.3a. In contrast to the previous case, κ_{harm} grows over the entire temperature range and reaches a value of 2.1 mW cm^{-1} K^{-1} at $T = 320$ K. Comparing both results, it can be concluded that − at physiological temperatures and in the harmonic limit − localization decreases the thermal conductivity by a factor of 2, because high-frequency modes are frozen out of the energy transport process.

As a next step, the effects of anharmonicity are included in the calculation of the thermal transport properties. Anharmonic coupling allows the localized modes to exchange energy with the rest of the system, the contribution of which, $\kappa_{anh}(T)$, increases the thermal conductivity. Then, the value $\kappa(T) = \kappa_{harm}(T) + \kappa_{anh}(T)$ will lie somewhere between the two extreme cases of the harmonic limit discussed above. The anharmonic contribution to the thermal conductivity can be estimated by using a hopping model as first suggested by Orbach and coworkers [21]. Assuming that energy transport between localized modes is phonon-assisted, energy decays at rate $W(\omega)$ from a localized mode into a lower-frequency mode, where it can propagate over a certain distance until another anharmonic transition occurs at rate $W(\omega)$. If $W(\omega)$ is sufficiently slow, energy has time to spread over the entire localization length of this mode before it is redistributed, so that the mean free path of this process is given by $\ell = \xi$ and the speed by ξW. Then, the diffusion coefficient describing the anharmonic contribution can be written as:

$$D^v_{anh}(\omega) = \frac{1}{3}\xi^2(\omega)W(\omega) \tag{2.25}$$

If, however, the anharmonic decay rate $W(\omega)$ is fast enough, a vibrational excitation will not have time to diffuse over a distance as far as ξ, i.e., energy will be redistributed before it can feel the limitations of mode localization. In this case, intrasite vibrational energy redistribution is not rate-limiting so that the effects of localization do not influence energy transport and the diffusion coefficient is again given by $D^v_{harm}(\omega)$, even for spatially localized modes above the demarcation frequency ω_d. To decide, which diffusion coefficient to use for calculating the thermal diffusivity of modes with $\omega > \omega_d$, Leitner and coworkers estimate the time t^* it takes for a vibrational excitation to diffuse over the entire distance ξ [18]:

$$t^*(\omega) = \frac{1}{3}\frac{\xi^2(\omega)}{D^v_{harm}(\omega)} \tag{2.26}$$

Then, the anharmonic contribution to the thermal conductivity can be calculated as:

$$\kappa_{anh}(T) = \int_{\omega_d}^{\omega_{max}} d\omega n(\omega)c(\omega)D^v(\omega) \text{ with } D^v(\omega) = \begin{cases} D^v_{harm}(\omega) & \text{if } W^{-1}(\omega) \leq t^*(\omega) \\ D^v_{anh}(\omega) & \text{if } W^{-1}(\omega) > t^*(\omega) \end{cases} \tag{2.27}$$

For frequencies ω >500 cm^{-1}, the vibrational modes are highly localized so that energy diffusion is usually dominated by anharmonic decay, and best described by the diffusion coefficient $D^v_{anh}(\omega)$ [18]. For modes between 150 cm^{-1} and 500 cm^{-1} however, the localization lengths ξ become longer and anharmonic decay more efficient, so that anharmonicity redistributes energy faster than a vibrational excitation can travel. Hence, in the intermediate regime just above the localization threshold, vibrational energy transport is still better described by the harmonic diffusion coefficient $D^v_{harm}(\omega)$ [18].

The result for the thermal conductivity $\kappa(T)$ that has been obtained by Leitner and coworkers [18] by using Eq. (2.24) for the delocalized modes below the demarcation frequency, and Eq. (2.27) for all modes above, is displayed as a solid line in Figure 2.3a. The value of the thermal conductivity increases with temperature, to reach a value of around 2 mW cm^{-1} K^{-1} at physiological temperatures, which is about twice the value computed in the harmonic limit and almost as much as if all modes would be delocalized. Hence, anharmonicity enhances energy flow in a protein to an extent that it almost compensates for localization effects.

With the value of $\kappa(T)$ available, it is possible to also calculate the thermal diffusivity D of myoglobin according to Eq. (2.21). The result is displayed in Figure 2.3b, showing that the thermal diffusivity decreases with temperature (which is because the heat capacity increases with temperature more strongly than κ does), and reaches a value of ≈12 Å^2 ps^{-1} at $T = 320\ K$. In the absence of anharmonicity, accordingly, also this transport property would be diminished by an approximate factor of 2 at physiological temperatures [19].

Chapter 3

Vibrational energy transport in the presence of IVR
Part I: Toy model MD simulations

In this chapter, classical and quantum-mechanical molecular dynamics simulations on vibrational energy transport in biomolecular chains are presented. The mechanism of vibrational energy flow is studied in a regime where a diffusion equation is likely to break down, i.e., on length scales of a few chemical bonds and time scales of a few picoseconds. Along the lines of the previous chapter, a toy model is introduced that on the one hand mimics the vibrational normal mode distribution of peptides and proteins, and on the other hand is small enough to numerically time-propagate the system fully quantum mechanically. Comparing classical and quantum-mechanical results the question is addressed how far classical MD simulations, which are the only choice for modeling real biomolecular systems, can be pushed toward an effective and quantitative description of quantum effects in energy transport properties.

3.1 Introduction

The experimental studies presented in the later chapters of this thesis are based on the idea of using pulsed laser radiation to initially prepare a nonequilibrium distribution of vibrational energy in biomolecules, and to follow the subsequent redistribution of energy within the molecule as well as the equilibration with the surroundings with time-resolved vibrational spectroscopy. The purpose of this chapter is to simulate vibrational energy transport in a protein-like system, in order to obtain a better understanding of the involved relaxation processes, which leads to a guideline for the interpretation of experimental observations but also for the development of novel experimental concepts.

A very intuitive approach to study vibrational energy transport properties in biomolecules is to run nonequilibrium MD simulations, depositing excess energy into one vibrational mode and calculate its flow through the system directly as a function of time. The pioneering work in this field was done in 1986 by Henry *et al.* [23], who simulated the vibrational cooling of a laser-excited heme into its surrounding protein. However, because condensed-phase quantum-mechanical calculations are computationally extremely demanding, still today, for any realistically-sized solution phase molecular system one has to resort to classical mechanics MD simulations [2, 23, 24, 26–29].

Of course, classical simulations, as they are based on Newtonian mechanics, can only produce classical results and not account for any quantum effects [68]. While the classical approximation works very well when studying conformational processes of molecular systems, this is not necessarily the case for thermal properties, even in the completely harmonic case. Most evidently, the classical heat capacity of all but the lowest frequency normal modes of molecular systems deviates significantly from its quantum counterpart. It is therefore of great interest to assess the validity of classical mechanics for the investigation of vibrational energy transport properties [68–70]. A popular approach in this context, is to perform classical MD simulations and to multiply the obtained results by so-called quantum correction factors giving the real quantum result [69–71].

As already indicated in Chapter 1, the agreement between the experimental findings obtained by Botan *et al.* [43] and Backus *et al.* [51, 52] and the accompanying classical MD simulations is unsatisfactory. First of all, the simulations overestimate the experimentally measured thermal diffusivity by a factor of five. This is an uncommon finding, because it is known that classical simulations rather underestimate the real vibrational relaxation rates [69]. Application of quantum correction factors to the classical results would yield even higher transport rates, and consequently increase the discrepancy between simulation and experiment. The authors of Ref. [51], therefore, speculated that vibrational energy trapping might be a reason for the experimentally observed low thermal diffusivity, which, however could not be reproduced by the accompanying simulations.

Furthermore, from the classical MD simulations, no conclusive information about the excitation energy dependence of vibrational energy transport can be deduced. Backus *et al.* speculated in Ref. [51] that the rate-limiting step in energy transport is intramolecular vibrational redistribution (IVR) within the various peptide units of the helix, and not the actual transport from site to site. This is related to the very general observation that only a relatively small subset of the lowest frequency normal modes of a protein, the number of which scales as the order of $\sqrt{N}$ (compare Sec. 2.2), tends to delocalize over large distances similar to the physics of glasses [1, 17–20]. The higher-frequency modes, in contrast, are largely localized at individual sites. Hence, when a high-frequency mode is excited, it first needs to relax to a lower-frequency mode before it can be transported along the chain. Since classical and quantum mechanics distribute thermalized vibrational energy very differently among the various modes, the amount of heating could have distinct effects on the subsequent energy relaxation process. While classical MD simulations are known to be largely insensitive on the amount of deposited energy [51] the behavior of quantum-mechanical MD simulations is uncertain and has not been studied so far.

Another effect that could not be reproduced by MD simulations is the transition of vibrational energy transport from diffusive at high solvent temperatures to ballistic − and counterintuitively, less efficient − at low solvent temperatures [52]. To explain this behavior, another speculation raised in Ref. [52] was that the solvent temperature modulates the flexibility of the helix, and thereby intrasite IVR. At low solvent temperatures, intrasite IVR is slow, and only the small fraction of energy that is initially deposited in the low-frequency modes can be transported. This transport is ballistic-like, that means phonon-like in manner, because these low-frequency modes delocalize over length scales that equal the size of the helix. As the solvent temperature increases, IVR becomes significantly more efficient and refeeds vibrational energy from localized high-frequency modes into the low-frequency transporting modes. Due to the large number of states that are

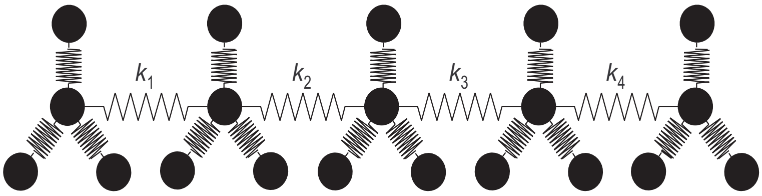

Figure 3.1: Scheme of the 1D chain with n=5 sites and m=4 modes per site. The intersite couplings k_i are indicated. Note that the Hamiltonian Eq. (3.1) is, in fact, one-dimensional (i.e., one normal mode per mass point), different from what the figure might suggest.

involved, IVR has probabilistic character, and energy transport now is diffusive-like, in the sense that it can be fitted by a master equation.

To put some of these speculations on more solid grounds, the aim of this chapter is to devise a toy model that is small enough to numerically propagate the system fully quantum mechanically. The model is designed to mimic the normal mode distribution found in proteins [1, 17–20, 72]: for every site, one low-frequency mode is introduced that couples to neighboring sites through a harmonic spring and therefore is capable to transport energy along the chain. This mode is classical with $\hbar\omega < k_B T$. In addition, a couple of higher-frequency modes is added to each site that are quantum-like ($\hbar\omega > k_B T$) and that communicate with the transporting mode through Fermi resonances (compare Sec. 2.3). First, the system is equilibrated at a certain temperature. Then, all modes of one site at the end of the chain (site #1) are heated to an elevated temperature and the relaxation along the chain is investigated in nonequilibrium MD simulations. To address the question whether the classical nature of MD simulations can explain part of the discrepancy between experiment and simulations, the system is time-propagated both classically and quantum mechanically, using exactly the same potential energy function.

3.2 Model

3.2.1 The Hamiltonian

As a model system, a one-dimensional (1D) chain with n=5 sites and m=4 modes on each site is defined (Fig. 3.1). The set of lowest frequency modes on each site, described in unitless massweighted coordinates $q_{i,1}$, mimics transporting modes modeled as harmonic springs between neighboring sites. The higher-frequency normal modes q_{ij} with $j \geq 2$, in contrast, are normal modes localized on individual sites. Throughout this chapter, the first index, i, labels the site and the second index, j, the corresponding mode on site i. The harmonic part of the Hamiltonian reads

$$H^{(2)} \;=\; T + \frac{1}{2}\sum_{i,j}\omega_{ij}q_{ij}^2 + \frac{1}{2}\sum_{i=1}^{n-1}k_i\left(q_{i,1} - q_{i+1,1}\right)^2 , \tag{3.1}$$

where T is the corresponding kinetic energy, ω_{ij} the on-site frequency of the mode, and k_i the coupling constant between the sites. All energies are defined in units of the base temperature, $k_B T_0 = 200$ cm^{-1} at room temperature and time is given in units of $\hbar/k_B T_0 \approx 25$ fs at room temperature.

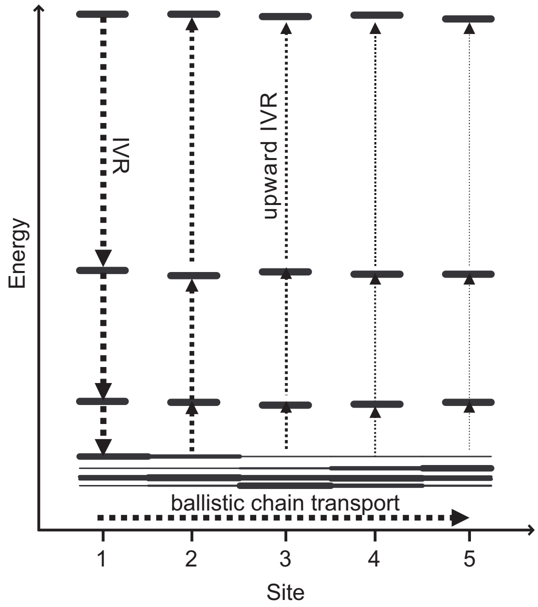

Figure 3.2: Normal mode distribution for a typical realization of the Hamiltonian. The thickness of the lines represents the amplitudes of the various normal modes at individual sites. The arrows symbolize intrasite IVR and chain transport processes, see discussion. Two of the low-frequency modes are so close that they are not resolved in this representation.

For clarity, the Hamiltonian is sorted by its diagonal and off-diagonal elements:

$$H^{(2)} = \frac{1}{2}\sum_{i,j}\omega'_{ij}\left(p_{ij}^2 + q_{ij}^2\right) - \sum_{i=1}^{n-1} k_i q_{i,1} q_{i+1,1} \tag{3.2}$$

with

$$\omega'_{i,1} = \omega_1 + k_i - \langle k_i\rangle + k_{i-1} - \langle k_{i-1}\rangle \tag{3.3}$$

for the transporting mode $j = 1$ (the boundary term is omitted for $i = 1$ and $i = n$), and

$$\omega'_{ij} = \omega_j + \delta\omega_{ij} \tag{3.4}$$

for the higher-frequency modes $j \geq 2$. The particular spectrum is chosen as $\{\omega_1, \omega_2, \omega_3, \omega_4\} = \{0.7, 1.4, 2.8, 5.6\}$ (in units of k_BT), which is a series of Fermi resonances to facilitate IVR despite the small number of modes. The lowest-frequency (transporting) mode is a "classical" mode with $\omega_1 < k_BT$, all other modes are quantum-like with $\omega_j > k_BT$.

The numbers $\delta\omega_{ij}$ mimic disorder and are randomly chosen from a Gaussian distribution with a standard deviation $\langle\delta\omega\rangle = 0.02$. The intersite couplings k_i, responsible for transport along the chain, are chosen from an exponential distribution with a mean value $\langle k\rangle = 0.15$. To maintain the Fermi resonances (modulo disorder), the mean $\langle k\rangle$ at the boundaries of the chain and twice the mean $\langle k\rangle$ in the interior of the chain is subtracted from ω_1 (see Eq. (3.3)). Figure 3.2 shows the normal modes for a typical realization of the Hamiltonian. The high-frequency modes are all localized on the individual sites, whereas the set of transporting low-frequency modes delocalizes to a certain extent along the chain.

The harmonic Hamiltonian Eq. (3.2) decouples the high-frequency modes ($j \geq 2$) from the low-frequency transporting modes ($j = 1$). Therefore, to promote IVR within each site i, an additional cubic anharmonicity [73,74] with a common anharmonicity parameter Δ is introduced , which efficiently couples resonant states:

$$H^{(3)} = \Delta \sum_{i,j,k} q_{ik} q_{ij}^2 \tag{3.5}$$

The effect of this cubic anharmonicity is easiest to understand when expressing the position coordinates q in terms of creation and annihilation operators. The resulting coupling terms $b_{ik} b_{ij}^\dagger b_{ij}^\dagger$ and $b_{ik}^\dagger b_{ij} b_{ij}$ (see Appendix A) de-excite one oscillator by one quantum, and at the same time excite the other oscillator by two quanta, or vice versa, which strongly couples these two modes. Since the individual modes are Fermi-resonant by construct, i.e. $\omega_{j+1} = 2\omega_j$, the respective states efficiently start to mix [75].

The complete Hamiltonian, resulting from Eqs. (3.2) and (3.5), is written as:

$$H = H^{(2)} + H^{(3)} \tag{3.6}$$

3.2.2 Classical simulations

For the classical MD simulations, the Hamilton equations are time-propagated as

$$p_{ij}(t + \Delta t) = p_{ij}(t) + F_{ij}(t)\Delta t \tag{3.7}$$

$$\begin{aligned} q_{ij}(t + \Delta t) &= q_{ij}(t) + v_{ij}(t + \Delta t)\Delta t \\ &= q_{ij}(t) + \omega'_{ij} p_{ij}(t + \Delta t)\Delta t, \end{aligned} \tag{3.8}$$

with the force $F_{ij} = -\partial V/\partial q_{ij}$ deduced from the potential energy function and an integration time step $\Delta t = 0.01$.

The system is initialized by assigning the total energy $E = k_B T_0$ to each mode entirely in form of kinetic energy. For this purpose the starting conditions are chosen to be $q_{ij} = 0$ and p_{ij} is taken from a Gaussian distribution with a standard deviation $\sqrt{2k_B T_0/\omega'_{ij}}$, revealing a Boltzmann distribution in 1D. According to the virial theorem (which applies approximately since the anharmonic term $H^{(3)}$ is small), the average total energy is distributed equally between kinetic and potential energy after equilibration. In order to obtain an equilibrated, thermalized ensemble the system is time-propagated for sufficiently long time. Since the initial guess is already close to a thermalized system an equilibration run of the duration $t = 25000$ turns out to be adequate and no further changes can be observed hereafter. Thus, a thermalized ensemble with a total energy of $E = 4k_B T_0$ per site is obtained, which is equally distributed over all modes (i.e., $E = k_B T_0$ per mode).

After the equilibration step, excess energy is deposited at site i=1 by scaling the instantaneous momenta $p_{1,j}$ and spatial coordinates $q_{1,j}$ of all 4 modes $j = 1, 2, 3, 4$ uniformly upward (compare Ref. [23]) so that the heating site remains thermal but at a higher temperature. Since the total energy E is quadratic in p and q a scaling factor $\sqrt{T/T_0}$ is used for both coordinates, whose values are chosen close to the experiment; in the case of high-energy excitation it is $\sqrt{3}$ in the case of low-energy excitation $\sqrt{1.1}$ so that the energy of the heating site jumps from T_0 to $3T_0$ ($\Delta T = 2T_0$) or $1.1T_0$ ($\Delta T = 0.1T_0$), respectively.

The system then evolves freely and the total energy of each site is calculated as a function of time. Only the local, first term of Eq. (3.2) is evaluated to calculate the total energy, while the intersite couplings on the main chain $\sum_{i=1}^{n-1} k_i q_{i,1} q_{i+1,1}$ and the small anharmonic part $H^{(3)}$ (Eq. (3.5)) are neglected. The results are averaged over an ensemble of 3000-30000 individual trajectories, each initialized with different random initial conditions and random Hamiltonians generated as described above.

The quadratic-cubic Hamiltonian (Eq. (3.6)) is not binding, resulting in a small probability that trajectories escape from the local minimum around q_i=0. To prevent this from happening, a small quartic term

$$H^{(4)} = \alpha\Delta \sum_{i,j,k} q_{ik}^2 q_{ij}^2 \tag{3.9}$$

with α=0.3 is added for the classical simulations. For the quantum-mechanical simulations this quartic compensation term is redundant because the accessible phase space is intrinsically restricted due to the truncation of the basis (see next section).

3.2.3 Quantum simulations[†]

Matrix representation

For the quantum-mechanical simulations, the Hamiltonian (Eq. (3.6)) is expressed in terms of creation and annihilation operators, $b_{ij} = (\hat{q}_{ij} + i\hat{p}_{ij})/\sqrt{2}$ and $b_{ij}^\dagger = (\hat{q}_{ij} - i\hat{p}_{ij})/\sqrt{2}$, a detailed derivation can be found in Appendix A:

$$\begin{aligned} H^{(2)} &= \sum_{i,j} \omega'_{ij} \left(b_{ij}^\dagger b_{ij} + \frac{1}{2} \right) - \frac{1}{2} \sum_{i=1}^{n-1} k_i \left(b_{i,1}^\dagger b_{i+1,1}^\dagger + b_{i,1}^\dagger b_{i+1,1} + c.c \right) \\ H^{(3)} &= \Delta \frac{1}{\sqrt{8}} \sum_{i,j,k} \left(b_{ik}^\dagger b_{ij}^\dagger b_{ij}^\dagger + b_{ik}^\dagger b_{ij}^\dagger b_{ij} + b_{ik}^\dagger b_{ij} b_{ij}^\dagger + b_{ik}^\dagger b_{ij} b_{ij} \right) + c.c. \end{aligned} \tag{3.10}$$

When describing bilinear couplings, nonquantum-conserving terms, such as $b_{i,1}^\dagger b_{i+1,1}^\dagger$ are commonly neglected in the harmonic Hamiltonian $H^{(2)}$ because they couple states that are far apart in energy [75]. However, due to the relatively strong intersite coupling in the present system, these terms are no longer completely negligible and consequently retained.

The wave function is expanded in a basis of product states of the individual modes:

$$\Psi = \sum_{\{n_{ij}\}} c_{\{n_{ij}\}} |n_{1,1}, n_{1,2}, ...n_{nm}\rangle \tag{3.11}$$

with

$$|n_{1,1}, n_{1,2}, ...n_{nm}\rangle \equiv \prod_{i,j} \left(b_{i,j}^\dagger \right)^{n_{ij}} |0\rangle \tag{3.12}$$

Here, $c_{\{n_{ij}\}} \equiv c_{n_{1,1},n_{1,2},....n_{nm}}$ is a "vector" with $n \times m$ indices, the n_{ij} are the corresponding occupation numbers and $|0\rangle$ is the vacuum state. The dimension of the basis, in principle, is $\prod_{ij}(N_{ij}^{(max)} + 1)$ with $N_{ij}^{(max)}$ the maximal number of quanta on mode (i, j). In order to reduce the basis to a manageable size, only combination modes below a certain cutoff energy are retained. With a cutoff energy of $\epsilon_{cut} = 11$, about 95% of the norm of a

---

[†] The quantum-mechanical simulations were performed by Peter Hamm.

thermalized wave function (Eq. (3.13), below) are within the configuration space spanned by this basis. This cutoff results in ca. 2×10^5 to 10^6 basis states, depending on the particular realization of the Hamiltonian, i.e., the random choice of numbers $\delta\omega_{ij}$ and k_i.

The time-dependent Schrödinger equation is propagated using a Chebychev scheme [76]. This requires knowledge of upper and lower bounds of eigenstates of the Hamiltonian, which are computed beforehand by a few Lanczos iterations (the basis size is too large to completely diagonalize the Hamiltonian). The elementary operation in both the Chebychev scheme and the Lanczos algorithm is a matrix-vector product, whose computational cost scales like the number of elements of the sparse Hamilton matrix (≈ 10 times the dimension of the basis).

Equilibration and heating

As a first guess for a thermalized initial condition, the expansion coefficients are calculated as Boltzmann factors

$$c_{\{n_{ij}\}} = \frac{1}{\sqrt{N}} e^{-\frac{H_{\{n_{ij}\},\{n_{ij}\}}}{2k_B T_0}} e^{i\phi_{\{n_{ij}\}}} \tag{3.13}$$

using the diagonal elements of the Hamiltonian

$$H_{\{n_{ij}\},\{n_{ij}\}} = \sum_{ij} \omega'_{ij} \left(n_{ij} + \frac{1}{2} \right) \tag{3.14}$$

as an estimate of the energies of the corresponding modes. N is a normalization factor, and the phases $\phi_{\{n_{ij}\}}$ are chosen from a random distribution between 0 and 2π. Averaging over many such wave functions with different random choices of the phases $\phi_{\{n_{ij}\}}$, the resulting density matrix would be diagonal and represent a thermal ensemble. In order to further equilibrate the wave function in the presence of the off-diagonal terms of the Hamiltonian (the intersite couplings k_i and the anharmonic terms Δ), the wave function is time-propagated for sufficiently long time, as already described for the classical simulations.

After the equilibration step, all modes at site i=1 are heated with temperature jumps that are the same as in the classical case. To this end, the reduced probability densities $\rho_{n_{ij}}$ of the various quantum states n_{ij} of the individual modes (i, j) are first calculated for the equilibrated state by tracing out the other degrees of freedom. Each expansion coefficient of the equilibrated wavefunction is then replaced by

$$c_{\{n_{ij}\}} \to c_{\{n_{ij}\}} \times \prod_j \rho_{n_{1j}}^{\delta\beta/2}, \tag{3.15}$$

where the index of the product runs over all components of the vector $c_{\{n_{ij}\}}$ related to site #1. The phases of the individual components are retained and the wave function is renormalized afterwards. This expression corresponds to a heating from the base temperature $\beta_0 \equiv 1/k_B T_0 = 1$ to an elevated temperature $\beta = 1 - \delta\beta$ for all modes on site #1, which can easily be seen if the reduced probability densities $\rho_{n_{ij}}$ would strictly follow Boltzmann distributions. In the present finite system, where the population deviates somewhat from a Boltzmann distribution, the same is achieved by perturbing the equilibrium wave function as little as possible.

The wave function prepared in this way is time-propagated, and the energy on each site is calculated at each time step:

$$E_i^{(tot)} = \sum_{j,n_{ij}} \rho_{n_{ij}} \omega'_{ij} n_{ij} \tag{3.16}$$

The result is averaged over several nonequilibrium trajectories for different set of random numbers $\delta\omega_{ij}$ and k_i in the Hamiltonian Eq. (3.2), as well as random phases $\phi_{\{n_{ij}\}}$ in the initial condition Eq. (3.13), thereby realizing a thermal average over a disordered inhomogeneous ensemble. Due to the high computational cost, the number of trajectories is small (12 trajectories), nevertheless, the essential characteristics are contained in every single trajectory. Also, in contrast to the classical simulation, a single quantum wave function already contains a significant amount of phase-space averaging through the initial condition Eq. (3.13).

3.3 Results

3.3.1 Quantum simulations

Figure 3.3 shows the energies of sites #1-5 after a temperature jump at site #1 of $\Delta T = 0.1T_0$ (panel a) and $\Delta T = 2T_0$ (panel b) for a small anharmonicity $\Delta = 0.025$. The ratio between coupling Δ and disorder $\langle\delta\omega\rangle = 0.02$ determines the resonance condition of the Fermi resonances. A value $\Delta/\langle\delta\omega\rangle \approx 1$ is just at the borderline between completely switching off IVR and efficient IVR.

Two relaxation phases can be identified: first, a very fast initial step until $t \approx 10$ (i.e., 250 fs in real units), which deposits energy up to site 3 (see Fig. 3.3, inset). Some residual coherence initiated by that initial process survives until $t \approx 1000$ with a typical frequency of ≈ 0.3. The time scale of the initial drop scales with the intersite couplings k_i and, therefore, it can be attributed to ballistic energy transport along the chain. This means, if the intersite couplings k_i and the frequency of the transporting modes ω_1 were constant, the system would be perfectly ordered so that the lowest frequency modes would be phonons, in the limit of an infinite chain. With the given initial condition, a localized wavepacket is deposited at site #1, which then would propagate along the chain in a wave-like manner. The time scale of this ballistic transport would be given by the dispersion of the phonon, which is approximately $4k_i$. The present chain system, however, is constructed with disorder in k_i and ω_1, which causes the low-frequency modes to partially localize (compare Sec. 2.2). Nevertheless, to the extent the normal modes are still delocalized (Fig. 3.2), vibrational energy transport can be phonon-like over a certain distance.

Second, on a significantly slower time scale, a further relaxation process is observed that proceeds until $t \approx 50000$ (1.2 ns in real units; it is difficult to specify a time constant because the process is nonexponential). It should be noted that relaxation is not complete even for times $t \gg 50000$ (data not shown), i.e., the energies of the five sites do not converge to the same value, which they should in average. It can be shown that the size of the remaining offset decreases as the size of the system increases, which is why it is attributed to the finiteness of the system and consequently the discreteness of the energy spectrum.

Figure 3.4 shows the same simulations for a significantly larger anharmonicity parameter $\Delta = 0.07$. Due to the increased ratio of coupling versus disorder ($\Delta/\langle\delta\omega\rangle = 3.5$)

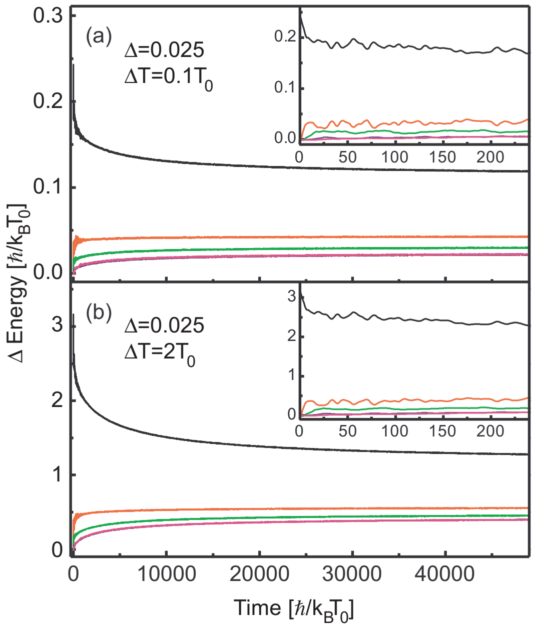

Figure 3.3: Quantum results for low anharmonicity ($\Delta = 0.025$). Energies of sites #1-5 (in black, red, green, blue, and magenta) after a temperature jump at site #1 of $\Delta T = 0.1T_0$ (panel a) and $\Delta T = 2T_0$ (panel b). The inset shows the same on an expanded time axis.

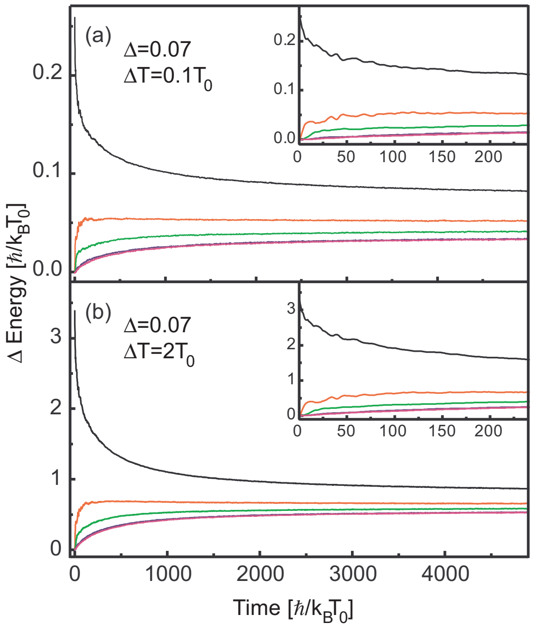

Figure 3.4: Quantum results for high anharmonicity ($\Delta = 0.07$). Energies of sites #1-5 (in black, red, green, blue, and magenta) after a temperature jump at site #1 of $\Delta T = 0.1T_0$ (panel a) and $\Delta T = 2T_0$ (panel b). The inset shows the same on an expanded time axis.

intrasite IVR is much more efficient in this case. Qualitatively, the results are comparable to the low-anharmonicity case, exhibiting two relaxation phases. However, the slower phase now is about ten times faster than in Figure 3.3 (note the different time scales), and the coherences are less pronounced.

Careful inspection of the relaxation in the low-anharmonicity case (Fig. 3.3) shows that the responses after a small (Fig. 3.3a) or a large (Fig. 3.3b) temperature jump are not exactly the same. This is made clearer in Figure 3.5a which directly compares the cooling of the initially heated site #1 in the two cases. Both curves are normalized so that they coincide at $t = 0$ and asymptotically for large times. In a relative sense, the initial ballistic component is larger for the small temperature jump. Interestingly, when increasing the anharmonicity, the difference between the two cases essentially vanishes (Fig. 3.5b).

Especially for the high-anharmonicity case, a propagation effect can be identified, which becomes clear in Figure 3.4 and also Figure 3.6a, which shows the same data on an enlarged scale: the farther a site is away from the initially heated site #1, the longer it takes until vibrational energy appears. Site #2 is, in fact, overshooting a little, as it is first populated from site #1 and later on depopulated toward the rest of the chain. To investigate the origin of this propagation effect, the simulation of Figure 3.4 was repeated with the anharmonic couplings of sites #2-5 switched off, and thereby preventing the possibility of intrasite IVR on these sites (intrasite IVR in the heated site #1 is still possible, so that the deposited energy can be transferred into the transporting modes).

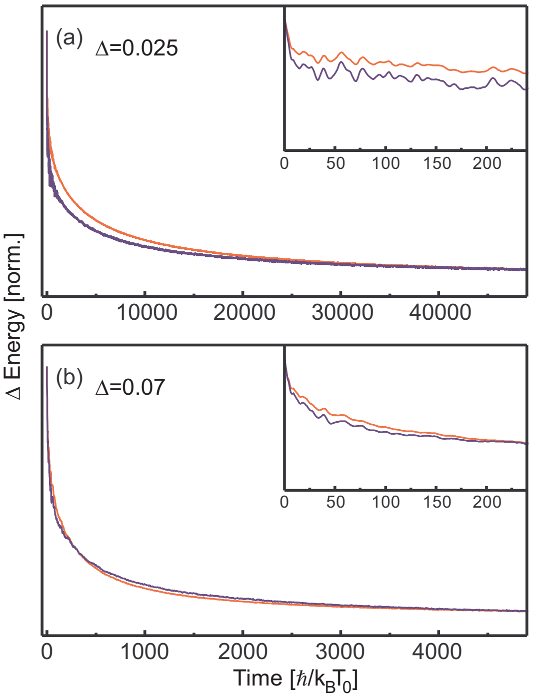

Figure 3.5: Quantum results: Comparison of the cooling of the initially heated site #1 after a small (blue) and large (red) temperature jump.

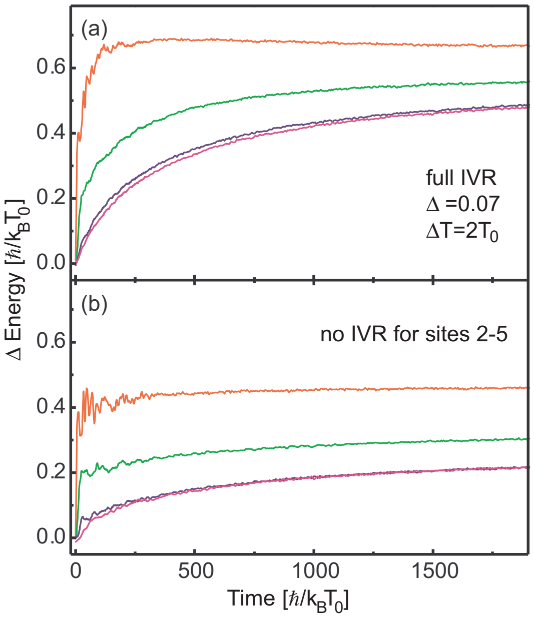

Figure 3.6: Quantum results: (a) For comparison, the same data as in Fig. 3.4b for sites #2-5 (in red, green, blue, and magenta) are plotted on an enlarged scale. (b) Corresponding results after switching off the anharmonic couplings of sites #2-5.

The obtained result is shown in Figure 3.6b. With regard to the initial, ballistic phase, both simulations reveal essentially the same step for sites 2 and 3. However, later on the energy content of all sites #2-5 rises more or less in parallel and is decreased compared to the case with full IVR allowed (Fig. 3.6a). Hence, when IVR is switched off, energy dissipating out of site #1 appears in all sites #2-5 essentially simultaneously and the overall transport process becomes less efficient.

3.3.2 Classical simulations

Figure 3.7 shows the corresponding results obtained from a classical simulation for small anharmonicity $\Delta = 0.025$. Once again two phases can be identified, i.e., a fast ballistic one taking place on a time scale of $t \approx 10$ that deposits energy up to site 3, and a subsequent nonexponential relaxation step on a slower time scale up to $t > 170000$ (4 ns in real units). The latter again shows a propagation effect, i.e., a sequential response of the sites according to their distance from the heating site. As already discussed in the introduction to this chapter, relaxation rates obtained from classical MD simulations are significantly slower as compared to the quantum case. Therefore, in contrast to the quantum-mechanical simulations the relaxation process is still ongoing even for times $t \gg 170000$. However, it can be verified that the system, when propagated classically, always equilibrates to a common energy value (data not shown).

The corresponding simulations for a high anharmonicity parameter $\Delta = 0.07$ are shown in Figure 3.8. The ballistic process is found to happen on about the same time

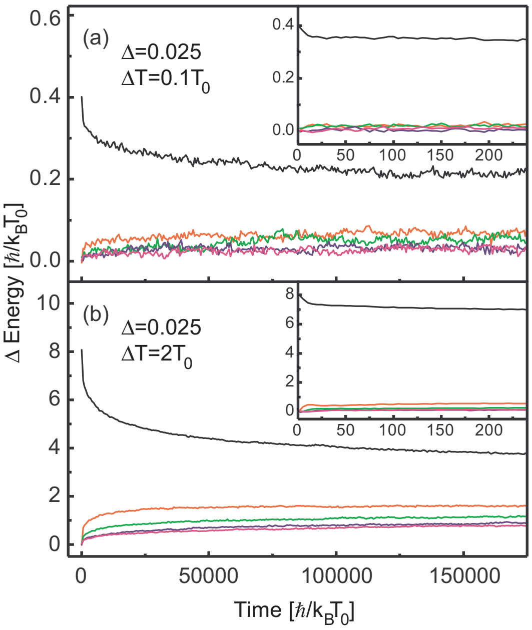

Figure 3.7: Classical results for low anharmonicity (Δ=0.025). Energies of sites #1-5 (in black, red, green, blue, and magenta) after a temperature jump at site #1 of ΔT=0.1T_0 (panel a) and ΔT=2T_0 (panel b). The inset shows the same on an expanded time axis.

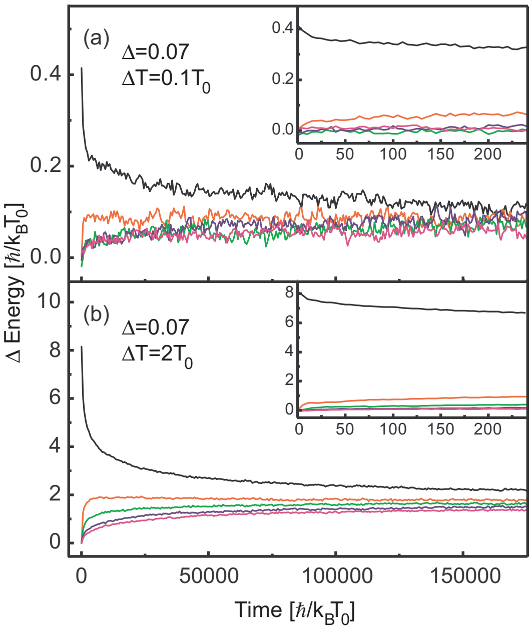

Figure 3.8: Classical results for high anharmonicity (Δ=0.07). Energies of sites #1-5 (in black, red, green, blue, and magenta) after a temperature jump at site #1 of ΔT=0.1T_0 (panel a) and ΔT=2T_0 (panel b). The inset shows the same on an expanded time axis.

scale as for low anharmonicity, i.e., $t \approx 10$. However, the subsequent relaxation is much faster so that equilibration process is much more advanced at $t = 170000$.

Figure 3.9 shows the direct comparison for the relaxation of the heating site #1 after high- and low-energy excitation, normalized as described before. In contrast to the quantum-mechanical simulations (Fig. 3.5), the differences between high- and low-energy excitation are essentially not present (within signal-to-noise ratio), even for the low anharmonicity parameter Δ (Fig. 3.9).

3.3.3 Classical simulations with quantum-like initial conditions

Sections 3.3.1 and 3.3.2 showed that the cooling behavior in the quantum-mechanical MD simulations depends somewhat on the amount of initially deposited energy (Fig. 3.5a), whereas the classical simulations cannot reproduce this effect (Fig. 3.9a). Apparently, the different behavior has its origin already at very early times ($t \approx 10$). One might therefore assume that the reason for the difference is the way classical and quantum mechanics distribute thermalized energy over the various modes.

In order to test this hypothesis, the system is prepared with quantum-mechanical initial conditions for the heating site #1, but is subsequently propagated according to classical mechanics. In quantum mechanics, the average energy per mode is

$$\langle E \rangle = \hbar\omega \left(\frac{1}{e^{\hbar\omega/k_B T} - 1} + \frac{1}{2} \right) \tag{3.17}$$

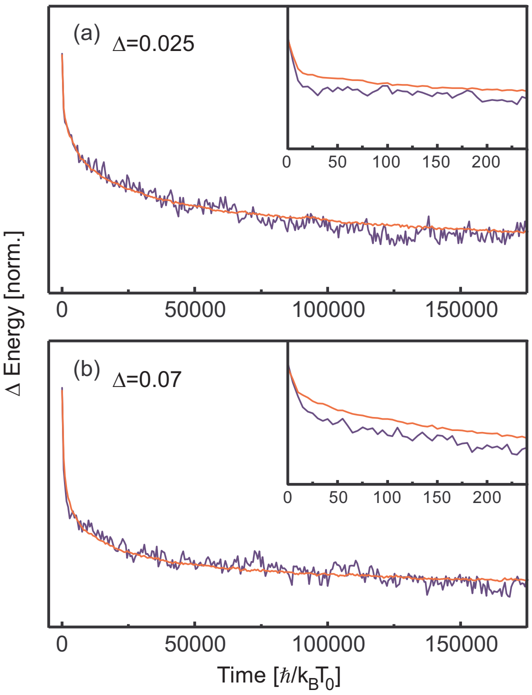

Figure 3.9: Classical results: Comparison of the cooling of the initially heated site #1 after a small (blue) and large (red) temperature jump.

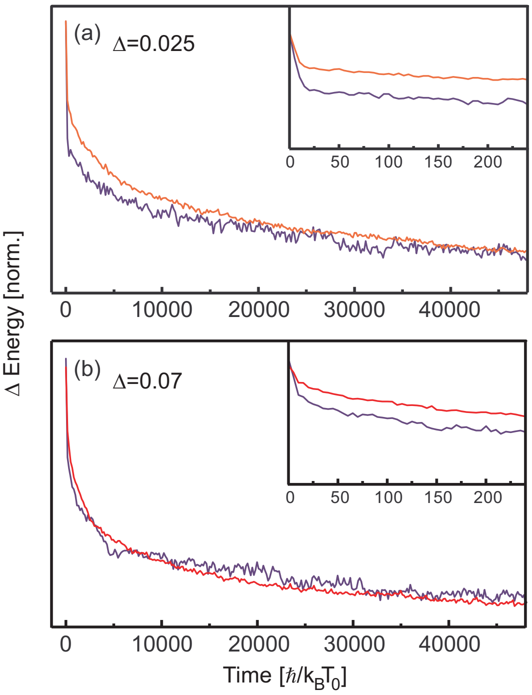

Figure 3.10: Classical results with quantum-like initial conditions: Comparison of the cooling of the initially heated site #1 after a small (blue) and large (red) temperature jump.

with the second term corresponding to zero-point energy. Assigning zero-point energy to all modes is problematic in classical mechanics because it would dissipate and overheat the system. Therefore, the zero-point energy is replaced by $k_B T_0/\hbar\omega$, which is the long time limit in classical mechanics. In order to mimic heating of the ensemble after the initial equilibration step, the positions q and momenta p of the individual modes are scaled up accordingly.

Comparing the cooling behavior of site #1 after high- and low-energy excitation, an effect very similar to the quantum case (Fig. 3.5) is obtained: for small anharmonicity $\Delta = 0.025$ the initial drop of energy during the ballistic phase is larger in a relative sense after low energy excitation (see Fig. 3.10a). However, when the anharmonicity parameter is increased to $\Delta = 0.07$, the difference between both responses essentially disappears (see Fig. 3.10b).

3.4 Discussion

In the previous section vibrational energy transport was calculated in classical and quantum-mechanical MD simulations, for high- and low-energy excitation, and with intrasite IVR mimicked by high and low cubic anharmonicity – once even completely suppressed. Comparing the results of these simulations, three important points can be extracted:

First, apart from the different time scales – which are related to the well-known fact that classical relaxations underestimate the energy relaxation rates and consequently equilibrate slower [69] – the differences between quantum-mechanical and classical simulations are very small and most probably not responsible for the deviations between experiments and simulations. Nevertheless, it is interesting to note that the classical simulations cannot reproduce the small excitation energy dependence of the heat propagation efficiency, which is found in Figure 3.9. The reason for the observed difference is the way classical and quantum mechanics distribute thermal energy over the various modes, i.e., the initial condition, and not the mechanism of anharmonic scattering. Also in a recent a perturbative treatment, the latter has been shown to be fairly similar in classical and quantum mechanics [69]. That means, by starting a classical simulation with quantum-like initial conditions (Eq. (3.17)), results very similar to a true quantum simulation are obtained. In classical mechanics, the energy in one particular mode scales linearly with temperature, independent of the frequency of the mode. Hence, in a relative sense, the dynamics with which energy diffuses out of a mode does not depend on the amount of energy. In quantum mechanics, in contrast, higher-frequency modes are hardly populated, and energy increases in a highly nonlinear manner upon heating. In a relative sense, higher-frequency modes receive more energy upon heating as compared to lower-frequency modes. Since the energy first has to cascade down the vibrational ladder, overall IVR is slower when more energy is initially deposited, which is observed in Figure 3.5a. For high anharmonicity values Δ, however, intrasite IVR becomes so efficient that these differences in the initially heated site level out quickly and do not play a role for the subsequent energy propagation process.

Second, as already speculated in the introduction to this chapter, on the short length scales of a few chemical bonds, IVR is the rate-limiting step in vibrational energy transport. There are two distinctively different time scales of transport, the first of which is governed by the chain coupling k_i and is very fast for the present choice of parameters ($t = 10$ or 250 fs in real units). It gives rise to the fast ballistic phase which is identical in classical and quantum mechanics since it works on the level of harmonic springs. The second, slower phase is governed by intrasite IVR. In a naive picture, one might assume that energy, once it is dissipated into the transporting low-frequency mode, should propagate along the chain instantaneously (ballistically). The simulations, however, show that sites #2-5 pick up energy in a sequential manner and on a time scale that is much slower than the ballistic process (Fig. 3.6a). This observation can be explained by the fact that vibrational energy is only trapped at a site, once anharmonic couplings dissipate it into higher-frequency modes by upward IVR (compare Fig. 3.2). Since the overlap of the harmonic wave functions along the transporting chain decreases with distance from the heated site #1, sites that are further away pick up energy slower, which gives rise to the observed propagation effect. When switching off the possibility of intrasite IVR, the propagation effect essentially vanishes, and energy dissipation is less complete (Fig. 3.6b).

The important point in this context, is that the time scale of the propagation effect is determined by IVR, which can be much slower than the actual transport along the chain. That explains one of the question raised in Section 3.1, namely, why the experimentally measured thermal diffusivity (2 $\text{Å}^2\text{ps}^{-1}$) [43] is so much slower than the values known for bulk materials (10-20 $\text{Å}^2\text{ps}^{-1}$) [6]. On the length scale of short peptides, intrasite IVR is the rate-limiting step. However, since intrasite IVR is length independent, transport along the chain is expected to become rate-limiting on larger length scales, in a way formulated for instance by Leitner and coworkers [6,14,18,19]. With the given experimental numbers, it can be estimated that this regime would be reached for molecular chains that are about $\sqrt{5}$ to $\sqrt{10}$ longer than the current system. The transition between both regimes is investigated in detail in the following Chapter 4.

Third, by reducing the anharmonicity and thereby the efficiency of intrasite IVR, the diffusive component can essentially be switched off, so that transport becomes ballistic. In this case, only the small fraction of energy that initially is directly deposited in the transporting modes can propagate, which happens very quickly (ballistically), but the overall amount of transferred energy is decreased. Hence, the presented model can intuitively explain why energy transport, when it becomes ballistic, is faster but at the same time less efficient. This interpretation is in perfect agreement with the speculation raised by Backus *et al.* in Ref. [52], except that the cause of IVR in the real molecular system is structural flexibility, i.e., a time-dependent molecular Hamiltonian which also can give rise to energy dissipation. In the present model system, in contrast, IVR is mimicked by a cubic anharmonicity in a static system.

3.5 Conclusion

Different from what was initially expected, quantum effects turned out to be of minor importance for the deviations between experiments and accompanying MD simulations. Nevertheless, the toy model presented in this chapter suggests an overall picture that unifies most of the experimental observations. Most important, it was demonstrated that the mechanism of vibrational energy transport on length scales of a few chemical bonds and time scales of a few picoseconds is distinctively different from heat diffusion on macroscopic scales, because vibrational energy does not necessarily thermalize completely within individual amino acid sites on the time scale of transport.

Based on this very general finding, light could be shed on all three questions raised in Chapter 1. First of all, it was shown that the energy transport properties of biomolecular chains are largely insensitive to the amount of initially deposited energy. Even time-propagating vibrational energy transport along a molecular chain in a fully quantum-mechanical simulation, which should be able to reproduce the potential excitation energy dependence of the thermal properties, does not show any significant effects.

Second, the model intuitively demonstrates how controlling the rate of intrasite IVR can switch vibrational energy transport from ballistic but inefficient to diffusive and efficient. When IVR is suppressed, only the energy that is already contained in the delocalized low-frequency modes can contribute to transport. Efficient intrasite IVR, in contrast, opens the channel for energy flow out of and into (!) the localized high-frequency modes, thus distributing vibrational energy efficiently over the entire biomolecule.

Finally, it was shown that on the given ultrashort length and time scales, IVR rather than the actual transport along the chain is the rate-limiting step, which significantly slows down the observed energy propagation speed. This explains why the experimentally measured thermal diffusivity is much lower than for bulk materials. However, the question still remains, why the MD simulations of real peptides cannot account for this effect and overestimate the true relaxation rate. This point will be revisited in the next chapter.

Chapter 4

Vibrational energy transport in the presence of IVR
Part II: Rate modeling

One of the suggestions of the previous chapter is that on the short length scale of a few chemical bonds *intra*site IVR rather than the actual *inter*site transport along the molecular chain determines the speed of vibrational energy transport. However, since IVR is chain-length independent, transport along the chain is expected to become rate-limiting at some point, thereby approaching the limit of an infinitely long peptide. This transition from an IVR-dominated, microscopic regime to a propagation-dominated, macroscopic regime is expected to occur on length scales about $\sqrt{5}$ to $\sqrt{10}$ larger than the model studied in the previous chapter. Due to the high computational costs, however, the MD simulations of the toy model could not be expanded into these dimensions. Therefore, in this chapter the introduced model is revisited and treated in a simple rate equation scheme, which practically can be applied to much longer molecular chains.

4.1 Model

MD simulations describe dynamical processes on a microscopic level; the obtained macroscopic properties like reaction and transport rates are averages over the underlying stochastic processes. Due to great detail of the calculations and the extensive averaging MD simulations are computationally costly. As a result, the toy model presented in Chapter 3 was limited to a chain consisting of only five amino acid sites, especially owing to the quantum-mechanical MD simulations. Therefore, this chapter gets back to the same model, which is now treated in a much simpler scheme working on the level of macroscopic transport rates. Whereas this model can no longer provide microscopic information on the energy transport process, it can be extended into dimensions where the transition between the intrasite- and intersite-dominated regime is expected to take place.

Along the lines of the previous chapter a one-dimensional chain of n sites is defined, each consisting of one transporting mode and three localized (“parking”) modes, as depicted in Figure 4.1. The distance between two adjacent chain sites is chosen as Δx=1. To mimic the delocalized low-frequency states, the transporting mode is coupled to its nearest neighbors with which it exchanges energy at a rate k_p (propagation along the chain). The

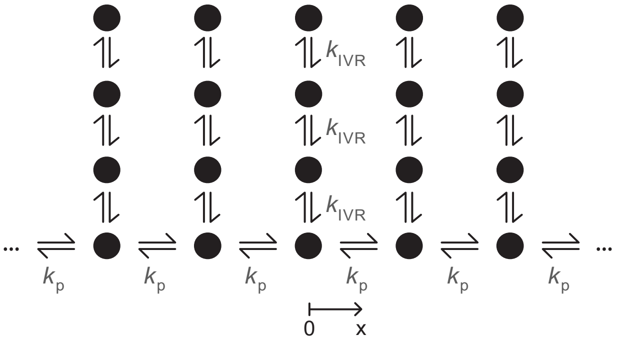

Figure 4.1: One-dimensional chain with n sites and m=4 modes per site. The transporting mode exchanges vibrational energy with its nearest neighbors at a propagation rate k_{p}. At each site, three higher-frequency ("parking") modes mimic intrasite IVR with rate k_{IVR}. The distance between two adjacent sites is Δx=1.

three other modes mimic localized high-frequency states and can only exchange energy within the respective site at rate k_{IVR} (intrasite IVR). To again mimic vibrational energy redistribution in a protein, a cascade-like connectivity of states, very similar to the normal mode distribution displayed in Figure 3.2, is chosen.

As shown in detail in Appendix C, the dynamics of such a system can be described by a rate equation scheme, where the coupling matrix K contains the energy transfer rates k. By solving the resulting set of coupled differential equations (Eq. (C.4)), the energy of each state can be calculated as a function of time.

The chain is locally heated at one single site by using a suitable nonequilibrium initial condition. For this purpose vibrational energy is deposited in equal parts into each of the four modes of the heated site, thus mimicking a classically thermalized site. To prevent potential boundary effects the central site of the chain is chosen for heating. The length of the chain is chosen to be sufficiently large so that the system cannot equilibrate on the time scales of interest, ensuring that the energy transport does not stop.

4.2 Results

As discussed in Chapter 2, the mean square displacement $\langle x^2 \rangle$ in a diffusive process increases linearly with time. In particular, it can be shown that for the one-dimensional case the underlying proportionality constant is twice the diffusion constant, i.e., $2D$ (a detailed derivation of this relation is given in Appendix B):

$$\left\langle x^2 \right\rangle (t) = 2Dt \tag{4.1}$$

In the present model, most of the energy initially is deposited in the localized high-frequency modes which cannot contribute to transport. Since this energy first has to relax into the low-frequency mode before it can be transported along the chain, one could expect that the thermal diffusivity initially is low, like on the short length scales covered by the MD simulations of the toy model, and increases to its final bulk value on a time scale determined by the rate of intrasite IVR. This means in particular, that the thermal diffusivity D is expected not to be a constant.

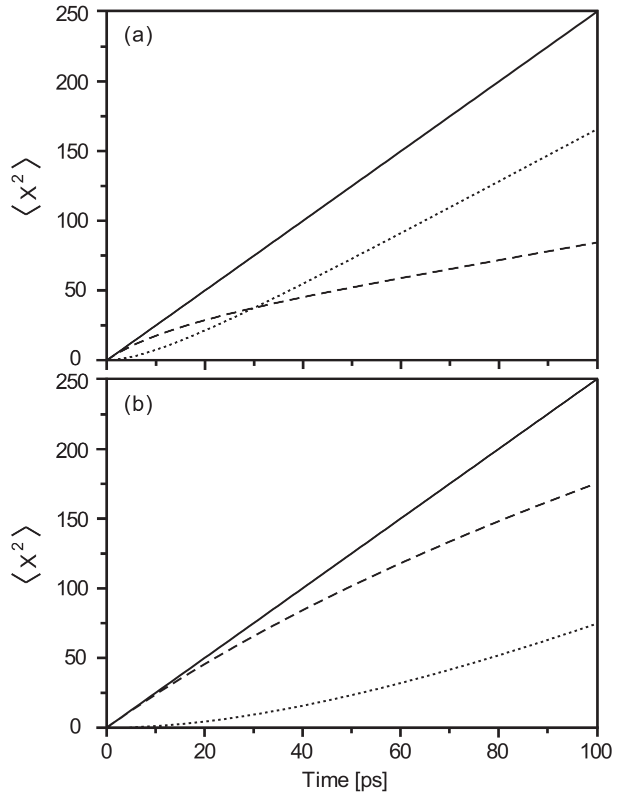

Figure 4.2: Mean square displacement of the energy $\langle x^2 \rangle$ as a function of time t; the thermal diffusivity D is the half value of the slope (Eq. (4.1)). The presented results were obtained for a propagation rate $k_\mathrm{p} = (0.2\ \mathrm{ps})^{-1}$ and (a) a fast IVR rate of $k_\mathrm{IVR} = (10\ \mathrm{ps})^{-1}$ or (b) a slow IVR rate of $k_\mathrm{IVR} = (100\ \mathrm{ps})^{-1}$. The time behavior of the low-frequency transporting modes ($\langle x^2_\mathrm{trans} \rangle$, dashed lines) and the high-frequency parking modes ($\langle x^2_\mathrm{park} \rangle$, dotted lines) depends on k_IVR. For the time behavior of the total site ($\langle x^2_\mathrm{site} \rangle$, solid lines), which is the sum of the contributions of transporting and parking modes, the effect of k_IVR cancels out.

To assess the thermal diffusivity D of the model system, the mean square displacement of the energy $\langle x^2 \rangle$ is calculated as a function of time for different propagation rates k_p and IVR rates k_IVR. Plotting $\langle x^2 \rangle$ vs. t, the thermal diffusivity D is obtained from half the value of the slope (Eq. (4.1)). Figure 4.2 shows the results obtained for the entire sites $\langle x^2_\mathrm{site} \rangle$ (solid lines), and broken down into the contributions of the low-frequency transporting modes $\langle x^2_\mathrm{trans} \rangle$ (dashed lines) as well as the high-frequency parking modes $\langle x^2_\mathrm{park} \rangle$ (dotted lines).

As expected, for very early times only vibrational energy that is initially deposited in the transporting modes can contribute to energy diffusion. Therefore, the total thermal diffusivity at ultrafast time scales can be attributed entirely to the transporting modes, the contribution of which decreases with time. The contribution of the parking modes, in contrast, initially is low and increases to its final value on a time scale determined by the rate of intrasite IVR. This becomes clear from comparing the results obtained for a fast IVR rate ($k_\mathrm{IVR} = (10\ \mathrm{ps})^{-1}$, Fig. 4.2a) and a slow IVR rate ($k_\mathrm{IVR} = (100\ \mathrm{ps})^{-1}$, Fig. 4.2b); the faster the IVR rate the sooner the high-frequency modes can participate in energy transport.

Very counterintuitively though, the effects of the initially enhanced contribution of the transporting mode and the delayed contribution of the parking modes exactly compensate each other so that $\langle x^2_{\text{site}} \rangle$ increases linearly in time. Hence, the total vibrational energy propagates in a diffusive manner, although the individual contributions of transporting and parking modes do not. The complexity of the IVR process within the sites, although it is rate-limiting on these length and time scales, is completely hidden. The overall thermal diffusivity D is not influenced by the speed of intrasite IVR and has a constant value:

$$D = \frac{c_{\text{trans}}}{c_{\text{total}}} \; k_{\text{p}} \Delta x^2 \; = k'_{\text{p}} \Delta x^2 \tag{4.2}$$

Hence, one seems to observe a diffusive process on a simple 1D chain with some effective propagation rate k'_{p}, that equals the bulk value even at short times. The effective propagation rate k'_{p} is the transport rate along an unbranched 1D chain k_{p} weighted with the ratio of the heat capacity of transporting versus total number of modes at a site i, $c_{\text{trans}}/c_{\text{total}}$ (for the given system this ratio is 1/4). The more parking modes are included in the individual sites of the chain, the less energy is available for propagation in the transporting modes. Hence, intrasite IVR influences the population of the transporting modes, and thus the amount of vibrational energy that can be transported along the chain, but the transport speed depends only on k_{p} but *not* on k_{IVR}. This is true even for very short times $\ll k^{-1}_{\text{IVR}}$.

This means that under the given circumstances the thermal diffusivity D is a constant and no transition between the ultrashort regime and the bulk regime can be observed. It can be shown that Eq. (4.2) always holds for any connectivity of parking modes including branches etc., if only the initial condition is an equilibrium state of each site (see Appendix C). That is, the temperature at one site might be elevated as compared to the other sites, but the energy is equilibrated within that one site. In the present example, the forward and backward rates between each two modes were assumed to be identical, which implicitly implies an identical heat capacity of all modes. That is the case for low-frequency, classical modes with $\hbar\omega \lesssim k_B T$, but not for higher-frequency modes. However, the quantum-mechanical heat capacity of higher frequency modes can be taken care of by adjusting the ratio of forward and backward rates accordingly, and again, this would not affect the result of Eq. 4.2.

The competing effects between parking and transporting modes always cancel out when averaging equally over the energy content of all vibrational modes of one site. While all modes can easily be considered when starting from an MD simulation (in fact, one commonly averages over all modes to achieve better statistics), the same is very difficult to implement in a real experiment. Experimentally, the amount of vibrational energy in the vicinity of a peptide unit is measured by probing the transient redshift of a localized C=O mode. The physical origin of this thermometer is the well-known Dunham expansion of the vibrational energy

$$E = \sum_i \hbar\omega_i \left(n_i + \frac{1}{2} \right) + \sum_{ij} x_{ij} \left(n_i + \frac{1}{2} \right) \left(n_j + \frac{1}{2} \right), \tag{4.3}$$

where the ω_i are the harmonic frequencies of the various modes of a molecule, n_i their occupation numbers, and x_{ij} the anharmonic constants. The C=O reporter mode itself will hardly be excited at the relevant temperatures because of its high frequency (≈1650 cm^{-1}). Nevertheless, if lower-frequency modes get thermally excited when vibrational energy is transferred along the peptide backbone, then the C=O reporter mode will still experience a frequency shift through the anharmonic coupling terms $x_{\mathrm{CO},j}$ [47]:

$$\Delta\omega_{\mathrm{CO}} = \sum_j x_{\mathrm{CO},j} n_j \tag{4.4}$$

Whereas transition frequencies can be determined with reasonable precision from experiments and simulations, the calculation of anharmonic constants is still very challenging [77]. Nevertheless, as discussed in Section 2.3, localized high-frequency modes preferably couple to other localized modes that overlap in space, while the anharmonic coupling between a localized and a delocalized mode is typically very small [17]. Therefore, one can assume that the local C=O thermometer in the time-resolved laser experiments tentatively overestimates the contribution of other localized parking modes and does not sufficiently account for the energy in the delocalized transporting modes. In such a scenario the contributions of the transporting modes and the parking modes would no longer be equally weighted. Hence, the measured thermal diffusivity would be dominated by the localized high-frequency modes that receive vibrational energy later, which consequently would lead to a decreased thermal diffusivity at early times.

To clarify this effect, Figure 4.3a shows the same simulation as Figure 4.2a but now with the transporting modes underestimated by an arbitrary factor of 10, i.e. assuming that the anharmonic constants between the C=O reporter mode to transporting modes are in average 10 times smaller than to other parking modes. In contrast to Figure 4.2a, the thermal diffusivity is no longer constant, that is, the slope changes. The thermal diffusivity at early times is low and increases to its final value on a time scale determined by k_{IVR}, as predicted above. The transition between both regimes is most obvious in a double logarithmic plot of $\langle x^2_{\mathrm{site}} \rangle$ versus t, which is shown in Figure 4.3b. Two regimes can be identified, in both of which propagation is diffusive, indicated by a slope of 1 in the double logarithmic representation. On short length and time scales the apparent thermal diffusivity is reduced by the weighting factor 10 and asymptotically approaches its higher bulk value. Hence, Figure 4.3 exactly shows the behavior that was already predicted in Chapter 3, however a weighting factor between the transporting and parking modes is required as an additional ingredient to reproduce this effect.

4.3 Discussion

If vibrational energy within an individual amino acid residues would remain thermalized at all times (i.e., in the limit of very fast k_{IVR}), their entire time-dependent energy content can be extracted from any vibrational mode because all modes are equilibrated. On very fast time scales, however, intrasite IVR is rate-limiting so that vibrational energy does not thermalize on the time scale of transport. When vibrational excess energy is transported along the peptide backbone the low-frequency transporting modes receive energy directly by thermal excitation. The higher-frequency modes, on the other hand, pick up energy later when they are excited by intrasite IVR from the transporting modes. Under such conditions it becomes important which vibrational modes are used to estimate the residue energy of an amino acid site. If the energy is measured with a local “thermometer” mode that preferably couples to higher-frequency modes, the obtained value for the thermal

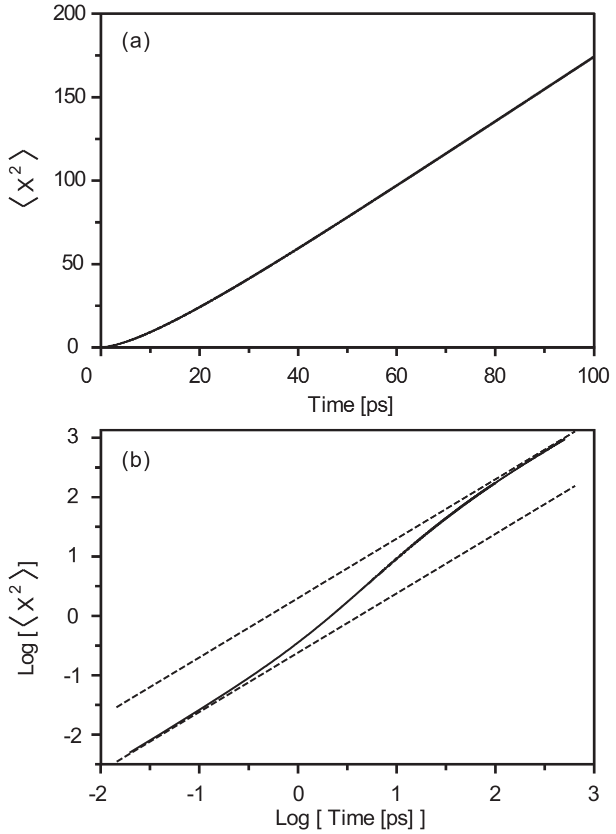

Figure 4.3: Same calculation as in Fig. 4.2a, i.e., $k_\mathrm{p} = (0.2\ \mathrm{ps})^{-1}$ and a slow IVR rate $k_\mathrm{IVR} = (10\ \mathrm{ps})^{-1}$, but with the transporting modes underestimated by a factor of 10. (a) The mean square displacement of the energy of the entire site $\langle x^2_\mathrm{site} \rangle$ plotted as a function of time now shows biphasic behavior. (b) The transition between two regimes with different heat diffusion constants D can be nicely seen in a double logarithmic plot. Dashed lines with slope 1 are plotted to guide the eye.

diffusivity initially is low and increases first when IVR has redistributed the energy within a site. Only if a vibrational reporter mode was equally sensitive to the bath of all other thermally occupied modes such effects would chancel out when averaging over the entire amino acid site.

The fact that C=O modes have a higher sensitivity for other localized higher-frequency modes leads to an underestimation of the delocalized transporting modes, the effect of which was mimicked by a weighting factor in the simulations. Consequently, the transient redshift of a localized C=O mode does not reflect the energy of the entire amino acid site and, in particular, occurs with some delay after the rise of the total residue energy. This finding provides the missing puzzle piece for one of the questions raised in Chapter 1, namely, why the MD simulations of the real peptide revealed a transport rate that is about a factor of five faster than the experimentally measured value. The simulations of the toy model presented in the previous chapter, in principle, could already explain all experimental findings, but not resolve why the MD simulations of the real peptide were unable to reproduce them. The reason is simply that the experimentally measured observable, i.e. the transient redshift, does not reflect the overall residue energy, which,

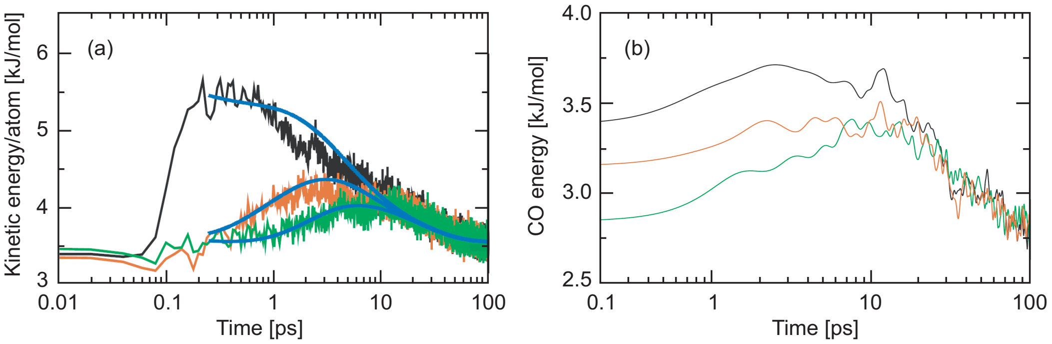

Figure 4.4: Nonequilibrium MD simulations of energy transport in a peptide helix performed by Stock and coworkers [78]: time evolution of the energy of sites #1 (black), #3 (red), and #5 (green) of the peptide, (a) calculated as an average over the entire amino acid site, and (b) calculated for the local C=O vibrational mode only. The time evolution of the energies obtained from the modified MD simulations is significantly slower (note the different time axes of the two subfigures), resulting in lower energy transport rates that agree much better with the experimentally measured values. The figures were kindly provided by Gerhard Stock; reprinted with permission from Ref. [78]. Copyright © (2010), American Institute of Physics.

however, was the basis for all MD simulations. As a result, the thermal diffusivity at ultrafast time scales extracted from those simulations was too fast. Furthermore, when averaging the energy content over entire amino acid sites the influence of IVR cancels out (compare solid lines in Figure 4.2), so that properties related to the temperature dependence of IVR (e.g., the switching from diffusive to ballistic transport) cannot be reproduced.

Based on these ideas, Stock and coworkers modified and reran their classical MD simulations of energy transport through the real peptide [78]. Instead of simulating the total residue energy of the amino acid sites, they attempted to calculate a quantity that closer resembles the experimentally measured observable. However, calculating the transient redshift of the C=O modes is not feasible because, as already mentioned above, the underlying anharmonic constants are difficult to obtain. Therefore, the authors of Ref. [78] resorted to calculate the time evolution of the energy of the localized C=O modes. Energy transfer into the C=O modes, in principle, is an artifact of classical simulations, because these modes are so high in frequency that they are hardly populated at room temperature. In reality, the observed redshift of the C=O modes is not due to population of these modes themselves, but rather due to population of modes that are lower in frequency and couple to the C=O reporter modes (Eq. (4.4)). However, since energy transfer into the C=O modes and the transient redshift are caused by the same anharmonic couplings, this process is expected to be a good estimate of the experimental observable.

The results obtained by Stock and coworkers [78] are summarized in Figure 4.4: subfigure (a) shows the original MD simulations in which the site energies were calculated as an average over the entire amino acid sites, resulting in too fast energy transport rates compared to the experiment. Subfigure (b) shows the corresponding results obtained from the modified MD simulations taking into account the energies of the local C=O vibrational modes only. Comparing both calculations shows a significantly slower time evolution of the site energies in the case of the modified simulations. The resulting transport rates are about one order of magnitude smaller, which agrees much better with the slow time evolution of the redshift observed in the experiment. Moreover, the transport properties extracted from the C=O energies can also reproduce the experimentally measured temperature dependence.

4.4 Conclusion

In this chapter, the effect of IVR on energy transport in biomolecular chains was revisited. It was shown that, when intrasite IVR is slower than energy propagation along the chain, localized higher-frequency modes pick up energy delayed, thus preventing thermalization of vibrational energy on the time scale of transport. Under these circumstances, probing localized C=O reporter groups – which commonly are more sensitive to just these higher-frequency modes – reveals a thermal diffusivity, which shows biphasic behavior. The initial transport of nonthermalized vibrational energy can be described by a decreased apparent heat diffusion constant. On longer time scales, when vibrational energy has relaxed to an equilibrium Boltzmann distribution, heat transport can be described by the familiar bulk properties. The transition between both regimes occurs on a time scale determined by the rate of intrasite IVR.

Hence, the low value observed for the thermal diffusivity at ultrafast time scales is not an artifact of a poor thermometer. It rather shows that averaging the vibrational energy content over entire amino acid residues oversimplifies the problem because it intrinsically assumes full thermalization of the individual sites at all times. This approach, which is commonly used in MD simulations, leads to the surprising result that all the complexity of IVR is completely hidden in a reduced, effective propagation rate.

This finding finally resolves, why MD simulations of real peptides overestimate the experimentally measured energy transport speed, which was one of the questions raised in Chapter 1. If energy is not thermalized within individual amino acid residues, the temperature-induced redshift of the C=O modes does not correspond to the total energy of a residue site, which turned out to be IVR independent, but rather monitors the contribution of higher-frequency modes, which pick up energy on a much slower time scale governed by IVR. Based on this idea, modified MD simulations, which calculate the energy content of the C=O modes instead of the total residue energy, lead to an improved agreement with the experimental results [78].

Chapter 5

Experimental methods

This chapter introduces the setups and concepts necessary for studying energy transport in peptides and proteins from an experimental point of view. Since the redistribution of vibrational energy in biomolecules occurs on ultrafast time scales, transient spectroscopy with femtosecond time resolution is necessary for unraveling these processes. The starting point for all experiments, therefore, are ultrashort and intense laser pulses generated by a femtosecond laser source, which is introduced in Section 5.1. For time-resolved spectroscopy experiments these pulses are split into two parts: a pump beam for initiating the dynamics, and a probe beam for subsequently monitoring them. In this thesis, ultrafast absorption spectroscopy in the infrared, and to a smaller extent, also in the visible spectral regime was performed. Both techniques are implemented in separate setups, which are described in detail in Section 5.2 (transient IR spectroscopy) and Section 5.3 (transient visible spectroscopy).

5.1 Femtosecond laser system

The femtosecond laser pulses used for the experiments originate from a commercial laser system (Spectra-Physics Lasers) that is schematically depicted in Figure 5.1. A frequency-doubled, continuous-wave Nd:YVO_4 laser ("*Millennia*") operating at 532 nm is used to pump a Ti:sapphire (i.e., titanium-doped Al_2O_3) oscillator ("*Tsunami*") emitting 80 fs pulses at a repetition rate of 80 MHz, which have a central wavelength around 800 nm and a pulse energy of about 8 nJ.

To increase their energy, the pulses are sent into a regenerative amplifier ("*Spitfire*"), working on the principle of chirped pulse amplification (CPA). First, by applying a large linear chirp, the laser pulses are temporally stretched to decrease their peak intensity to values below the damage threshold of the optical components in the amplifier. Subsequently, the pulses are amplified in a Ti:sapphire resonator, pumped by a frequency-doubled pulsed Nd:YLF laser ("*Evolution*") emitting pulses at 527 nm with 1 KHz repetition rate. To control the number of cycles in the amplifier, an intracavity Pockels cell is used as an optical switch for coupling the laser pulses in, and – after several round-trips – out of the amplifier. Finally, the amplified pulses are temporally recompressed, resulting in 800 nm laser pulses with 100 fs time duration and pulse energies of up to 800 μJ, however at a significantly lower repetition rate of 1 KHz, which are used for driving the different ultrafast experiments.

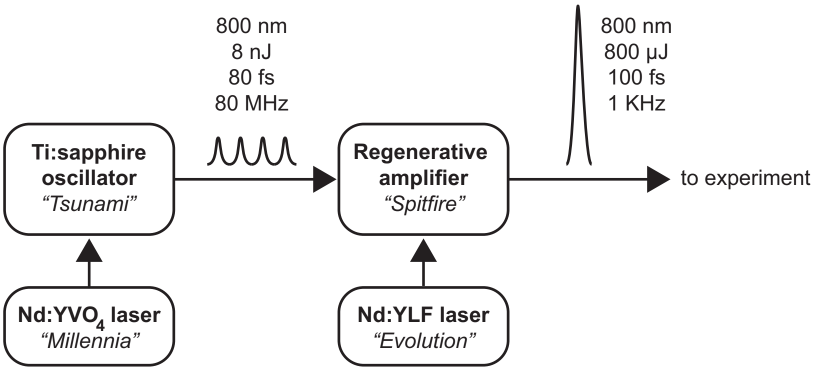

Figure 5.1: Schematic representation of the femtosecond laser system with its different components. A Ti:sapphire oscillator delivers short pulses at a high repetition rate but low pulse energy. In a subsequent regenerative amplification process these pulses are temporally stretched, amplified and then temporally recompressed resulting in laser pulses at a lower repetition rate but with a pulse energy increased by five orders of magnitude. The amplified laser pulses with energies of up to 800 μJ are then used in the different experiments.

5.2 Transient IR spectroscopy setup

The transient IR absorption spectroscopy setup is very flexible and can be used for 1-color IR pump/IR probe, 2-color IR pump/IR probe, Vis pump/IR probe and UV pump/IR probe experiments. A schematic overview of the experimental setup is given in Figure 5.2. It is based on the Ti:sapphire laser system described in the previous section delivering 800 nm pulses with a pulse energy of about 800 μJ. The initial laser beam is split into two parts that can be converted into different frequency regimes and subsequently serve as pump and probe pulses. One fraction of the beam is always used for the generation of tunable mid-infrared probe pulses between 3 and 6 μm in an optical parametric amplifier (OPA). The second part, produces intense pump pulses in different frequency regimes (one at a time), i.e., either mid-IR pump pulses generated in a second OPA, visible pump pulses coming from a noncollinear optical parametric amplifier (NOPA), or UV pulses generated by second harmonic generation (SHG). The optical setups used for the frequency conversion of pump and probe pulses are described in Sections 5.2.1 (OPA) and 5.2.2 (NOPA). Finally, the pump and probe pulses are recombined in the pump-probe setup, which is discussed in Section 5.2.3, where the transient nonlinear response of the sample is measured.

5.2.1 Generation of tunable mid-IR pulses

Two identical, home-built two-stage optical parametric amplifiers, based on parametric amplification in a β-barium borate (BBO) crystal and subsequent difference-frequency generation (DFG) in a silverthiogallate ($AgGaS_2$) crystal [79], are used to generate intense (1-2 μJ) and independently tunable (3-6 μm) mid-IR laser pulses. A schematic representation of the OPA setup can be found in Figure 5.3.

A small fraction of about 1% of the 800 nm beam coming from the Ti:sapphire laser system is focused into a 1 mm thick sapphire window to generate a single-filament white-light continuum (WLC), which is subsequently focused into a 4 mm thick type II BBO

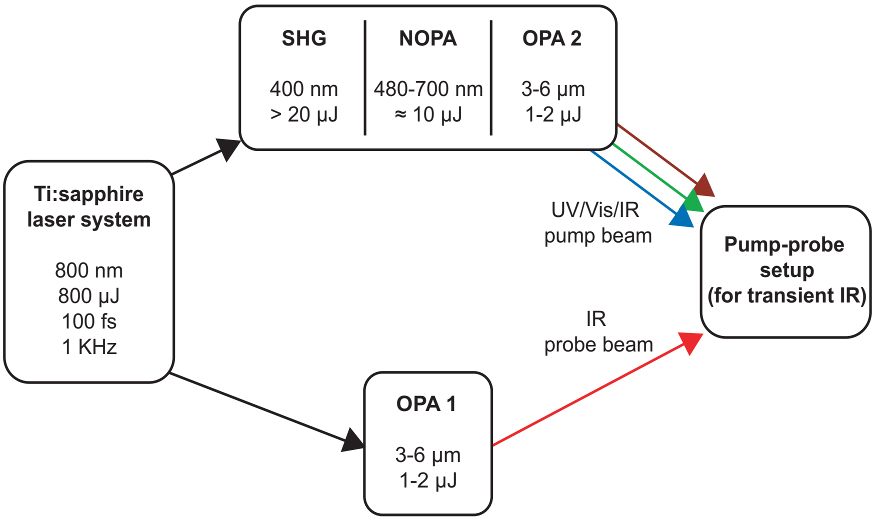

Figure 5.2: Schematic representation of the entire transient IR spectroscopy setup. Femtosecond laser pulses coming from the Ti:sapphire laser system are split into two parts: one part generates mid-IR probe pulses in an optical parametric amplifier (OPA 1, red). The second part, is used to produce intense pump pulses in different frequency regimes (one at a time), i.e., either mid-IR pump pulses generated in a second OPA (OPA 2, dark red), visible pump pulses coming from a noncollinear optical parametric amplifier (NOPA, green), or UV pulses generated by second harmonic generation (SHG, blue). Both pulses are overlapped in the pump-probe setup, where the transient nonlinear response of the sample is measured (see details in Fig. 5.5).

crystal, where it serves as broadband seed for the parametric amplification process.

The first OPA stage is pumped with another fraction of about 10% of the 800 nm beam, which is tightly focused into the BBO crystal. Using a dichroic mirror (DM1, high transmission for white-light seed, high reflection for the 800 nm pump) both beams are collinearly overlapped in the BBO crystal, their temporal overlap is adjusted with delay 1.

The near-IR signal and idler pulses created in the first OPA stage are separated by a second dichroic mirror (DM2, high transmission for idler, high reflection for signal) which removes the idler beam, whereas the remaining signal beam is delayed (delay 2) and focused back into the BBO crystal, seeding the second OPA stage. This second pass is pumped with the remaining 90% of the initial 800 nm beam, which is again coupled into the crystal using a dichroic mirror DM1, yielding intense near-IR signal and idler pulses with energies around 20 to 30 μJ each.

Finally, mid-IR pulses are generated by difference-frequency mixing between the near-IR signal and idler pulses in a 1.5 mm thick type I $AgGaS_2$ crystal. For this second frequency conversion step signal and idler beams are separated by means of another dichroic mirror DM2, which again reflects the signal beam while the idler beam passes, and then focused and collinearly recombined in the crystal. The idler beam is sent over a variable delay line (delay S/I) so that the temporal overlap can be adjusted. The generated MIR pulses are tunable between 3 and 6 μm and have pulse energies between 1 and 2 μJ.

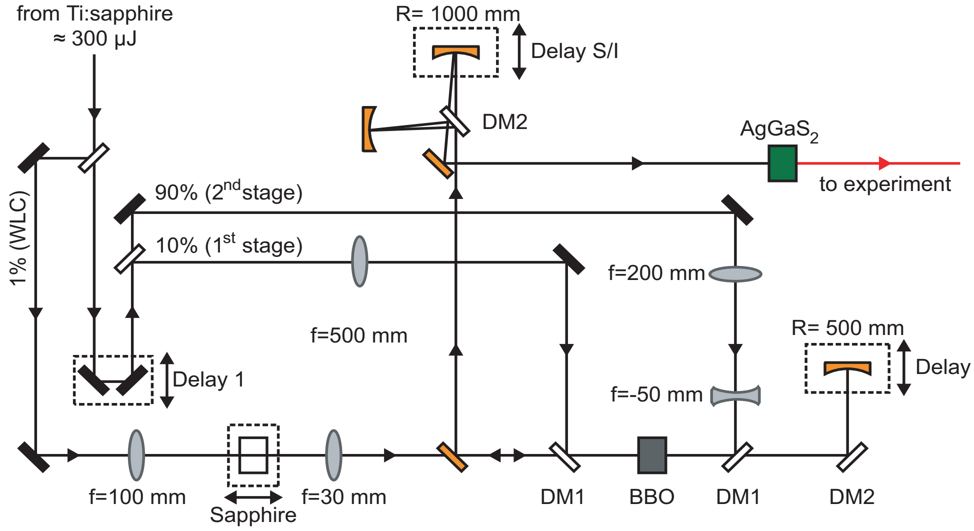

Figure 5.3: Schematic representation of the setup used for the generation of femtosecond tunable mid-IR laser pulses. The two-stage OPA is based on parametric amplification in a BBO crystal and subsequent difference-frequency generation in AgGaS$_2$. (Figure adapted from Ref. [79]).

5.2.2 Generation of tunable Vis pulses

Intense and tunable visible pump pulses are generated in a two-stage blue-pumped noncollinear optical parametric amplifier, which is described in detail in Refs. [80, 81]. A schematic representation of the used setup is given in Figure 5.4.

The NOPA is pumped with a fraction of about 300 μJ of the Ti:sapphire laser system output. The incoming laser beam is slightly collimated by a telescope, which has the same effect as a lens with large focal length, however without introducing a comparably long optical path.

A small fraction of about 4% of the incoming 800 nm beam is focused into a 3 mm thick sapphire window to generate a single-filament white-light continuum (WLC), which is subsequently focused into the first 2 mm thick type I BBO crystal, where it serves as broadband seed for the parametric amplification process.

The main fraction of the fundamental laser beam is frequency-doubled in a 1 mm thick BBO crystal, yielding 400 nm pulses, which are used for subsequently pumping the two passes of the NOPA. To overlap the blue pump light with the respective seed beams in a noncollinear manner, its beam path is located below the plane that contains all the other beams and optics.

20% of the generated blue pump light are focused into the first BBO crystal, where they are recombined with the white-light seed coming from above, the temporal overlap is adjusted with delay 1. The resulting tunable visible output has pulse energies of some 100 nJ.

To further amplify the tunable visible light generated the first stage it is imaged into a second 2 mm thick type I BBO crystal, which is pumped with the remaining 80% of the 400 nm beam. This second NOPA stage finally yields femtosecond visible laser pulses, which are tunable between and 480 and 700 nm and have energies around 10 μJ.

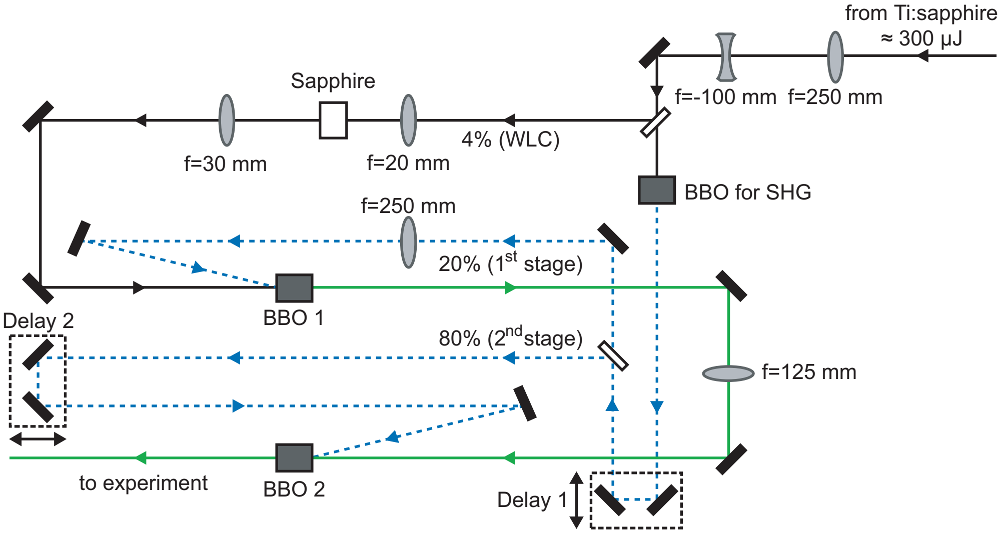

Figure 5.4: Schematic representation of the blue-pumped two-stage NOPA used for the generation of femtosecond tunable visible laser pulses. In reality, the beam path of the frequency-doubled pump light is located below the plane that contains all the other beams and optics (indicated as blue dashed lines).

5.2.3 Pump-probe setup

Figure 5.5 shows the transient IR pump-probe setup, in which the pump and probe pulses are temporally delayed with respect to each other, and subsequently focused and spatially overlapped on the sample, so that its third order nonlinear response can be recorded as a function of delay time.

The IR beam coming from OPA 1 is directed through a long wave pass filter (LWP, transmission for λ>2.5 μm) removing residual contributions from the signal and idler beams. The filtered IR light then passes a wedged BaF_2 window resulting in two spatially separated reflections that serve as weak IR probe and IR reference beams. Passing a 2:3 telescope, which initially increases the beam diameter, finally results in a reduction of the spot size when focused. The IR probe and reference beams are focused on the sample by a 30° off-axis parabolic mirror, resulting in focal beam diameters of ≈ 140 μm. Pump pulses are focused into the sample in spatial overlap with the IR probe pulses, whereas the IR reference beam, which is focused about 1 mm apart, passes through a nonexcited volume of the sample. Behind the sample the IR probe and reference beams are recollimated by a second parabolic mirror before being frequency-dispersed in a grating spectrometer and focused on a double-array HgCdTe detector (2 x 32 pixel, InfraRed Associates, Inc.), where complete IR spectra are recorded simultaneously. The obtained IR absorption spectra have a spectral resolution of $\approx$4 cm^{-1} and a total spectral width of $\approx$120 cm^{-1} (at a probe wavelength of 6 μm).

The main part of the IR light from OPA 1 is transmitted by the wedged window and can be used as intense IR pump beam for 1-color IR pump/IR probe experiments. After sending it over a variable delay line, it is focused on the sample using the same mirrors as for the pump and reference beams.

For 2-color IR pump/IR probe experiments, the IR pump beam from OPA 1 is blocked and instead IR light coming from a second OPA (OPA 2) is coupled into the setup following

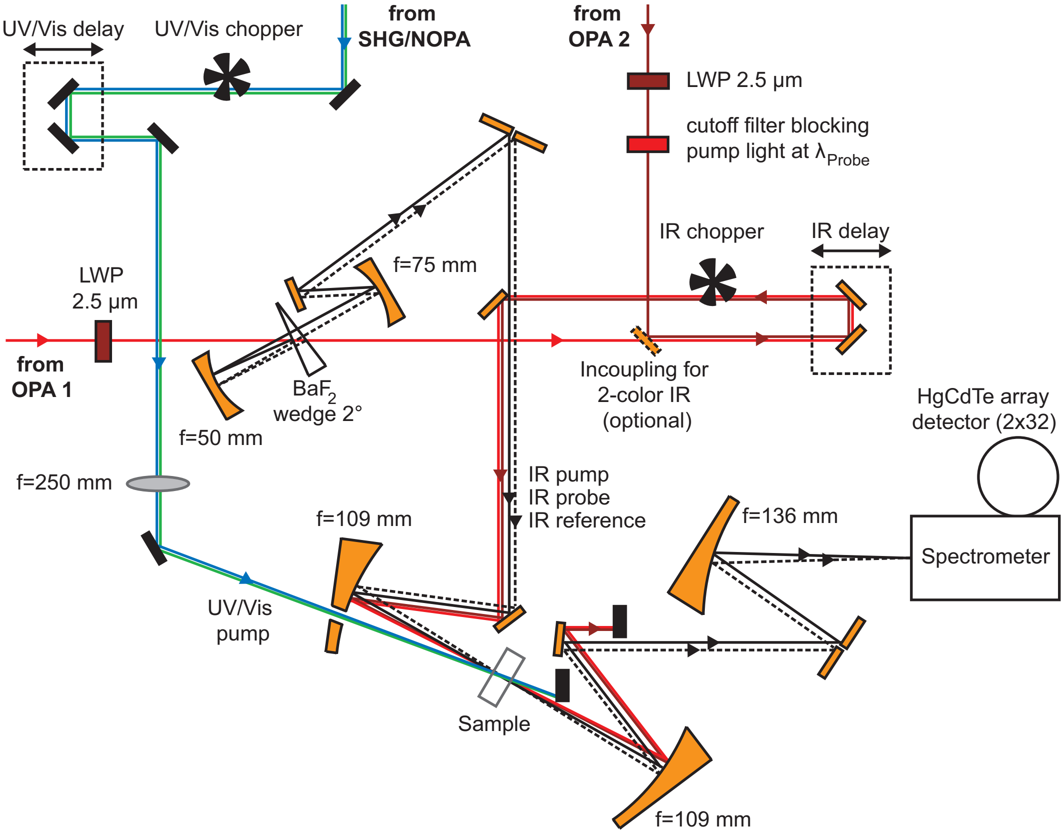

Figure 5.5: Pump-probe setup for transient IR spectroscopy, the different incoming beams are color-coded as in Figs. 5.2, 5.3 and 5.4. IR light coming from OPA 1 (red) passes a wedged BaF_2 window, the two reflections from the front and back side serve as IR probe (black) and IR reference (black dashed) beams, the transmitted part can be used as IR pump beam for 1-color IR pump/IR probe experiments. For 2-color IR pump/IR probe experiments the IR pump beam from OPA 1 is blocked and OPA 2 delivers IR pump light at a different frequency (dark red), which is coupled into the setup along the same beam path as in the 1-color case. All IR beams are focused on the sample by a 30° off-axis parabolic gold mirror and subsequently frequency-dispersed in a spectrometer and imaged on a double-array HgCdTe detector. For UV/Vis pump experiments light from the NOPA (green) or SHG (blue) is coupled in via a separate beamline and overlapped with the IR probe at the sample. Mechanical choppers in the respective pump beams block every other excitation pulse.

the same beam path as in the 1-color case. It turned out that the relative phase between pump and probe beam, even when generated in two separate OPAs, is sufficiently stable so that small fractions of pump light, which are scattered into the spectrometer, can interfere constructively with the probe beam causing unwanted scattering artifacts. Even if the central frequencies of the pump and probe beam differ by more than 500 cm^{-1}, rather small contributions from the tail of the pump spectrum can lead to considerable oscillations on the detected probe spectrum. However, while scattering suppression in the 1-color case requires sophisticated solutions [82], in the 2-color case this problem can be easily solved by inserting an adequate cutoff filter into the pump beam, ensuring that the (scattered) pump light does not have any spectral overlap with the probe region.

For the Vis or UV pump/IR probe experiments the pump beams coming from the NOPA or SHG, respectively, are delayed via a separate variable delay line and focused onto the sample using an adequately anti-reflex coated lens with a focal length of 250 mm.

The physical quantity measured in a pump-probe experiment is the difference in absorption A between a pumped and an unpumped sample recorded as a function of the delay time t:

$$\begin{aligned}\Delta A &= A^{\text{Pump on}} - A^{\text{Pump off}} \\ &= -\log\left(\frac{I^{\text{Pump on}}}{I^{\text{Pump off}}}\right)\end{aligned} \tag{5.1}$$

In practice, such as measurement is accomplished by employing a mechanical chopper, which runs at half the repetition rate of the laser system, so that every other pump pulse is blocked. Thus, the transmitted probe intensity I with and without excitation can be compared for two successive laser shots. The advantage of detecting the absorption change on a shot-to-shot basis is that long-term drift effects of the laser system are eliminated, leading to a significantly enhanced signal-to-noise ratio.

Residual short-term drift effects, like pulse energy fluctuations occurring between successive laser shots, can only be removed on a single-shot basis. Therefore, to further improve the sensitivity of the pump-probe setup, each probe pulse is normalized on the transmission of a reference pulse, which is a replica of the probe pulse originating from the same laser shot.

When measuring the absorbance change on a shot-to-shot basis together with single-shot normalization of the transmitted probe pulses Eq. (5.1) is modified to:

$$\Delta A = -\log\left(\left(\frac{I_{\text{Probe}}}{I_{\text{Ref}}}\right)^{\text{Pump on}} \Bigg/ \left(\frac{I_{\text{Probe}}}{I_{\text{Ref}}}\right)^{\text{Pump off}}\right) \tag{5.2}$$

With the transient IR spectroscopy setup presented in this section absorbance changes down to 10^{-4} (i.e., 10 μOD) can be detected.

5.3 Transient Vis spectroscopy setup

Figure 5.6 shows the transient Vis spectroscopy setup, in which a UV pump beam and a white-light probe beam are generated, temporally delayed with respect to each other, and subsequently focused and spatially overlapped on the sample. The time-resolved absorption change can be detected at chosen wavelengths, which are selected by filtering the white-light probe in front of the detection photodiode.

The setup is based on the Ti:sapphire laser system described in Section 5.1 of which a fraction of about 300 μJ is used to feed the experiment. A small portion of about 5% of the initial 800 nm beam is picked off by a thin glass window and focused into a sapphire window, where an intense and spectrally broad single-filament white-light continuum is generated.

The remaining fraction of the initial 800 nm beam is frequency doubled in a BBO crystal to generate intense UV pump pulses at 400 nm, which are sent over a variable delay line and chopped at half the laser repetition rate. Pump and probe beam are

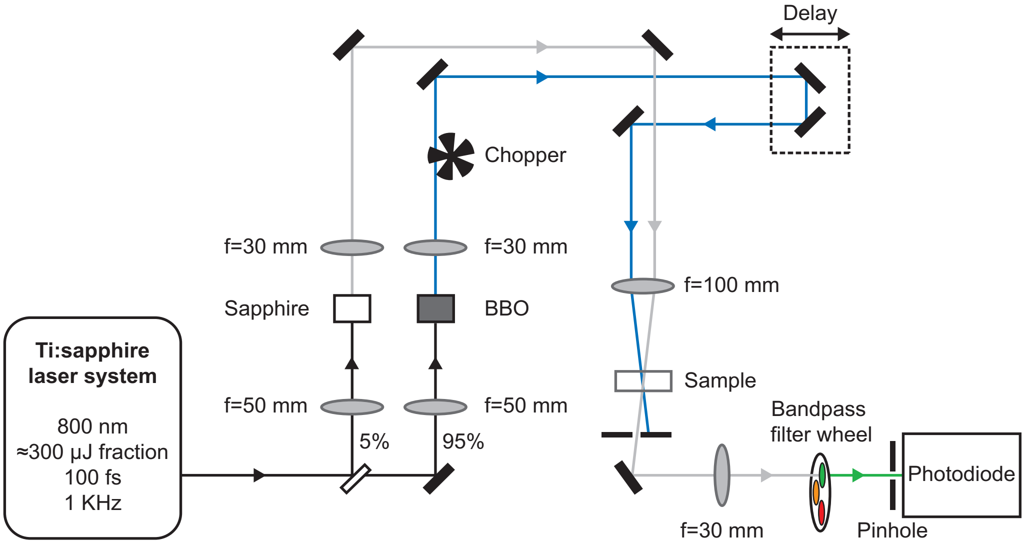

Figure 5.6: Experimental setup for transient Vis spectroscopy. A fraction of the femtosecond 800 nm laser pulses coming from the Ti:sapphire laser system is split into two parts: a small portion of the light is used to generate a white-light probe continuum in a sapphire window (gray). The remaining part is frequency-doubled in a BBO crystal yielding intense UV pump pulses at 400 nm (blue). Both pulses are delayed with respect to each other and focused on the sample. A mechanical chopper blocks every other pump pulse. The detection wavelength is selected by filtering the white-light probe beam in front of the detection photodiode (Figure adapted from Ref. [83]).

focused on the sample using a lens with a focal length of 100 nm. An iris placed behind the sample blocks pump light that is scattered by the sample.

The detection wavelength is chosen by inserting different bandpass filters (FWHM ≈10 nm) behind the sample, thus singling out a narrow spectral probe window from the broad white-light continuum. The transmitted intensity is detected by focusing the filtered white-light probe beam on a fast silicon photodiode. In contrast to the transient IR absorption setup (Section 5.2), where complete spectra can be measured simultaneously by frequency-dispersing and imaging the probe beam on a multi-channel detection array, the transient visible setup works on the principle of single-channel detection. Thus, the time-resolved absorption change can only be measured at one selected probe wavelength at a time.

Chapter 6

Vibrational energy transport after excitation of C−D modes in Leu-d_{10}

The theoretical study presented in Chapter 3 indicates that the vibrational energy transport properties of molecular chains are largely insensitive to the amount of initially deposited energy. In this chapter, decadeuterated leucine (Leu-d_{10}) is introduced as an alternative local heater, which releases a low amount of excess energy by vibrational relaxation of its side-chain carbon-deuterium (C−D) modes. The aim is to study energy transport in a small peptide after low-energy IR excitation, and thus to experimentally address the question whether vibrational energy diffusion really is linear on the given length and time scales.

6.1 Introduction

In the experiments presented by Botan *et al.* [43], energy transport through short peptide helices was studied after deposition of vibrational excess energy by means of an azobenzene chromophore, serving as a local heater that releases a large amount of vibrational energy on an ultrafast time scale. The subsequent energy flow was monitored by using C=O groups in the peptide backbone as local "thermometers". The authors of this paper found that following ultrafast internal conversion of the UV-excited azobenzene moiety, the studied peptide helix is not a particularly good vibrational energy conductor. The thermal diffusivity derived from this experiment (2 $\text{Å}^2\text{ps}^{-1}$) is significantly lower than values known for bulk materials (10-20 $\text{Å}^2\text{ps}^{-1}$ [18, 19, 53, 54]). Furthermore, as discussed before, accompanying MD simulations could only qualitatively reproduce the experimental observations, but also overestimated the measured heat diffusion constant by a factor of five.

In a follow-up paper, Backus *et al.* [51] studied the dependence of the vibrational energy transport properties on the amount of excess energy that is initially deposited. They compared the high-energy (UV) excitation result to that after excitation of a single C=O oscillator in the peptide backbone with low-energy (IR) photons and observed that vibrational energy transport was at least four times more efficient in the latter case (thermal diffusivity $\gtrsim$8 $\text{Å}^2\text{ps}^{-1}$). Since this result agreed much better with the findings for bulk materials and also with the accompanying MD simulations, the authors concluded that the IR experiment was the general case of vibrational energy transport in peptides, whereas the UV experiment represented the exception where energy gets trapped because it is deposited in too high amounts.

The simulations and theoretical considerations presented in Chapters 3 and 4 of this thesis, however, alter the view on the experimental observations and suggest a different interpretation. First of all, the MD simulations of the toy model indicate that no difference between high- and low-energy excitation should be observed. Even time-propagating vibrational energy transport along a molecular chain in a fully quantum-mechanical simulation, which should be able to reproduce possible changes of the thermal properties with temperature, did not show any significant effects. Second, it was understood that on the given ultrashort length and time scales, IVR rather than the actual transport along the chain is the rate-limiting step in vibrational energy transport and significantly slows down the observed propagation speed. Hence, for the thermal diffusivity measured under such experimental conditions, values much lower than for bulk materials should be expected.

These new findings hint at the IR experiment by Backus *et al.* [51] being the special case of vibrational energy diffusion in peptides, in which additional pathways might accelerate the overall energy transport. The study presented in Ref. [51] contains two potential caveats that come along with the use of C=O vibrations as pumping and probing modes at the same time. First, due to the inherent spectral overlap, the probe signals at early times up to about 5 ps are dominated by excitation and relaxation of the directly pumped C=O oscillator and, therefore, cannot be evaluated. As a result, no upper limit for the thermal diffusivity could be given. Second, the possibility of resonant energy transfer directly along the C=O oscillators could act as an alternative route of vibrational energy transport that bypasses energy flow along the peptide backbone, and thus increases the thermal diffusivity measured after C=O pumping.

Motivated by these insights, this chapter presents a repetition of the low-energy excitation experiment with an alternative local heating source that can be pumped with IR photons. Ideally, the pumped mode should be nonresonant with the fundamentals of the C=O spectator modes used as local thermometers, as well as with any of their overtones to also avoid complications with potential Fermi resonances. A promising candidate fulfilling this criterion are C−D vibrations of deuterated amino acid side chains, which occur around 2000-2250 cm^{-1} [84–87]. The ratio between $\nu_{\text{C-D}}$ and $\nu_{\text{C=O}}$ of about 1.3 to 1.4 is close to optimal for avoiding direct, as well as Fermi resonances. Having in mind to incorporate these C−D modes as local heat source into biomolecules, a further important feature is that their absorption falls into the so-called “transparent window” between 1800 and 2600 cm^{-1}, in which protein vibrational spectra are free from any other absorption bands [88–91]. Thus, having no spectral overlap with other vibrations, the C−D absorption has a pronounced local-mode character and corresponds to specific bond vibrations [88], which is an important prerequisite for the local deposition of vibrational energy. The challenge of working with C−D vibrations is their relatively weak transition dipole, however, it has been shown recently by Rubtsov and coworkers [34] that the combined absorbance of the 10 C−D groups of Leu-d_{10} together, all of which can be covered simultaneously with the bandwidth of the experimentally available femtosecond IR pulses, is reasonably large (total effective extinction coefficient $\approx$200 $\text{M}^{-1}\text{cm}^{-1}$). Hence, incorporation of a Leu-d_{10} residue into a peptide sequence should provide a feasible local heater for initiating vibrational energy transport after excitation with IR photons.

6.2 Materials and methods

6.2.1 Laser setup

The spectroscopic experiments presented in this chapter were carried out with the transient IR spectroscopy setup described in Section 5.2. In detail, the experimental conditions were the following. For 2-color IR pump/IR probe experiments independently tunable infrared pulses were generated in two separate OPAs. One OPA was set to a center frequency of 2180 cm^{-1} delivering pump pulses with an energy of about 2 μJ and a bandwidth of 200 cm^{-1} to excite all 10 C−D vibrations of the leucine heater simultaneously. To monitor the response of the C=O reporter groups placed at various distances from the heat source, probe pulses with a bandwidth of 200 cm^{-1} and a center frequency of 1680 cm^{-1} were generated in a second OPA. Scattering between both spectral regions was suppressed by inserting a cutoff filter into the pump beam, blocking all contributions below a frequency of $\approx$1940 cm^{-1}. For 1-color IR pump/IR probe experiments in the C−D region, only one OPA tuned to a center frequency of $\approx$2180 cm^{-1} was used to generate pump and probe pulses at the same time. An overall instrumental response time of 300 fs was determined from a cross-correlation measurement in a germanium plate. All laser beams were polarized parallel.

6.2.2 Peptide helix

The two terminally protected, heptameric peptides used in this study are Z-Aib-Leu**-Aib-Ala*-(Aib)$_3$-OMe (peptide **1**) and Z-Aib-Leu**-(Aib)$_3$-Ala*-Aib-OMe (peptide **2**), where Aib stands for α-aminoisobutyric acid, one asterisk (*) indicates a ^{13}C=O label and two asterisks (**) decadeuteration. An overview of the sequences and their structure is given in Table 6.1 and Figure 6.1.

These particular amino acid sequences were chosen according to the following considerations: Botan *et al.* [43] and Backus *et al.* [51] suggested octameric 3_{10}-helices based on α-aminoisobutyric acid (Aib) as structural motifs for studying energy transport. The advantage of the 3_{10}-conformation is that very stable helices are formed even for relatively short sequences of approximately eight amino acids [45], whereas the more well-known α-helix needs on the order of 20 amino acids to become stable [46].

The intention of this experiment was to incorporate a decadeuterated leucine as a local heater into a similar Aib-based 3_{10}-helical peptide. However, addition of a Leu-d_{10} residue to the original octameric sequence would have led to a nonameric peptide, which is close to the limit for a sufficient solubility, particularly in chloroform solution. Furthermore, the coexistence of 3_{10}- and α-helices is very likely for Aib-rich peptides of that size [44, 92, 93]. Therefore, a shorter sequence of seven amino acid residues was chosen to maintain the pure 3_{10}-helical structure.

Whereas the original azobenzene heater was attached at the N-terminus of the peptide helix, a leucine residue at this position should be avoided because, in this case, the resulting N-terminal -Leu-Aib- dipeptide could fold in either a nonhelical type-II β-turn or a helical type-III β-turn [44, 93].

To measure the local temperature at various distances from the heater as a function of time, ^{13}C=O isotope labels were placed at different positions in the helix. As proposed in Refs. [43, 51] these labels were obtained by incorporating ^{13}C-L-Ala, since this amino acid is readily available commercially and does not destabilize the 3_{10}-helix significantly.

Table 6.1: Terminally protected, heptameric peptides used for the energy transport study. One asterisk (*) indicates a ^{13}C=O label, two asterisks (**) stand for decadeuteration, Z is benzyloxycarbonyl, Aib is α-aminoisobutyric acid, and OMe is methoxy.

Notation	Sequence
Peptide **1**	Z-Aib-Leu**-Aib-Ala*-Aib-Aib-Aib-OMe
Peptide **2**	Z-Aib-Leu**-Aib-Aib-Aib-Ala*-Aib-OMe

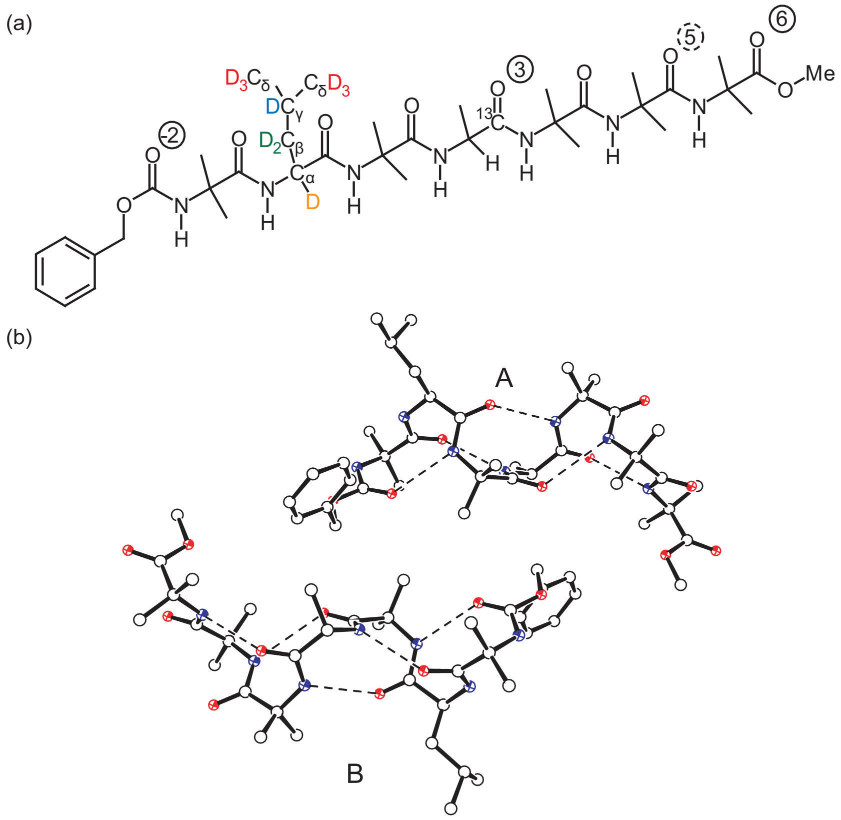

Figure 6.1: (a) Chemical structure of the heptapeptide, here exemplified for peptide **1**. The encircled labels indicate the positions of the different C=O vibrators, which are used as local thermometers, relative to the position of the Leu-d_{10} heater. In peptide **1** the ^{13}C-labeled Ala is situated at site #3 (as shown here); in peptide **2**, the label is placed at site #5. The deuterated sites on the C_α, C_β, C_γ and C_δ side-chain atoms are marked in red, blue, green and orange, respectively. (b) X-ray diffraction structures of the two independent peptide molecules (**A** and **B**) of peptide **1** in the asymmetric unit. H and D atoms have been omitted for clarity. Intramolecular H-bonds are indicated by dashed lines.

Peptide synthesis was performed in solution by activating the carboxyl function with 1-(3-dimethylamino)propyl-3-ethyl-carbodiimide and 7-aza-1-hydroxy-1,2,3-benzotriazole [94]. The peptides were dissolved in chloroform at a concentration of ≈10 mM. The sample was kept between 2-mm-thick CaF_2 windows separated by a 300 μm spacer. If not indicated otherwise, all measurements were carried out at room temperature

6.3 Results

6.3.1 3D-Structural characterization[†]

X-Ray diffraction, FTIR absorption, ^{1}H NMR, and CD techniques were used to examine the preferred conformations of the N$^\alpha$-acylated heptapeptide esters **1** and **2**. Only for peptide **1** a single crystal suitable for an X-ray diffraction analysis could be obtained. Interestingly, there are two independent peptide molecules in the asymmetric unit of **1** (Fig. 6.1b). Both are regular 3_{10}-helices, each stabilized by five intramolecular $i \leftarrow i+3$ C=O...H−N H-bonds. The main difference between them is found in their helical screw sense: one molecule (**A**) is right-handed, whereas the other (**B**) is left-handed (in other words, the two molecules are diastereomers). This is a rather uncommon but not unique observation in peptide crystallography (see also [43] and [96]). What is unique, is that this peptide sequence is characterized by the occurrence of as many as two chiral L-residues, not by one, as found in all previously observed diastereomeric pairs.

The FTIR absorption spectra recorded in the conformationally informative N−H stretching region of peptides **1** and **2** in the structure-supporting solvent chloroform are similar, showing a weak band at about 3425 cm^{-1} (free NH groups) and a very strong band in the 3320-3330 cm^{-1} region (hydrogen-bonded NH groups) [45]. The observed hydrogen bonding can be assigned to the intramolecular type because the spectra do not significantly change upon variation of the peptide concentration between 1.0 and 0.1 mM. The ratio of the integrated intensity of the band of hydrogen-bonded NH groups to that of free NH groups is remarkably high for both peptides **1** and **2**, suggesting the onset of rather stable helical structures. In addition, for peptide **1**, this ratio is close to that previously reported for the 3_{10}-helical -(Aib)$_7$- homopeptide [45] and is slightly higher than that of peptide **2**. The latter finding is indicative of a marginal destabilization induced in the helix by the L-Ala residue when inserted in the penultimate position of the peptide chain, as compared to a central position.

The results of the two ^{1}H NMR titrations in deuterochloroform solution upon addition of the hydrogen bonding acceptor dimethylsulfoxide (DMSO) clearly show that two NH protons for each heptapeptide are exposed to the solvent, whereas the remaining five NH protons are solvent protected by hydrogen bonding. One of these protons (that at the highest field) is easily assigned to the N-terminal Aib proton by virtue of its urethane character [45] and multiplicity (singlet). The second solvent-exposed NH proton can be attributed to the Leu-d_{10} at position 2 in the peptide chain on the basis of a number of conformational studies published on Aib-rich, medium-sized, peptides [43–45, 92]. These overall ^{1}H NMR properties are typical for peptides folded in a 3_{10}-helical structure [45].

The far-UV CD spectra recorded for the two heptapeptides in 2,2,2-trifluoroethanol, also a structure-supporting solvent, exhibit two negative Cotton effects (222-230 nm, weak; and 202-203 nm, very strong) and the ratios of their intensities are in the range expected for peptides largely adopting the 3_{10}-helical structure [97].

From this extensive conformational analysis, one can safely conclude that both heptapeptides **1** and **2** are 3_{10}-helical, although not to the same extent, under structurally favorable experimental conditions.

[†] The synthesis and characterization of the peptides were contributed by Alessandro Moretto, Marco Crisma and Claudio Toniolo from the University of Padova, Italy, and are gratefully acknowledged. The detailed analysis data can be found in Ref. [95] and the corresponding Supporting Information.

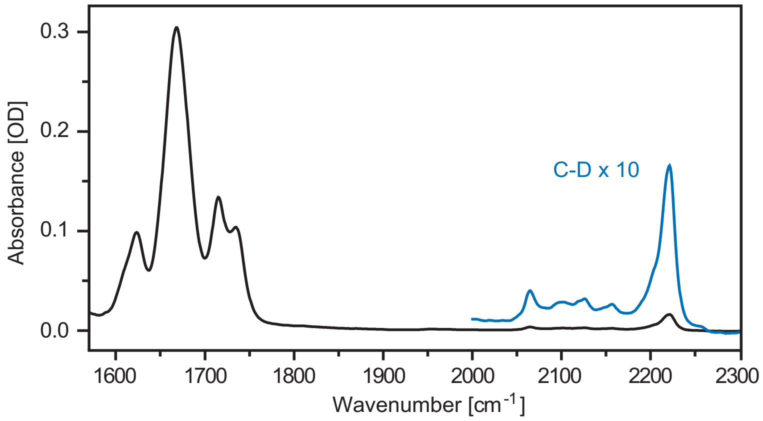

Figure 6.2: Absorption spectrum of peptide **1** in the spectral region of the C=O and the C−D stretching vibrations. For better visibility, the C−D bands are scaled up by a factor of 10 (blue). The four C=O bands at 1620, 1665, 1715, and 1734 cm^{-1} belong to the isotope labeled ^{13}C=O, the main band consisting of all five equivalent carbonyl groups, the N-terminal urethane moiety and the C-terminal ester group, respectively. The five C−D bands appearing at 2065, 2101, 2126, 2157 and 2221 cm^{-1} can be assigned to $C_\delta D_3$(ss), $C_\beta D_2$(ss), $C_\gamma D$, $C_\beta D_2$(as) and $C_\delta D_3$(as), respectively. For further explanations, see text.

6.3.2 Steady state spectroscopy

Steady state infrared absorption spectra with a spectral resolution of 1 cm^{-1} were recorded with a commercial Fourier transform infrared (FTIR) spectrometer (BioRad FTS 175C) equipped with a highly sensitive liquid-nitrogen cooled HgCdTe detector. Figure 6.2 shows the IR absorption spectrum of the peptide helix in the spectral region of the C=O and the C−D stretching vibrations (exemplified here for peptide **1**; the spectrum of peptide **2** is almost identical).

The intense band at 1665 cm^{-1} is the so-called amide I “main band” consisting of all equivalent C=O groups in the helix (five in total). The isotope labeled ^{13}C=O band (i.e., C=O #3 in peptide **1**, C=O #5 in peptide **2**) appears redshifted with respect to the main band at about 1620 cm^{-1}. The bands at 1715 cm^{-1} and 1734 cm^{-1} belong to the two chemically different C=O groups in the helix; namely the urethane moiety connected to the N-protecting group (C=O #-2) and the ester group of the C-terminal Aib residue (C=O #6) [43,51,52].

The side chain of Leu-d_{10} consists of two $C_\delta D_3$, one $C_\gamma D$, one $C_\beta D_2$, and one $C_\alpha D$ moiety, as indicated in Figure 6.1a. Their absorption bands appear in the region around 2200 cm^{-1} and can be assigned as follows [34]: the two $C_\delta D_3$ moieties give rise to the strongest transitions in the spectrum, which are the bands at 2065 cm^{-1} and 2221 cm^{-1} belonging to the symmetric and antisymmetric stretching vibrations, respectively. The $C_\gamma D$ moiety can be assigned to the central peak of the Leu-d_{10} spectrum, appearing at 2126 cm^{-1}. The $C_\beta D_2$ group contributes the remaining two transitions, which are the symmetric and asymmetric stretching vibrations at 2101 cm^{-1} and 2157 cm^{-1}, respectively. The $C_\alpha D$ group is expected to have a very small transition dipole, which is why it is usually not attempted to assign a special peak of the leucine C−D spectrum to its stretching vibration.

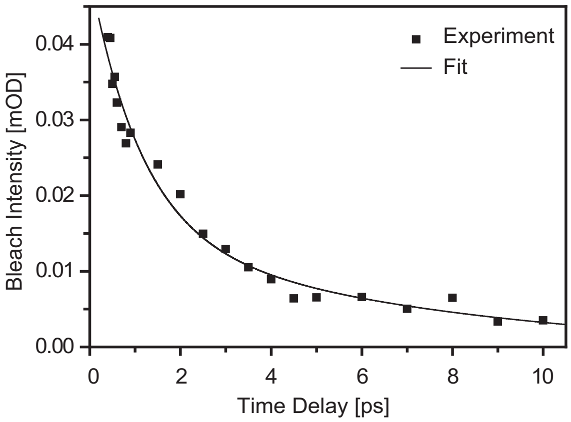

Figure 6.3: Time dependence of the pump-induced bleach measured for the strongest C−D mode of Leu-d_{10} in the peptide helix; a biexponential fit reveals a lifetime of ≈1.1 ps.

6.3.3 Time-resolved spectroscopy

The rate at which energy is released from the heater into the peptide chain is determined by the decay of the initially pumped state. Therefore, in a first set of experiments, the lifetime of the C−D modes of Leu-d_{10} in the peptide helix was assessed in a 1-color IR pump/IR probe measurement at a wavelength of ≈2200 cm^{-1}. Upon pumping all C−D modes simultaneously, their ground states are depleted giving rise to distinct bleach features. Due to the absence of a clear excited state absorption, the lifetime was estimated from the bleach recovery of the strongest C−D mode at 2221 cm^{-1}. The measured bleach intensity as a function of time is displayed in Figure 6.3, a biexponential fit through the obtained data reveals a lifetime of ≈1.1 ps. This number agrees very well with a result published for the corresponding C−D mode in free Leu-d_{10}-Boc dissolved in chloroform, which is T_1=1.3 ps [34].

The time-resolved 2-color IR pump/IR probe spectra from the C=O stretching region are displayed in Figure 6.4, a linear baseline determined from the edges of the spectral window was subtracted from all spectra. Upon excitation of the Leu-d_{10} C−D vibrations, all C=O modes exhibit redshifts, which are due to anharmonic coupling of the spectator modes to thermally excited lower-frequency modes [47]. Since the resulting (negative) bleach signal is, in general, narrower than the anharmonically shifted (positive) hot band, the former was used as a measure of the amount of vibrational energy in the vicinity of the probe. As expected, the main band at 1665 cm^{-1} shows the strongest response. This is because it averages over the five nonlabeled C=O oscillators in the helix, among which are the two direct neighbors of the vibrationally excited Leu-d_{10}; that is, sites #-1 and #1. Comparing the amplitudes of the bleach signals at 1620 cm^{-1}, belonging to the isotope labels at site #3 (peptide **1**, Fig. 6.4, left) and site #5 (peptide **2**, Fig. 6.4, right), it immediately becomes clear that more vibrational energy reaches the closer site #3. Interestingly, the response of site #-2 is more than twice as strong as that of site #3, although its distance to the heater is almost the same (5 vs. 7 chemical bonds; see Fig. 6.1a). This is due to a boundary effect, which pools vibrational energy at the terminal site of the chain. The same effect, albeit less pronounced, can be observed for the C-terminal site #6.

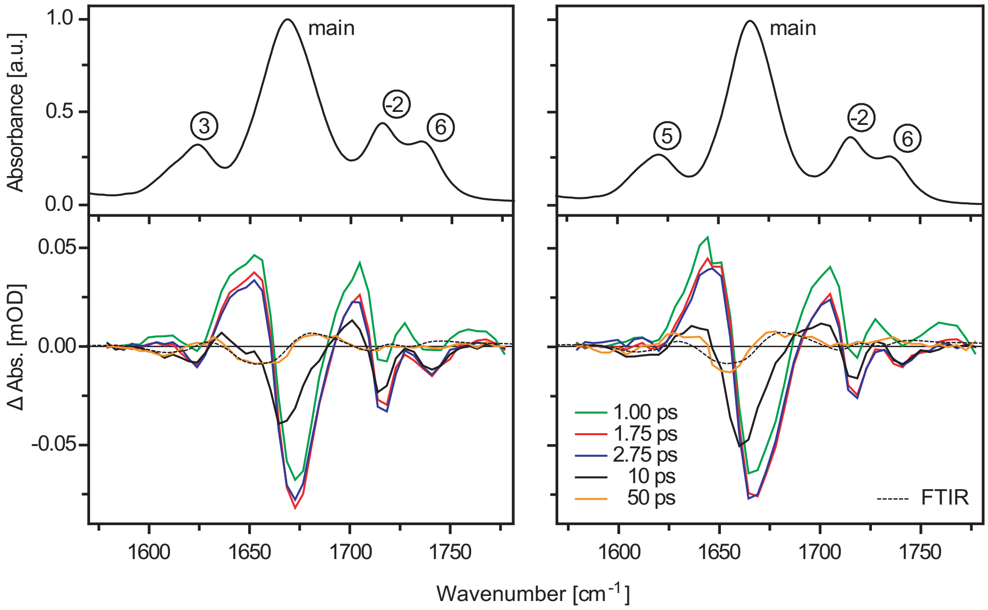

Figure 6.4: Transient spectra in the C=O stretching region for peptide **1** (left column) and peptide **2** (right column) recorded at various delay times (green, 1.00 ps; red, 1.75 ps; blue, 2.75 ps; black, 10 ps; orange, 50 ps) after pumping of the leucine C−D vibrations around 2200 cm^{-1}. For comparison, the stationary absorption spectra of the respective peptides are plotted above. The labels refer to the positions of the C=O groups relative to the heater (see Fig. 6.1a). The black dashed line is a stationary temperature-induced difference spectrum corresponding to a temperature jump of 7.5 mK.

The pump-probe spectra recorded at late delay times (Fig. 6.4, orange lines) resemble a stationary temperature difference spectrum (Fig. 6.4, black dashed lines). The latter was measured for a 10 K temperature increase in an FTIR spectrometer and was down-scaled to match the 50 ps time-resolved result. From the scaling factor, it can be estimated that the bulk solvent is heated up by approximately 7.5 mK. As a secondary effect, this temperature rise leads to an overall weakening of the hydrogen bonds of the helix, resulting in a blueshift of the C=O bands [49, 98].

The kinetics of the main band bleach is shown in Figure 6.5 as a cut through the transient spectra of peptide **1** at 1673 cm^{-1}. A biexponential fit reveals a rise time of 1.1 ps and a decay time of 7.6 ps. The bleach of the main band is dominated by the C=O probes next to the leucine heater; that is, sites #-1 and #1. Assuming that vibrational energy propagation from the Leu-d_{10} side chain to the peptide backbone is not the rate-limiting step, the rise time of the main band is expected to essentially reflect the vibrational lifetime of the C−D modes in Leu-d_{10}. In the 1-color IR pump/IR probe experiment discussed above (Fig. 6.3), the latter was determined to be 1.1 ps, which perfectly supports the given interpretation of the measured data. The ≈7 ps decay component of the main band, on the other hand, is known as the typical cooling time in chloroform [99] and is consistent with all previous energy transport studies in this solvent [43, 51, 52].

The kinetics of sites #-2, #3, and #5 are summarized in Figure 6.6b. One can nicely see the sequential appearance of the bleach maxima, showing that vibrational energy propagates through the molecule. The farther a reporter unit is away from the heater, the later and the less vibrational energy arrives.

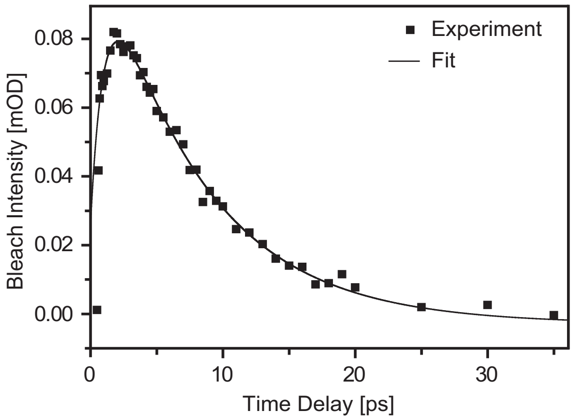

Figure 6.5: Time dependence of the bleach intensity of the main band (recorded for peptide **1**) with opposite sign as in Fig. 6.4. The experimental data can be fitted with a biexponential function with a rise time of 1.1 ps and a decay time of 7.6 ps. Since the main band is dominated by the C=O units closest to the heater its rise time reflects the lifetime of the heated C−D modes.

To model the experimental data, a rate equation scheme similar to the one introduced in Appendix C was devised, which is illustrated in Figure 6.6a. Vibrational energy is initially deposited into the C−D modes of the Leu-d_{10} heater, which decay with a characteristic lifetime T_1. As a result, vibrational energy is transferred to the next neighbors (i.e., sites #-1 and #1) with a rate constant $k_{\mathrm{CD}}{=}T_1^{-1}$. Each peptide unit then can exchange energy with its nearest neighbors with a propagation rate k_{p}. Furthermore, all peptide units lose energy into the solvent at rate k_{s}. To describe the transfer of vibrational energy between the different peptide units a connectivity matrix K as introduced in Eq. (C.5) was used. For the present system of eight site-localized C=O oscillators plus the Leu-d_{10} heater K is a 9×9 matrix, which under the given connectivity of sites (compare Fig. 6.6a; the leucine unit is treated as site $n = 9$) adopts the following form:

$$K = \begin{pmatrix} -k_{\mathrm{s}} - k_{\mathrm{p}} & k_{\mathrm{p}} & 0 & 0 & \cdots & 0 \\ k_{\mathrm{p}} & -k_{\mathrm{s}} - 2k_{\mathrm{p}} - k_{\mathrm{CD}} & k_{\mathrm{p}} & 0 & \cdots & k_{\mathrm{CD}} \\ 0 & k_{\mathrm{p}} & -k_{\mathrm{s}} - 2k_{\mathrm{p}} - k_{\mathrm{CD}} & k_{\mathrm{p}} & \cdots & k_{\mathrm{CD}} \\ 0 & 0 & k_{\mathrm{p}} & -k_{\mathrm{s}} - 2k_{\mathrm{p}} & \cdots & 0 \\ \vdots & \vdots & \vdots & \vdots & \ddots & \vdots \\ 0 & k_{\mathrm{CD}} & k_{\mathrm{CD}} & 0 & \cdots & -k_{\mathrm{s}} - 2k_{\mathrm{CD}} \end{pmatrix} \tag{6.1}$$

In case of energy conservation within the chain the sum over each column of the matrix K is zero. However, in the present case energy is dissipated from the peptide chain into the solvent with a cooling rate k_{s}. Therefore, summing up all elements of one column of K a sink term $-k_{\mathrm{s}}$ remains.

As demonstrated in Appendix C, the solution of the resulting set of coupled differential equations is given by

$$\vec{\epsilon}(t) = Q^{-1}\mathrm{diag}(e^{\lambda_1 t}, e^{\lambda_2 t}, ..., e^{\lambda_n t})Q\vec{\epsilon}(0). \tag{6.2}$$

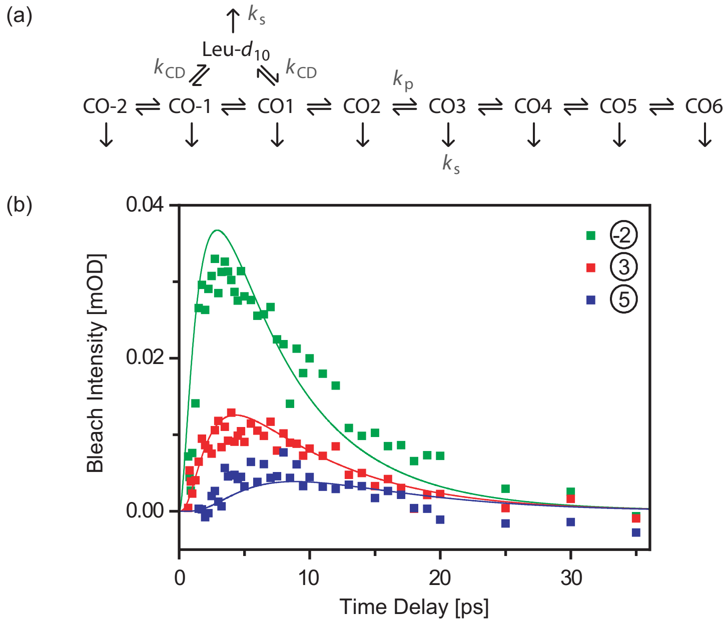

Figure 6.6: (a) Scheme of the rate model used for global fitting of the experimental data. The Leu-d_{10} heater is directly coupled to its next neighbors. The corresponding rate constant is given by the inverse lifetime of the C–D modes; that is k_{CD}=(1.1 ps)$^{-1}$. Cooling of all peptide units into the solvent occurs with a rate constant of k_{s}=(7.6 ps)$^{-1}$; the propagation rate in the helix is k_{p} ≈(2 ps)$^{-1}$. (b) Time dependence of the bleach intensity of sites #-2, #3 (both recorded at peptide **1**), and #5 (recorded at peptide **2**) with opposite signs as in Fig. 6.4. The solid lines represent global fits according to the rate model shown on top.

Since all energy initially is deposited into the heater unit ($n = 9$) the initial condition is:

$$\vec{\epsilon}(0) = \begin{pmatrix} \vdots \\ 0 \\ 1 \end{pmatrix} . \tag{6.3}$$

The rate constants for the energy injection into the chain and the cooling into the solvent can be extracted from the main band fit: k_{CD}=(1.1 ps)$^{-1}$ and k_{s}=(7.6 ps)$^{-1}$, respectively. The remaining free parameter k_{p} then can be deduced from a global fit of the obtained functions $\epsilon_i(t)$ to the measured time traces of sites #-2, #3, and #5. With the obtained propagation rate constant $k_{\mathrm{p}} = (2.0 \pm 0.5)^{-1}$ ps^{-1} the experimental data can be well reproduced (see Fig. 6.6b, solid lines).

6.4 Discussion

The experimental data can be reasonably described by a diffusive model. As discussed in Appendix C, one can think of the rate equation model of Figure 6.6a as a discretized version of a diffusion equation, in which the diffusion constant D is related to the propagation rate k_{p} through $D = k_{\mathrm{p}} \Delta x^2$ (Eq. (C.7)). With the helical translation per residue for a 3_{10}-helix of Δx ≈2 Å [44, 100], a heat diffusion constant of D=(2.0±0.5) Å^{2}ps^{-1} can be calculated, which is in quantitative agreement with the result obtained by Botan *et al.* [43] after UV pumping of a covalently attached azobenzene moiety (2 $\text{Å}^2\text{ps}^{-1}$).

Thus, comparing the IR pumping result presented in this chapter to the UV pumping result of Ref. [43], within signal-to-noise, no excitation energy dependence of the heat diffusion constant is observed. Hence, this study experimentally verifies one of the predictions made in Chapter 3; the energy transport properties of molecular chains are largely insensitive to the amount of initially deposited energy. Even when temperature gradients of many hundreds of Kelvin are generated over length scales of only a few chemical bonds, the linearity of vibrational energy diffusion is maintained.

The value obtained after off-resonant IR pumping of side-chain C−D modes is much lower than that after resonant excitation of backbone C=O groups ($\gtrsim$8 $\text{Å}^2\text{ps}^{-1}$) [51]. This shows that the enhanced propagation rate after resonant IR pumping must be due to coherent energy transfer directly along the C=O oscillators that bypasses vibrational energy flow along the peptide backbone. Suppressing this additional transport pathway, only the backbone chain can contribute to the redistribution of vibrational energy in the peptide, giving rise to the much lower heat diffusion constant of $\approx$2 $\text{Å}^2\text{ps}^{-1}$. This interpretation is also supported by a recent publication by Stock and coworkers [101], who performed nonequilibrium MD simulations of the experimentally studied 3_{10}-helix, showing that resonant excitation of a localized C=O oscillator initiates coherent energy transport along the C=O modes, with an amplitude and speed much higher than for energy transfer via the backbone.

Another prediction from Chapters 3 and 4 that has been confirmed by this experiment is that the apparent heat diffusion constant observed on the given ultrashort length and time scales truly is much lower than in macroscopic experiments (10-20 $\text{Å}^2\text{ps}^{-1}$). This is because IVR rather than the actual transport along the chain is the rate-limiting step for energy redistribution and determines the measured propagation speed. This point is discussed in more detail in Chapter 8.

The rate equation model presented in Figure 6.6a can nicely reproduce the effect of energy pooling at the N-terminal site #-2. The response of site #-2, measured relative to that of site #3, is much larger than what would be expected just from their different distances (5 vs. 7 chemical bonds; see Fig. 6.1a). From the rate equation model, one expects the response of site #-2 to be about 50% larger than the response of site #2, although both are situated at the same distance from the heater. This is the result of a boundary effect for the diffusion along a *finite* one-dimensional chain, which provides additional strong evidence that vibrational energy indeed flows along the peptide backbone, and not just through the solvent. Actually, the bleach of site #-2 should be even more distinct than found in the experiment. The fact that the simulation slightly overestimates its intensity could be due to the N-protecting group (Z-moiety), which is the real boundary of the peptide chain and has been neglected in the rate model.

Finally, a remark on the choice of the solvent for such a 2-color IR pump/IR probe experiment. Pumping the C−D vibrations of deuterated amino acid side chains and probing the amide C=O bands requires a spectrally broad transmission window from 1650 cm^{-1} to 2200 cm^{-1} (alternatively, at least two separate transmission windows around those regions). Solvent absorption is in particular disturbing in the pump region because it can lead to isotropic heating of the sample. This problem can in principle be resolved in a 2-color 2-dimensional IR experiment [34], which can differentiate the pairwise interaction between probed and pumped modes from those with a solvent background. In any case, the transfer of such an experiment especially into aqueous solution will be very difficult because heavy water (D_2O) is only transparent around the C=O vibration but highly absorbing in the C−D region while the contrary is true for normal water (H_2O). Rubtsov *et al.* [34] suggest that similar experiments could be done in D_2O solution on thin samples of ≈25 μm path length, which, however, is more than a factor 10 less than used in this experiment and would consequently decrease the signal size. Furthermore, it must be borne in mind that all C−D modes broaden drastically when hydrated in D_2O, which can be attributed to the influence of the heavy water O−D transitions [34]. Therefore, applying a Leu-d_{10} residue as a local heater in D_2O solution is limited to amino acid positions buried in the hydrophobic core of a protein.

6.5 Conclusion

In this chapter, decadeuterated leucine was introduced as a novel local heater for initiating vibrational energy transport through the peptide backbone. Leu-d_{10} is commercially available and can be easily incorporated into a peptide sequence by standard methods of peptide synthesis. Although the C−D vibrations are relatively weak IR absorbers, the total extinction coefficient of all 10 leucine C−D vibrations together is large enough to deposit a sufficient amount of vibrational energy, whose propagation through the peptide helix can be followed with a reasonable signal-to-nose ratio.

Vibrational energy propagation after IR excitation of the C−D modes can be described as a diffusion-like process. The effect of terminal energy pooling provides further evidence that energy propagates along the molecular chain, and not through the solvent. The measured heat diffusion constant of $\approx 2\ \text{Å}^2\text{ps}^{-1}$ is in agreement with the UV pump study presented by Botan *et al.* [43], confirming the prediction of Chapter 3 that the energy transport properties of biomolecular chains do not depend on how much energy initially is deposited. The fourfold faster energy transport observed by Backus *et al.* [51] can be attributed to a special case of resonant energy transfer directly along the C=O oscillators. In the present experiment, this additional transport pathway is strongly suppressed because the pumped C−D vibrations are nonresonant to the amide I vibrations.

Even the generation of large temperature gradients over very short length scales does not lead to artifacts like energy trapping; the linearity of vibrational energy diffusion has proved to be rather solid. This means that energy transport properties can be studied equally well after the deposition of high amounts of excess energy, which from a practical point of view is advantageous because much larger signals can be observed over longer distances. This opens the possibility to develop new efficient heaters and to extend vibrational energy transport studies to proteins to experimentally address the question whether specific transport pathways indeed exist as they are consistently predicted from MD simulations [8,9,25,27,30]

Chapter 7

Vibrational energy transport after plasmonic heating of gold nanoparticles

In this chapter, another novel heating mechanism for studying vibrational energy transport in biomolecules is introduced. The idea is to locally release a high amount of vibrational excess energy by using plasmonically heated noble metal nanoparticles, which, due to their large optical cross section and low quantum yield, are extremely efficient photothermal converters [102]. As structural motif for this experiment, again, short 3_{10}-helical peptides are chosen and covalently linked to spherical gold nanoparticles covering their entire surface. In contrast to the previous chapter, where energy transport was studied along individual helical chains, the peptides in this experiment are arranged in an ordered three-dimensional structure around the heat source. The geometry and packing efficiency of this capping layer influence the dissipation of vibrational energy into the solvent.

7.1 Introduction

The Leu-d_{10} residue presented in the previous chapter, due to its intrinsic limitations and the low absorbance of the pumped modes, is a very academic example of a local heater. In contrast, local heat generation with noble metal nanoparticles is of huge practical interest and has found numerous therapeutic applications in the life sciences [103]. For example, in hyperthermal therapy of cancer, plasmonically heated gold nanoparticles are used for the localized deposition of heat into human cancer tissue resulting in irreversible thermal cellular destruction [104–107]. Furthermore, plasmonic heating offers a possibility to optically activate drug delivery from nanoparticles; illumination of nanoparticles at their plasmon resonance frequency causes the particles to transfer heat to their local environment triggering the release of payload molecules attached to the surface [108–112].

Many of these practical applications rely on the optical excitation of a surface plasmon, which is an electronic effect causing metallic nanoparticles to strongly absorb and scatter electromagnetic radiation at wavelengths much larger than their own size [103]. The reason for this intense light-matter interaction is a collective response of the free metal electrons to an incoming light field; its oscillating electric field causes the conduction electrons at the metal surface to oscillate coherently [113], an effect, which is referred to as surface plasmon resonance. The frequency and bandwidth of the plasmon resonance depend on the shape and size of the nanoparticles as well as on material properties, such as the density and the effective mass of the conduction electrons [113]. For gold nanospheres, the plasmon resonance frequency, at which light can efficiently couple to the collective electronic excitation, is around 520 nm [114], giving rise to a pronounced optical absorption. The absorbed light excites electrons that relax via electron-electron scattering to a nonequilibrium energy distribution. Subsequently, this hot electron gas scatters with the lattice phonons, which transfer the excess energy into the surroundings [115, 116], leading to a highly localized increase in temperature that takes place on a picosecond time scale [115–122].

The efficient, localized and ultrafast conversion of light into thermal energy are unique features of metal nanoparticles, making them suitable as local heaters for energy transport studies. Comparable to the azobenzene heater introduced by Botan *et al.* [43], gold nanoparticles release a high amount of excess energy subsequent to excitation at UV/Vis frequencies. As discussed in Chapter 6, this approach of high-energy excitation is experimentally favorable because the redistribution of large amounts of vibrational energy in biomolecules can be followed over large distances and does not impose potential nonlinear artifacts on the heat diffusion. Beyond that, however, gold nanoparticles are superior to azobenzene chromophores in several respects. First of all, since metal nanoparticles have extinction coefficients much higher than organic chromophores, heating can be achieved with considerably lower excitation energies. At the same time, nanoparticles are not prone to bleach upon photoexcitation so that exchanging degraded sample is not necessary. As a result, experiments can be performed with much smaller sample volumes, which is particularly interesting when working with rare biomolecules. Furthermore, no conformational change (*cis-trans* isomerization) is involved in the excitation step, meaning that no disorder is generated in the attached biomolecules. Finally, whereas azobenzene chromophores often show disturbing vibrational ring modes in the amide I region [123], spherical gold nanoparticles do not have any infrared absorption at all.

Recognizing these advantages, the intention of this chapter is to introduce gold nanoparticles as an alternative local heater for energy transport studies in biomolecules and to explore its properties with nonlinear laser spectroscopy. The aim is to design an experiment, in which vibrational excess energy is locally deposited into the nanoparticle metal core by exciting its plasmon resonance with laser pulses in the visible region. The following energy transport along attached peptide chains is studied with femtosecond infrared spectroscopy, using ^{13}C=O isotope labels at defined distances from the metal surface as local thermometers. In a similar manner, vibrational sum-frequency generation from molecular chains on a laser flash-heated bulk gold surface has been studied by Dlott and coworkers [31, 124]. However, using a suspension of gold particles allows to study the process in a conventional pump-probe geometry, rather than by surface sensitive methods. Furthermore, due to the extremely high surface-to-volume ratio of nanoparticles, a much higher surface coverage than for bulk materials can be achieved, which consequently leads to much higher signals from the applied organic chains.

7.2 Materials and Methods

7.2.1 Laser Setup

In this chapter, femtosecond spectroscopy experiments in the visible and infrared spectral range are presented. The response of the nanoparticle gold core upon pulsed laser excitation was measured in a UV pump/Vis probe experiment using the transient Vis spectroscopy setup presented in Section 5.3. As described above, in this setup one portion of the initial laser beam produces 400 nm pump pulses, the remaining fraction is used to generate a white-light continuum serving as a probe beam. The probe wavelength was chosen by placing a 520 nm band pass filter with 10 nm bandwidth (FWHM) in front of the detection photodiode.

To measure the response of the C=O reporter groups in the attached peptides, a Vis pump/IR probe experiment was performed on the transient IR spectroscopy setup described in Section 5.2. Pump pulses at a center wavelength of 520 nm and a bandwidth of 20 nm, attenuated to approximately 0.5 μJ at the sample, were generated in a blue-pumped two-stage NOPA and excited the gold nanoparticle plasmon resonance. Infrared probe pulses with a center frequency of 1670 cm^{-1} and a bandwidth of 200 cm^{-1} were produced in a white-light-seeded two-stage OPA. An overall instrumental response time of 200 fs was determined from a cross-correlation measurement in a silicon plate. All beams were polarized parallel.

7.2.2 Peptide-capped gold nanoparticles

The spherical gold nanoparticles, synthesized for this experiment, were covalently linked to and completely covered by helical peptides. The design of those nanoparticles and the applied peptide capping layer was guided by the following considerations: very small gold nanoparticles with diameters of about 1-2 nm were chosen for this study because they have a more favorable surface-to-volume (i.e., peptide-to-gold) ratio that allows sufficient IR absorbance from the peptide capping layer to be obtained without the sample becoming opaque in the visible. Also, small nanoparticles are more resistant against laser-induced aggregation.

As structural motifs for the peptide ligands, 3_{10}-helices were chosen, which form exceptionally stable structures, even for short sequences (compare Chapter 6) [45]. Thus, a rigid peptide capping layer was obtained enabling to place ^{13}C=O reporter groups in a fixed geometry over the metal surface. The two capping agents used in this study were the octameric peptides HS-$(\mathrm{CH_2})_2$-O-CO-Aib-Ala*-$(\mathrm{Aib})_6$-OMe (peptide **1**) and HS-$(\mathrm{CH_2})_2$-O-CO-$(\mathrm{Aib})_3$-Ala*-$(\mathrm{Aib})_4$-OMe (peptide **2**), where Aib stands for α-aminoisobutyric acid and an asterisk (*) indicates a ^{13}C=O label. The thiol (-SH) group at the N-terminus was used to attach the peptides to the gold nanoparticles. An overview of the peptide sequences, their chemical structure and the resulting peptide-capped gold nanoparticles is given in Table 7.1 and Figure 7.1.

To measure the local temperature at various distances from the heat source as a function of time, ^{13}C=O isotope labels were placed at different positions in the peptide helix. As already demonstrated in Chapter 6, these labels can be obtained by incorporating ^{13}C-L-Ala, since this amino acid is readily available commercially and does not destabilize the 3_{10}-helix significantly. In addition, a urethane moiety was inserted between the linking group and the actual peptide to obtain an intrinsically spectrally resolved C=O group at

Table 7.1: Octameric peptides used as capping ligands for the gold nanoparticles. An asterisk (*) indicates a ^{13}C=O isotope label, Aib stands for α-aminoisobutyric acid and OMe for methoxy.

Notation	Sequence
Peptide **1**	HS-$(CH_2)_2$-O-CO-Aib-Ala*-Aib-Aib-Aib-Aib-Aib-Aib-OMe
Peptide **2**	HS-$(CH_2)_2$-O-CO-Aib-Aib-Aib-Ala*-Aib-Aib-Aib-Aib-OMe

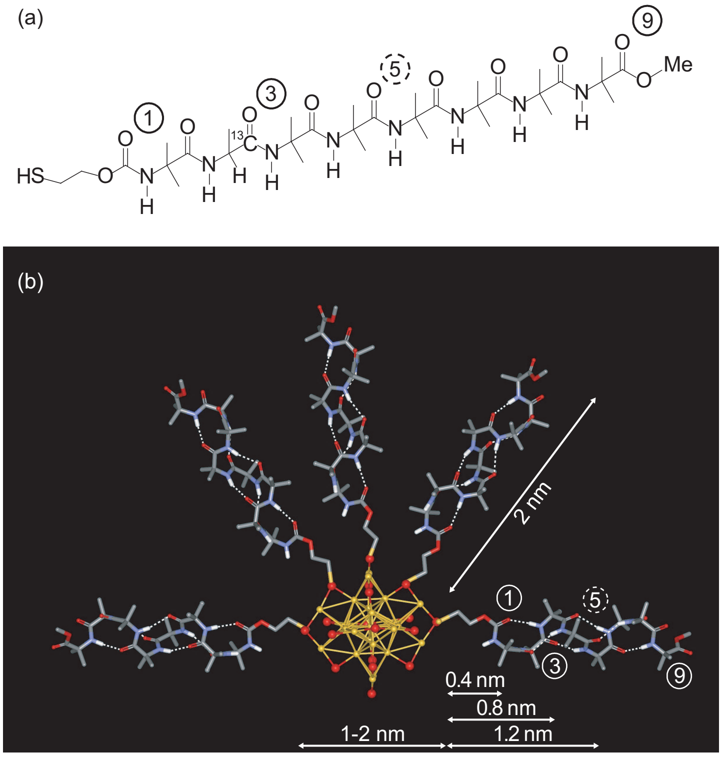

Figure 7.1: (a) Chemical structure of the 3_{10}-helix forming peptide **1**. The N-terminal thiol group is covalently linked to the gold nanoparticle. (b) Cartoon structure of the peptide-capped gold nanoparticles. The encircled labels in both subfigures indicate the positions of the different C=O thermometers in the capping layer relative to the gold core at the N-terminus. In peptide **1**, the ^{13}C=O labeled Ala is situated at site #3 (as shown here); in peptide **2**, the label is placed at site #5.

the beginning of the helical chain.

First, the terminally protected, linear octapeptides **1** and **2** were synthesized step-by-step by solution methods. Subsequently, the gold nanoparticles were prepared following a general procedure described in Ref. [125]: the peptides and chloroauric acid ($HAuCl_4$, 3:1 molar ratio) were combined in a 7:3 methanol/water solvent mixture and allowed to stand for 1 h. Then, 10 equivalents of $NaBH_4$ were added, and the suspension was stirred at room temperature for 5 h. The product was precipitated by adding 2 vol. of Et_2O, pelleted at top speed in a centrifuge, resuspended in 70% Et_2O/EtOH, pelleted again, and dried overnight at room temperature.

For the all spectroscopic measurements presented, the dehumidified peptide-nanoparticle sample was dissolved in acetonitrile-d_3 and vortexed for a few minutes. Filtering the resulting solution through a PTFE membrane with 0.45 μm pore size removed scattering particles. The effective peptide concentration, estimated from an FTIR measurement of the amide I band, was adjusted to approximately 10 mM (i.e., the absolute concentration of gold nanoparticles was accordingly lower). The sample was kept in a CaF_2 cell with an optical path length of 100 μm, including the option to circulate it in a closed cycle. However, since the nanoparticles were sufficiently stable against temperature-induced aggregation, flowing the sample turned out to be redundant. All measurements were carried out at room temperature.

7.3 Results

7.3.1 Nanoparticle Characterization[†]

The terminally protected -$(\mathrm{Aib})_8$- sequence is well-known to be folded in a fully developed 3_{10}-helical structure in chloroform solution [45]. The preferred conformation of the two octapeptides **1** and **2** that were used as capping ligands for the gold nanoparticles were examined. To validate that the 3_{10}-helical structure is maintained in structure-supporting solvents (chloroform and 2,2,2-trifluoroethanol), FTIR absorption, ^{1}H NMR, and CD techniques were applied.

The FTIR absorption spectra in the N$-$H stretching region of the two peptides in $CDCl_3$ solution are similar, showing a weak band at $\approx$3430 cm^{-1} (free N$-$H groups) [45] and a very intense band near 3328 cm^{-1} (hydrogen bonded N$-$H groups). Because a change in peptide concentration (from 1.0 mM to 0.1 mM) does not significantly modify the spectra, most of the observed hydrogen bonding can be safely assigned to the intramolecular type. The ratios of the integrated intensity of the band of hydrogen bonded N$-$H groups to that of free N$-$H groups for the two peptides are in accordance with previously reported results for the 3_{10}-helical -$(\mathrm{Aib})_8$- peptide [45].

The results of the ^{1}H NMR titrations in $CDCl_3$ solution upon addition of the hydrogen bonding acceptor solvent DMSO clearly indicate that two NH protons for each octapeptide are exposed to the solvent, whereas the remaining six NH protons are solvent protected because of intramolecular C=O...H$-$N hydrogen bonding. One of these NH protons (that at highest field) is assigned to the N-terminal N(1)H proton by virtue of its urethane character [45]. In peptide **1**, the second solvent-exposed NH proton is easily attributed to Ala* at position 2 on the basis of its different multiplicity. These ^{1}H NMR properties are those expected for peptides adopting a regular 3_{10}-helical structure [45].

The far-UV CD spectra of peptides **1** and **2** in 2,2,2-trifluoroethanol solution show two negative Cotton effects with positions (205 nm, very strong; 225 nm, weak) and ellipticity ratios ($\theta_{225}/\theta_{205}$=0.25) typical for a right-handed 3_{10}-helix [97].

A transmission electron microscopy (TEM) analysis was employed to determine the average gold nanoparticle core size. Similar to a previous report [127], for the peptide **1**/$HAuCl_4$ 3:1 molar ratio preparations at room temperature, an average gold nanopar-

---

[†] The synthesis and characterization of the gold nanoparticles were contributed by Alessandro Moretto and Claudio Toniolo from the University of Padova, Italy, and are gratefully acknowledged. The detailed analysis data can be found in Ref. [126] and the corresponding Supporting Information.

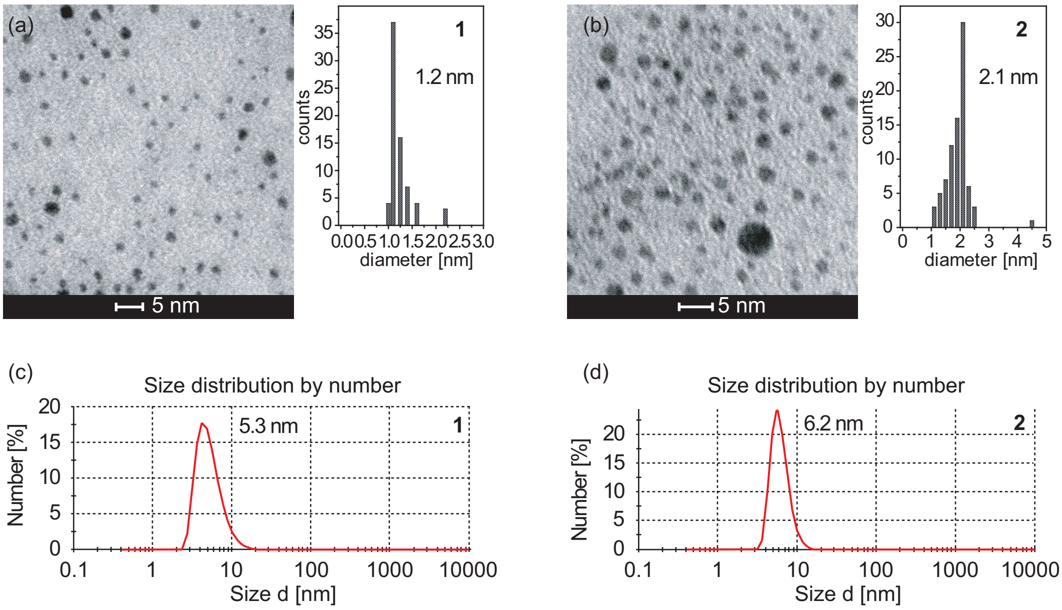

Figure 7.2: Size characterization of the peptide-capped gold nanoparticles: TEM images of the metallic cores of the nanoparticles, the insets show histograms of the corresponding size distribution. The average gold core diameters are 1.2 nm for nanoparticle **1** (a) and 2 nm for nanoparticle **2** (b). Light scattering data obtained for nanoparticles in methanol solution. The obtained total particle diameters, including the capping layer, are 5.3 nm for nanoparticle **1** (c) and 6.2 nm for **2** (d), and match very well the respective core size plus two times the length of the applied peptide ligands, which is $\approx$2 nm.

ticle core size of 1.2 nm (*d*, diameter) was found (Fig. 7.2a). In accordance with the mentioned report, an average gold nanoparticle formula of $Au_{38}Pept_{18}$ is proposed. For the peptide **2**/$HAuCl_4$ 3:1 molar ratio preparations, a bigger gold nanoparticle core size of 2.1 nm (*d*) was observed, which could be due to the fact that the two used peptide ligands have slightly dissimilar structures (Fig. 7.2b). For those nanoparticles an average gold nanoparticle formula of $Au_{225}Pept_{68}$ is proposed [127]. The fact that the different ligands lead to different nanoparticle sizes – although initially unintended – enables to study size-dependent effects of energy transport through differently packed peptide capping layers.

Dynamic light scattering was used to assess the average size of the gold nanoparticles, including the capping layer. The results showed total diameters of 5.3 nm for gold nanoparticle **1** (Fig. 7.2c) and 6.2 nm for **2** (Fig. 7.2d). Based on a similar 3_{10}-helical peptide, the 3D-structure of which was solved by X-ray diffraction [43], a length of $\approx$2 nm can be assumed for both peptide ligands. Adding this value twice to the gold core diameter obtained from the TEM analysis, the experimental values from light scattering are well matched. Even though the light scattering from the gold core and that from the capping layer are different, and the effects of both are not just additive, this qualitative analysis shows that the dimensions of the bulk spherical nanoparticles (gold core with capping ligand molecules) can be modulated rather precisely by an appropriate choice of the peptide ligand.

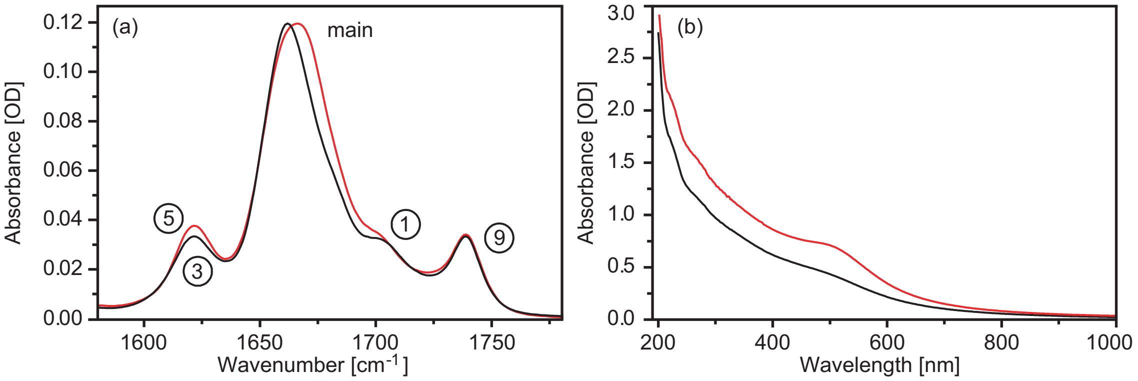

Figure 7.3: (a) FTIR spectra in the C=O stretching region and (b) UV/Vis spectra around the gold nanoparticle plasmon resonance recorded for nanoparticles **1** (black) and **2** (red) at equal effective peptide concentration of 10 mM. The four C=O bands at 1620, 1660, 1700, and 1739 cm^{-1} belong to the isotope labeled ^{13}C=O, the main band consisting of all six equivalent carbonyl groups, the urethane moiety and the ester group, respectively, and are labeled according to their positions in the peptide chain according to Fig 7.1. The UV/Vis spectra show the plasmon resonance peak around 520 nm, which is more pronounced for nanoparticle **2** due to the bigger diameter of its gold core.

7.3.2 Steady state spectroscopy

Steady state absorption spectra were recorded with commercial FTIR (BioRad FTS 175C) and UV/Vis (PerkinElmer Lambda 35) spectrometers, respectively. Figure 7.3 shows the FTIR and UV/Vis absorption spectra of the peptide-covered gold nanoparticles **1** (black) and **2** (red) measured at equal effective peptide concentration of about 10 mM in acetonitrile-d_3. Due to the spectrally separated absorptions of the capping layer and the metal core, the IR spectra are only sensitive to the applied peptide ligands, whereas the UV/Vis spectra exclusively show contributions from the gold core.

Along the lines of Chapter 6, the IR absorption bands observed in the amide I region can be assigned as follows: the intense main band at 1660 cm^{-1} consists of all equivalent peptide C=O groups in the helix (six in total). The isotope labeled ^{13}C=O peptide band (C=O #3 in **1**, C=O #5 in **2**) appears redshifted with respect to the main band at about 1620 cm^{-1}. The bands at 1700 cm^{-1} and 1739 cm^{-1} belong to the two chemically different C=O groups, which are the urethane moiety inserted close to the heated gold core at the N-terminus (C=O #1) and the ester group of the C-terminal Aib residue (C=O #9), the former not being completely spectrally resolved.

In the corresponding UV/Vis spectra the plasmon resonance of the gold nanoparticles appears at the expected position around 520 nm [114]. The spectrum of the smaller nanoparticle **1** only shows an unpronounced peak on top of an otherwise rather featureless absorbance ranging from the near-IR to the near-UV, which is a known effect for gold nanoclusters with diameters below ≈1.5 nm [128]. For the bigger nanoparticle **2**, in contrast, the plasmon band is much more distinct. Also away from the plasmon resonance band, the overall UV/Vis absorbance of nanoparticle **2** is increased compared to **1**, which is an additional size-related effect. Since the surface-to-volume ratio is decreased for bigger nanoparticles, a higher absolute particle concentration of **2** is needed to reach the same amide I peptide absorption in the IR.

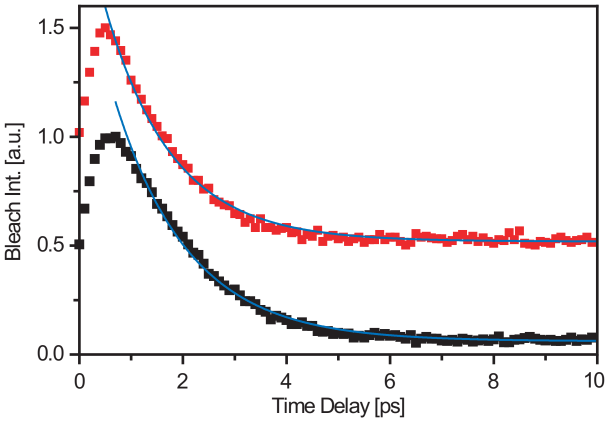

Figure 7.4: Transient absorption change recorded for nanoparticles **1** (black) and **2** (red, offset 0.5 for better visibility) measured at the maximum of the plasmon resonance band at 520 nm upon 400 nm excitation. The solid lines are exponential fits through the experimental data revealing cooling times of (1.4±0.2) ps for both samples.

7.3.3 Time-resolved spectroscopy

As discussed above, the rate at which energy is released from the heater into the attached peptide chains is determined by the decay of the initially pumped state. Therefore, to assess the time it takes for the gold cores to thermalize, that means to convert the electronic energy into heat, a UV pump/Vis probe experiment as described by Hartland and coworkers [115, 116] was performed. The nanoparticles were excited with laser pulses at 400 nm to generate a nonequilibrium electron distribution. The subsequent response was probed at the maximum of the plasmon resonance band at 520 nm, where the signal is proportional to the electron temperature [116]. From this measurement, relaxation times of (1.4±0.2) ps were obtained for both samples (Fig. 7.4). Hence, although the nanoparticle metal cores have different sizes, their thermalization behavior upon electronic excitation is very similar, so that their rates of energy release into the peptide capping layer can be treated as equal. The measured cooling rates are in agreement with Ref. [115], when extrapolating the reported relaxation times to smaller particle diameters. The different contributions of electron-phonon and phonon-phonon coupling cannot be distinguished for such small particles [115].

Whereas the energy release rates for both nanoparticles are the same, one possible difference between the samples is their initial temperature. Since the metal volume to be heated, as well as the energy uptake after laser excitation – which is basically determined by the UV/Vis absorbance – are different, the same should apply for the heat generation. However, as discussed in detail in Chapter 6, this effect does not influence the energy transport properties of the attached peptides, because vibrational energy diffusion through biomolecular chains is independent of the amount of initially deposited energy. Hence, the properties of vibrational energy flow, initiated by the given nanoparticles as local heat sources, can be directly compared.

The time-resolved Vis pump/IR probe spectra recorded in the C=O stretching region are displayed in Figure 7.5, a linear baseline determined from the edges of the spectral window was subtracted from all spectra to remove the contribution of free electrons in

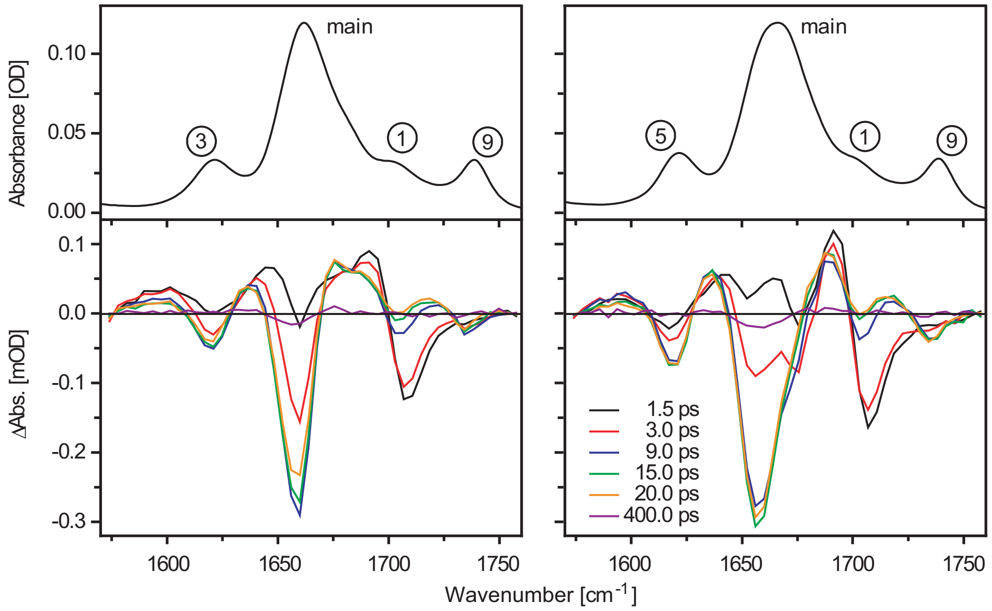

Figure 7.5: Transient IR spectra in the C=O stretching region for nanoparticles **1** (left column) and **2** (right column) recorded at various delay times (black, 1.5 ps; red, 3.0 ps; blue, 9 ps; green, 15.0 ps; orange, 20.0 ps; purple, 400.0 ps) after plasmonic heating of the gold nanoparticles at 520 nm. For comparison, the stationary absorption spectra of the respective nanoparticle samples are plotted above. The labels refer to the positions of the C=O groups relative to the heater (see Fig. 7.1).

the metal core appearing at early times. Subsequent to plasmonic excitation of the gold nanoparticles at 520 nm[a], heat is released into the peptide capping layer so that all backbone C=O modes exhibit redshifts, which are due to anharmonic coupling of the spectator modes to thermally excited lower-frequency modes [47]. As already discussed before, the bleach intensity is used as a measure of the amount of vibrational energy in the vicinity of the probe, because this signal is narrower than the anharmonically shifted hot band.

The main band at 1660 cm^{-1} shows the strongest response because it sums over the six nonlabeled peptide C=O oscillators in the helices. The kinetics of the main band bleaches of nanoparticles **1** and **2** are depicted in Figure 7.6 as cuts through the transient spectra at approximately 1660 cm^{-1}. The two samples clearly show different temporal responses: the transient absorption of **1** rises and decays faster, compared to **2**, so that its peak appears at earlier delay time (Fig. 7.6 inset). Biexponential fits reveal a rise time of 2.7 ps (4.4 ps) and a decay time of 38.0 ps (54.5 ps) for **1** (**2**). To exclude that the observed differences simply are effects of the different absolute nanoparticle concentrations, the effective peptide concentration[b] was varied over a wide range from 1.25 mM to 20 mM without observing changes in the kinetics or amplitude ratios, implying that the differences truly are due to an intra- and not an intermolecular effect. Hence, it can be concluded that

---

[a] All experiments were repeated for off-resonant excitation of the gold nanoparticles at 400 nm, revealing the same results (data not shown).

[b] The corresponding absolute particle concentrations can be calculated by dividing the effective peptide concentrations by the respective ligand coordination numbers of the samples, which are approximately 18 for nanoparticle **1** and 68 for **2**.

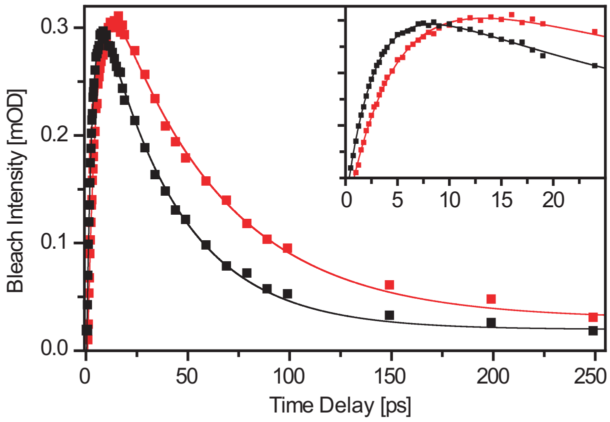

Figure 7.6: Time dependence of the bleach intensity of the main bands of nanoparticles **1** (black) and **2** (red) with opposite sign as in Fig 7.5, the inset shows the data at early times. The solid lines are biexponential fits to the data revealing rise and decay times of 2.7 ps and 38.0 ps for sample **1** as well as 4.4 ps and 54.5 ps for sample **2**. The final cooling of the peptide capping layer, is clearly accelerated for the smaller sample **1**.

the observed properties are inherent features given by the geometry of the nanoparticle samples: the peptide capping layers over the smaller nanoparticles cool faster.

Having discussed the initial injection of vibrational energy and the final size-dependent equilibration of the entire capping layers, the most interesting step to study is the energy transport along the peptide ligands. For this purpose spectrally resolved C=O bands have been placed at defined distances from the heat source, namely at peptide backbone positions approximately 0.4 nm, 0.8 nm, 1.2 nm and 2.0 nm away from the metal core (sites #1, #3, #5 and #9, respectively, compare Fig. 7.1b). In order to analyze their transient response, the second derivatives of the time-resolved spectra were taken to increase the spectral resolution and to correct for offsets, which is a common procedure for analyzing the amide I spectra of peptides and proteins [129]. The resulting bleach kinetics of nanoparticles **1** and **2** are depicted separately in Figure 7.7. To account for the effect of spectral congestion of the urethane band (belonging to C=O #1), the corresponding data were scaled up to match the long-time cooling dynamics of the other sites of the same sample. The sequential appearance of the maxima shows the propagation of vibrational energy along the helices: the farther a reporter unit is away from the heated gold core, the later the vibrational energy arrives and its amount is diminished. To analyze the energy transfer process, the experimental data were fitted with multiexponential functions (i.e., triexponential in the case of site #1 and biexponential for the others), the obtained time constants are summarized in Table 7.2. For site #1 a rise time τ_1 of 1.1 ps and a fast decay component τ_2 of 3.5 ps are consistently found for the measurements in both samples. The long-time cooling dynamics, however, are again different for both particles. The observed decay times τ_3 agree with those measured for the corresponding main bands, i.e. about 40 ps for sites #1, #3 and #9 in **1** (Fig. 7.7a) and 50 ps for sites #1, #5 and #9 in **2** (Fig. 7.7b).

Table 7.2: Time constants obtained from the bi- and triexponential fits to the data in Fig. 7.7. The time it takes for a heat signal to appear at a given site is reflected by its rise time τ_1. The subsequent cooling is described by a fast decay component τ_2 (site #1 only) and the slower overall equilibration time of the capping layer τ_3.

	site	τ_1 [ps]	τ_2 [ps]	τ_3 [ps]
Nanoparticle **1**	#1	1.1±0.1	3.5±0.4	38.0±1.0
	#3	2.5±0.1	—	37.7±1.6
	#9	5.4±0.7	—	36.2±2.0
Nanoparticle **2**	#1	1.1±0.1	3.5±0.3	50.0±1.0
	#5	4.7±0.2	—	51.6±2.0
	#9	7.7±0.6	—	49.8±2.1

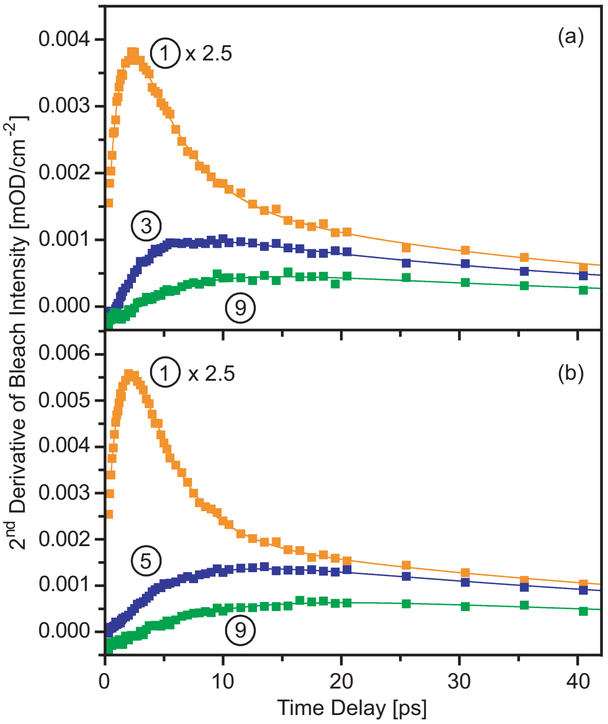

Figure 7.7: Time dependence of the bleach intensities of the spectrally resolved sites (a) #1, #3 and #9 (measured for nanoparticle **1**) and (b) #1, #5 and #9 (measured for **2**), extracted from the second derivatives of the transient IR spectra. The C=O bands are labeled as in all the previous figures. The solid lines are bi- and triexponential fits to the data, the obtained time constants are summarized in Tab. 7.2 above.

7.4 Discussion

From the UV-pump/Vis-probe experiment a thermalization time of approximately 1.4 ps was derived for the plasmonically heated gold nanoparticles. Since this lifetime determines the release of energy into the attached peptides, it is reflected by the response of the reporter group closest to the heater, which is site #1. The rise time of this C=O group, located only 0.4 nm away from the heated gold surface, was determined to $\tau_1 \approx$1.1 ps for both samples, which supports this interpretation.

After responding immediately to the heat generated in the gold core, site #1 subsequently cools into the following helical chain. This energy propagation process is reflected by the fast decay component τ_2 of 3.5 ps, which is also equal for both nanoparticle samples.

The final equilibration of the capping layer, however, is size-dependent so that the long-time cooling dynamics are different for both particles. Since the different cooling times τ_3 influence the points in time where the kinetic traces of the spectrally resolved C=O groups peak, the measurements from the two samples cannot be directly compared. Still, the propagation effect becomes clear by comparing the reporter units within the same sample whose responses peak delayed with a time-lag increasing with distance from the gold core, their rise times τ_1 are ordered accordingly.

As already discussed before, the different cooling times of the capping layer can be attributed to the dissimilar sizes of the nanoparticles, the exact reason is the following: since the packing efficiency is decreased for smaller particles [130], more solvent can penetrate into the capping layer accelerating the cooling process. This observation is also consistent with earlier energy transport studies on single peptides dissolved in organic solvents, where a much faster cooling time constant of approximately 7 ps was observed (compare Fig. 6.5 and the work by Botan *et al.* and Backus *et al.* presented in Refs. [43, 51, 52]). Single peptides can be considered the limit of infinitely small nanoparticle diameter. In this case, energy is dissipated into the solvent over a solid angle of 4π, and − if the peptide concentration is sufficiently low − does not affect other molecules. In contrast, energy dissipated from a peptide in the capping layer can appear in the nearby neighbor ligands so that the heat signal does not decay. The extreme case of this situation would be the infinite diameter of a bulk gold surface, where, due to exclusion of solvent, the peptides could only cool from their C-termini. Describing this crosstalk process between peptide ligands would require additional fitting parameters, so that the experimental data can no longer be globally described in the framework of an intuitive diffusive rate model as presented for the energy transport along single linear peptides (Fig. 6.6). However, also the individual fits of the transient bleaches, due to their exponential kinetics, prove the diffusive nature of the energy transport process.

Another characteristic of the plasmonically heated gold nanoparticles is that the heat signal at long delay times almost decays to zero (see 400 ps spectra in Fig. 7.5). In energy transport studies on single peptides, in contrast, an additional secondary heat effect resembling a stationary temperature difference spectrum remained even at very long delay times (compare Fig. 6.4). This is due to a temperature rise of the solvent leading to an overall weakening of the hydrogen bonds of the helix. As this effect originates from heating of the bulk solvent it also includes contributions from unpumped molecules and, as such, is concentration dependent [52]. In this study, however, such intramolecular effects are suppressed because the absolute nanoparticle concentration is very low ($\leq$1 mM).

The challenge when working with nanoparticles is that they can aggregate to large clusters and lose their nanoscale-related properties, coming along with a very distinct change in color, or when macroscopic clusters are formed, even with precipitation of the sample. Especially interaction with laser light can irreversibly destroy nanoparticles by fragmenting them into smaller units, which then aggregate with each other [131, 132] or, for high excitation flux, even by melting the lattice of the crystalline metal cores [133]. Also, the synthesis of peptide-capped nanoparticles is not trivial because adding thiol-containing amino acids or peptides as capping agents often induces aggregation [134,135]. Furthermore, as also encountered in this study, it is difficult to exactly control the size and size dispersion of the nanoparticles, because the formation of self-assembled peptide monolayers at the particle surface is sensitive to small changes of the reaction conditions.

Capping nanoparticles with an entire layer of peptides initiates energy transport through multiple ligands at the same time, which imposes a crosstalk that disturbs the evaluation of the energy transport properties of the individual biomolecular chains. Therefore, an idea for future experiments is to synthesize nanoparticles with mixed peptide capping layers [136] or so-called monofunctionalized nanoparticles [137–139], i.e., nanoparticles with just a few or even single biomolecules of interest included into a protective layer formed by some other stabilizing capping group.

7.5 Conclusion

In this chapter, plasmonically heated gold nanoparticles were introduced as a novel local heater for initiating vibrational energy transport through attached biomolecules. The subsequent propagation of vibrational energy is demonstrated by the sequential response of the C=O reporter groups in the peptide backbone; the exponential kinetics indicate the diffusive nature of this process. The urethane group (site #1) constitutes an internal standard, which lies very close (approximately 0.4 nm) to the gold metal core and responds immediately to the deposited heat. Already at site #3, approximately 0.8 nm away from the metal surface, a lag-time is observed and the amount of arriving vibrational energy has considerably decreased. The final equilibration of the capping layer is found to be size-dependent; due to the increased solvent penetration, capping layers applied to small nanoparticles cool faster. However, while the overall cooling depends on the solvent penetration, which is well-established [116, 140–142], the fast heating of the capping layer is only determined by its total heat capacity.

At the same time this study presents a new experimental approach for measuring the heat flow across organic capping layers over metal nanoparticles, which results in a more complete characterization of such a system after plasmonic excitation. Standard time-resolved spectroscopy in the visible, as presented in Section 7.3.3, is commonly used to determine the cooling times of plasmonically excited nanoparticles and to derive the thermal conductance of the metal/capping layer/solvent interface [116, 140–142], but cannot give information about the following transport and equilibration processes in the capping layer. By placing multiple reporter groups (^{13}C=O isotope labels and intrinsically spectrally resolved C=O groups) in a fixed geometric arrangement over the metal core, IR spectroscopy can be used as an additional spectroscopic technique to access the process of energy transport along the length of a capping ligand. Hence, with this method for nanoscale thermometry the rates and efficiencies of energy flow into and out of the capping layer can be measured, giving important information relevant for many plasmonic applications like optically activated drug delivery.

Chapter 8

Comparison of different local heating mechanisms

One of the aims of this thesis is to develop concepts to locally deposit vibrational energy at a given site of a biomolecule and to probe its arrival at any other site. Therefore, in the previous two chapters novel heating mechanisms have been presented and tested in short helical peptide chains. Together with the heating concept introduced by Botan *et al.* [43], now three alternative local heaters are available for initiating energy flow through peptide backbones. The purpose of this chapter is to compare their properties and to summarize some general properties of vibrational energy transport that could be extracted from those experiments.

Figure 8.1b recapitulates the measurements of vibrational energy flow through helical peptides obtained after excitation with the three distinctively different ultrafast heating mechanisms, which are in detail

i) the ultrafast photoisomerization of an electronically excited azobenzene chromophore that is covalently attached to one end of a peptide chain, presented in Ref. [43] (Fig. 8.1, left),

ii) the vibrational relaxation of the side-chain C−D modes of a fully deuterated leucine residue incorporated in a peptide sequence, introduced in Chapter 6 (Fig. 8.1, middle), and finally,

iii) the ultrafast cooling of a surface plasmon of a small, spherical gold nanoparticle capped with an entire monolayer of peptide ligands, introduced in Chapter 7 (Fig. 8.1, right).

The decays of the initially pumped states, which determine the speed at which energy is released from the heater into the attached peptides, are displayed in the insets of Figure 8.1b. The azobenzene chromophore, clearly, is the fastest of the three heaters, the ultrafast *cis-trans* isomerization proceeds on a 200 fs time scale, which is one of the fastest photoreactions ever observed [143]. The two other heaters are slower, the vibrational relaxation of the C−D modes in Leu-d_{10} and the thermalization of the plasmonically excited gold nanoparticle both occur on the 1 ps time scale.

All three heaters were tested in model systems comprising a short 3_{10}-helix, which was chosen due to its large stability. Also the detection of vibrational energy along the

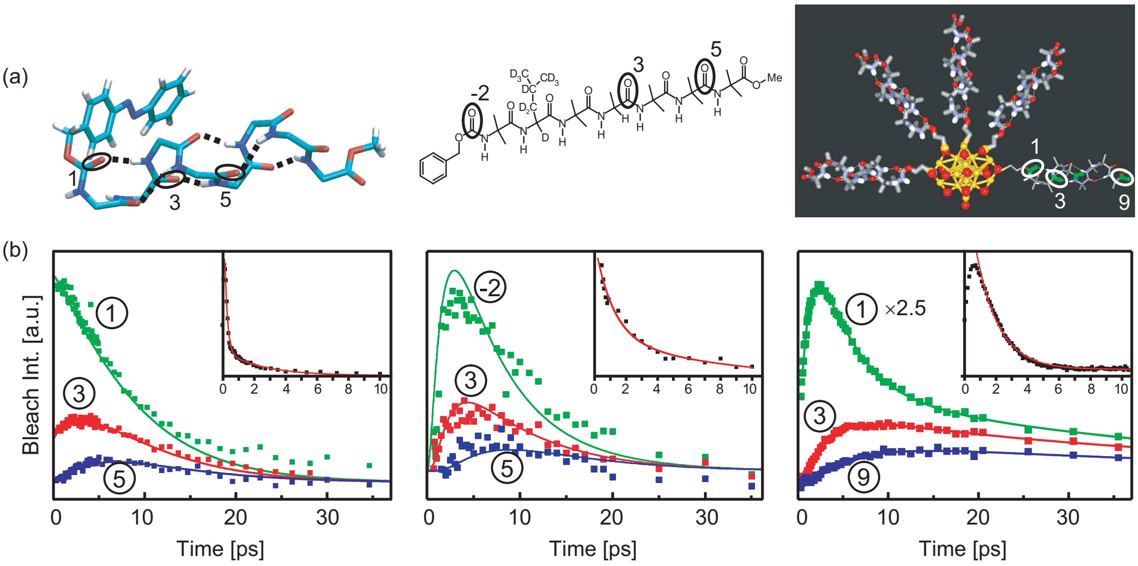

Figure 8.1: (a) Various heaters that have been employed for the localized deposition of vibrational energy: (left) photoisomerization of an azobenzene moiety; (middle) vibrational relaxation of C–D modes in Leu-d_{10}; (right) cooling of a surface plasmon of a small spherical gold nanoparticle. The local C=O thermometers that have been employed are labeled by their position relative to the heater. (b) Time-dependent responses of the various local thermometers after excitation of the corresponding heater. The insets show the decay of the initially excited states: (left) photoisomerization of azobenzene probed at 563 nm; (middle) vibrational relaxation of the C–D vibrations of Leu-d_{10}; (right) cooling of the gold nanoparticle plasmon resonance into the phonon system. The measurements displayed in the left panel are adapted from Ref. [43]; the data for the corresponding inset are published in Ref. [143] and were kindly provided by J. Wachtveitl and W. Zinth.

peptide backbone was equal in all three experiments: the appearance of vibrational energy at defined distances from the heat source was probed by employing spectrally isolated, localized C=O groups incorporated into the peptide sequence by labeling with ^{13}C isotopes and intrinsically spectrally resolved C=O groups (i.e., urethane or ester moieties). In either case the molecular systems were dissolved in organic solvents, that is chloroform (i and ii) or acetonitrile-d_3 (iii).

The obtained results show that qualitatively speaking the "temperature" response after excitation of either of the three different heaters is the same. In either case the decay of the initially pumped state determines the rise time of the group closest to the heater. At larger distances, the response peaks delayed with a time-lag that increases with distance from the heater. Energy losses along the chain, which are due to vibrational cooling into the solvent, are reflected by the sequential decay of the heat signals with increasing transport distance.

If possible, by fitting the data with a diffusive model that takes into account the particular boundary conditions in the various experiments, an apparent heat diffusion constant of ≈2 Å^{2}ps^{-1} is obtained. Interestingly, the vibrational energy transport rate does not depend on how and how much energy is deposited (varying from ≈3 eV when pumping the azobenzene moiety to ≈0.3 eV for the C–D vibrations), indicating that vibrational energy diffusion is linear. This result is also confirmed by a recent theoretical study by Stock and coworkers comparing different excitation schemes in an MD simulation [78]. The fact that the transport rate does not depend on how exactly the energy is deposited (i.e., all differences possibly related to specific initial conditions level out) shows that vibrational energy transport is not mode-specific, and hence, vibrational energy must be at least partially randomized on the picosecond time scale of transport.

As discussed in Chapters 3 and 4, it is mostly the low-frequency modes that transport vibrational energy very efficiently, similar to the situation in glasses, and hence would be responsible for the bulk value of heat diffusion. The different energy transport experiments show that the apparent heat diffusion constant observed on the given ultrashort length and time scales is much lower than in macroscopic experiments, as predicted in Chapters 3 and 4. This is because on the length scale of a few chemical bonds and the picosecond time scale, intrasite IVR rather than the actual transport along the chain is rate-limiting and determines the propagation speed, which explains the discrepancy to bulk values. From this experimental evidence it can be concluded that the localized high-frequency modes of an the amino acid site are not in equilibrium with the delocalized low-frequency transport modes. This means in particular that on the picosecond time scale of transport vibrational energy does not completely thermalize within the individual amino acid sites. However, when the energy does not follow an equilibrium Boltzmann distribution terms like “temperature” or “heat” in principle are invalid. Regarding this it is interesting to note that an apparent heat diffusion constant can be derived for the transport of nonthermal vibrational energy. This is because of the large number of modes involved, IVR has probabilistic character, and vibrational energy transport is diffusive-like, in the sense that it can be fitted by a rate equation system.

In summary, comparing the vibrational energy transport properties measured in the different experiments, it can be concluded that vibrational energy is largely randomized after either of the heating processes but not to the extent that it adopts an equilibrium Boltzmann distribution. Still, due to the probabilistic character of IVR, vibrational energy transport is diffusive-like and can be described by apparent heat transport properties.

Chapter 9

Toward vibrational energy transport in small proteins: villin headpiece 36

The previous chapters laid the ground for a deeper theoretical understanding of vibrational energy flow in biomolecules and introduced new heaters to experimentally explore energy transport properties. This chapter presents a preparatory study with the aim to move from exploring energy transport in model peptides to a small protein that folds into a three-dimensional, tertiary structure; villin headpiece 36. As local heaters for this experiment, a specifically-designed electronically excited azobenzene chromophore, and a small plasmonically heated gold nanoparticle are chosen, both of which depositing high amounts of vibrational energy on an ultrafast time scale. As a first step, the temporal behavior of the amide I band is measured, which reports on the averaged response of the entire protein upon local heating. As an outlook, the use of specific molecular labels for obtaining site-selective information about the energy transport process is discussed.

9.1 Introduction

By studying vibrational energy transport in short, helical model peptides, the properties of vibrational energy redistribution along one-dimensional molecular chains can be explored. However, questions how vibrational energy transport changes when undergoing a glass transition, if the active sites in a allosteric proteins communicate via exchange of vibrational energy, or if specific energy transport pathways – as they are consistently predicted from MD simulations – really exist, are related to the three-dimensional, structure of biomolecules. Hence, a natural next step is to extend vibrational energy transport experiments to proteins that fold into a tertiary structure. The ultimate aim of such a study is to vary both, the positions of the local heater as well as of the thermometers, so that finally a three-dimensional connectivity network can be mapped out, clarifying to what extent energy flow in proteins is anisotropic. An interesting question in this context is whether vibrational energy transport can occur between positions far away in the primary amino acid sequence but close by in the folded, tertiary protein structure, e.g., between different helices or other secondary structure motifs.

As a first step toward larger molecular structures the so-called villin headpiece 36

Table 9.1: Modified villin headpiece 36 sequences used for the energy transport experiments. Ser56 in the wild-type villin headpiece 36 was replaced by Cys56 to provide a specific anchor for a thiol-reactive local heater. The carbonyl groups of the amino acids Ala57 and Ala59 were $^{13}C{=}^{18}O$ isotope labeled (one at a time), indicated by A**. Note that the numbering of the amino acid residues is based on the full-length 76 residue villin headpiece, thus the first residue of villin headpiece 36 is assigned position 41, in consistency with former studies [144, 145].

Notation	**Sequence**			
	41 50	60	70	76
HP36WT (wild-type)	MLSDEDFKAV	FGMTRSAFAN	LPLWKQQNLK	KEKGLF
HP36Cys	MLSDEDFKAV	FGMTRCAFAN	LPLWKQQNLK	KEKGLF
HP36Cys-1	MLSDEDFKAV	FGMTRCA**FAN	LPLWKQQNLK	KEKGLF
HP36Cys-2	MLSDEDFKAV	FGMTRCAFA**N	LPLWKQQNLK	KEKGLF

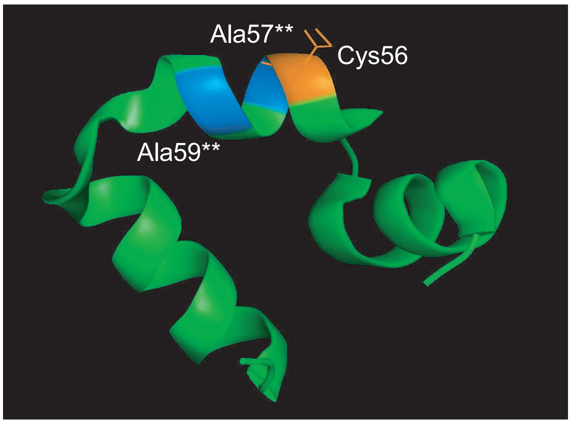

Figure 9.1: Structure of villin headpiece 36 with Cys56 highlighted in orange and the $^{13}C{=}^{18}O$-labeled residues Ala57 or Ala59 in blue (structure taken from 2F4K.pdb [147]).

(HP36) protein is chosen. The original full-length villin headpiece is a 76 residue domain that is found at the extreme C-terminus of the naturally-occurring protein villin. Its 35 C-terminal residues (HP35), plus one additional methionine at the N-terminus, form the helical HP36 subdomain with the sequence MLSDEDFKAVFGMTRSAFANLPLWKQQNLKKEKGLF (Tab. 9.1) [144, 145]. The NMR and X-ray structures of HP36 have been reported [146, 147], showing that the protein folds into three α-helices, two short ones formed by the residues Asp44 to Lys48 and Arg55 to Phe58 and a longer one from Leu63 to Lys72, which pack together to form the hydrophobic core (Fig. 9.1). This three-helix bundle HP36 is probably the smallest polypeptide that may be called a protein, in the sense that it folds cooperatively into a tertiary structure with a hydrophobic core without stabilizing disulfide bonds or cofactors [147]. Due to its small size, high stability and rapid folding dynamics, HP36 is an extremely popular target in basic protein research and has been studied extensively both experimentally [145–153] and theoretically [154–158]. With 36 amino acids the protein is still small enough to synthesize it in a peptide synthesizer amino acid by amino acid, an important prerequisite to readily perform site-selective labeling with isotope modified, or nonnatural amino acids.

9.2 Materials and Methods

To attach a local heater at a defined position in the protein, the serine residue at position 56 in the wild-type villin headpiece 36 (HP36WT) was substituted by a cysteine residue (HP36Cys). This sequence position was chosen to place the thiol side chain of the cysteine, which provides a specific anchor for coupling any thiol-reactive local heater, in a solvent-exposed position that can be attacked in a linking reaction.

In addition, the carbonyl groups of the close-by amino acids Ala57 (HP36Cys-1) and Ala59 (HP36Cys-2) were $^{13}C{=}^{18}O$ isotope labeled (one at a time) to obtain local reporter groups [50]. These doubly-labeled isotopes were chosen to introduce a bigger frequency shift of about 65 cm^{-1} − compared to about 40 cm^{-1} for the lighter $^{13}C{=}^{16}O$ labels used in the experiments presented in Chapters 6 and 7) − which is usually necessary for distinguishing the IR absorbance of a labeled peptide group from the broad amide I band of a protein. Furthermore, due to the natural abundance of ^{13}C, which is about 1.1%, the $^{13}C{=}^{16}O$ absorbance of the 36-residue villin headpiece is already around 40% of the intensity of a single $^{13}C{=}^{16}O$ label, thus leading to considerable spectral overlap.

For the synthesis of the isotope modified sequences, $^{13}C{=}^{16}O$-alanine was purchased from Cambridge Isotope Laboratories, Inc. as L-Ala, 1-13C 99% (CLM-116-1). By isotope exchange in ^{18}O-water ($H_2{}^{18}O$), as described in Ref. [50], $^{13}C{=}^{18}O$-alanine was obtained and, subsequently, protected by a fluorenylmethyloxycarbonyl (Fmoc) group. All villin headpiece 36 sequences were chemically synthesized on a peptide synthesizer by GL Biochem (Shanghai) Ltd. using standard solid-phase Fmoc protocols to achieve a stepwise coupling of each amino acid. The obtained proteins were purified through high performance liquid chromatography (HPLC) and their identity verified by mass spectroscopy. An overview of the different, manipulated protein sequences is given in Table 9.1. The numbering of HP36 is based on the original 76 residue villin headpiece, thus the first residue in HP36 is assigned position 41, in consistency with former studies [144].

For the energy transport studies based on the ultrafast photoisomerization of an azobenzene chromophore, the latter was coupled to the thiol group of Cys56[†]. It turned out that the water-solubility of the azobenzene moiety is crucial to prevent protein aggregation and precipitation. Therefore, to increase the water-solubility, a sulfonated version of an azobenzene moiety, 4-Chloroacetamido-azobenzene-3,4'-disulfonic acid (Acid yellow chloracetyl, AYC) was synthesized, similar to that suggested by Woolley and coworkers [159, 160]. The synthesis of the water-soluble azobenzene photoswitch and its linking to the thiol-containing villin headpiece protein are described in detail in Appendix D. The obtained azobenzene-linked protein samples were again HPLC purified and their molecular weight confirmed by mass spectroscopy. Since the absorbance of residual trifluoroacetic acid (TFA), originating from the protein synthesis and HPLC, overlaps the amide I band, TFA was removed from the purified proteins by liquid chromatography (Bond Elut SAX; Varian) columns rinsed with H_2O, 100 mM phosphate buffer, and 1 mM HCl.

To initiate energy transport through villin headpiece with plasmonically heated nanoparticles, small, spherical gold nanoclusters capped with a mixed protein/polyethylene

---

[†] The synthesis of the azobenzene-linked proteins was contributed by Rolf Pfister.

glycol (PEG) monolayer were synthesized[‡]. For this purpose, first, citrate-reduced, tannic acid-capped gold nanoparticles, with a size distribution of about (5.0±0.5) nm were synthesized by a standard protocol described in Ref. [161]. Subsequently, a mixture of thiolated PEG and the respective thiol-containing HP36 protein was used to achieve a ligand exchange with the tannic acid on the particle surface [136]. By varying the concentrations of the two thiol-containing substances, the HP36/PEG ratio on the nanoparticle surface can be controlled, leading to nanoparticles with a few villin headpiece proteins coupled to the gold surface that is otherwise protected by PEG – a capping agent without any disturbing vibrational bands in the spectral region of interest. The obtained nanoparticle-protein conjugate was purified by gel-filtration chromatography, which also removed residual TFA from the protein synthesis.

Unless otherwise indicated all protein samples were dissolved in a 10 mM sodium phosphate buffer, at pD 7 in D_2O (uncorrected pH meter reading) and kept between 2-mm-thick CaF_2 windows separated by a 50 μm spacer. For the time-resolved laser measurements of the azobenzene-linked proteins, the sample was circulated in a closed cycle flow cell ensuring complete exchange of the sample volume between two successive laser shots, and was additionally irradiated with CW light from an LED emitting at 375 nm to accumulate the azobenzene chromophore in its *cis*-state. The protein concentrations reached for these experiments were about 1-2 mM. As already discussed in Chapter 7, a major advantage of nanoparticles is that they do not bleach upon photoexcitation, allowing for the use of a static sample cell with much lower sample volume. Consequently, effective protein concentrations of ≈5 mM could be afforded for the experiments on the nanoparticle-linked villin headpiece samples.

9.3 Results

9.3.1 Circular dichroism

To determine how the mutation of Cys56 and the subsequent attachment of a local heater affect the conformation and stability of the used HP36 sequences, circular dichroism (CD) spectroscopy measurements were performed. CD spectroscopy in the far-UV spectral region is a versatile technique for determining the secondary structure of proteins. Different structural motifs like α-helices, β-sheets or random coils can be recognized from the very characteristic shapes and magnitudes of their CD spectra [162]. Furthermore, CD spectroscopy also enables for determining the thermodynamics of protein unfolding. By measuring the CD signal at a characteristic wavelength – which monitors some specific feature of the protein secondary structure – as a function of temperature, the thermal stability of proteins can be assessed [163].

Circular dichroism spectra were recorded with a commercial spectropolarimeter (Jasco J-810). For the CD measurements HP36 sample[a] was dissolved at a low concentration of ≈10-20 μM in the previously described 10 mM sodium phosphate buffer, and kept in quartz

---

[‡] The synthesis of the nanoparticle-protein conjugate was contributed by Shabir Hassan.

[a] Due to the strong plasmon absorption (compare Fig. 9.4b) the nanoparticle-linked protein samples could not be characterized by CD spectroscopy in the far-UV. To assess the thermal stability of these samples, vibrational CD spectroscopy in the amide I region is currently performed.

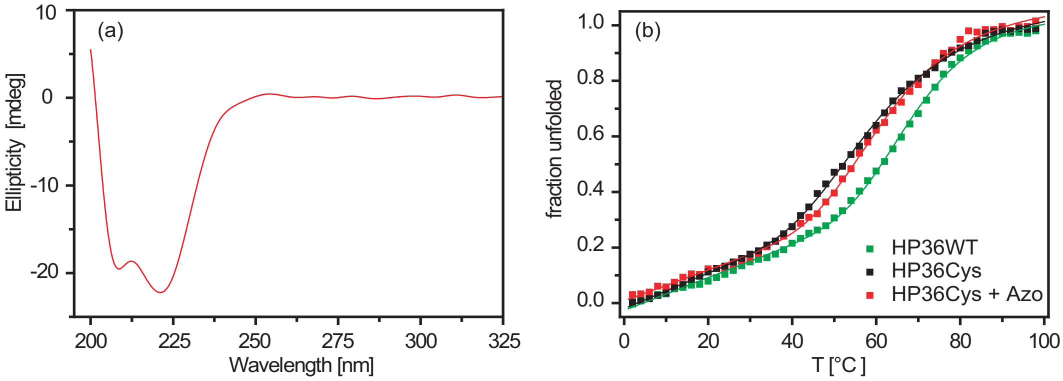

Figure 9.2: Circular dichroism spectra of the HP36 samples. (a) CD spectrum of HP36Cys with azobenzene, recorded at room temperature, showing the typical α-helix signature. (b) Thermal unfolding curves obtained by monitoring the ellipticity at 222 nm as a function of temperature. The figure shows the unfolded fraction of proteins for HP36WT (green) as well as for HP36Cys without (black) and with (red) the water-soluble azobenzene moiety. The solid lines are two-state fits through the experimental data revealing a melting temperature of $T_m \approx 71°\mathrm{C}$ for the wild-type protein and $T_m \approx 65°\mathrm{C}$ for both HP36Cys mutants.

cell with 10 mm optical path length. The far-UV CD spectrum obtained for HP36Cys with the azobenzene moiety attached is displayed in Figure 9.2a, showing the typical α-helix signature, i.e. two negative bands at 208 and 222 nm [162]. Hence, mutation of Ser56 to Cys56 and addition of the azobenzene moiety does not seem to change the natural α-helix bundle conformation of the villin headpiece protein.

To characterize the thermal stability of the HP36 samples the ellipticity at 222 nm was followed as a function of temperature and used to calculate the fraction of unfolded proteins. The measured unfolding curves (Fig. 9.2b) show the loss of secondary structure with temperature. To extract the melting temperatures T_m the obtained equilibrium unfolding data were fitted by a two-state model

$$y(T) = \frac{(m_N T + b_N) + (m_D T + b_D)\exp\left[\frac{\Delta H}{R}\left(\frac{1}{T_m} - \frac{1}{T}\right)\right]}{1 + \exp\left[\frac{\Delta H}{R}\left(\frac{1}{T_m} - \frac{1}{T}\right)\right]}, \tag{9.1}$$

where ΔH is the unfolding enthalpy, T_m the melting temperature, R the gas constant, and the remaining parameters represent the slope and offset of the baseline [164]. HP36WT is the thermally most stable protein sequence, the determined melting temperature $T_m \approx 71°\mathrm{C}$ is in very good agreement with the result reported in Ref. [144]. The two samples with Cys56 mutated both show a melting temperature $T_m \approx 65°\mathrm{C}$, which is about 5°C lower than for HP36WT. Almost no difference can be observed between the HP36Cys samples with and without the azobenzene moiety. Hence, mutation of Ser56 to Cys56 results in a thermally slightly less stable protein, the additional attachment of the azobenzene photoswitch, however, does not lead to a further destabilization. Still – and this is the crucial point – the melting temperature of the manipulated HP36 sequences is sufficiently high so that the predominant fraction of proteins remains folded at room temperature.

If the unfolded proteins aggregate and/or precipitate, the melting reaction will be irreversible. Therefore, the reversibility of the unfolding reaction was confirmed by cool-

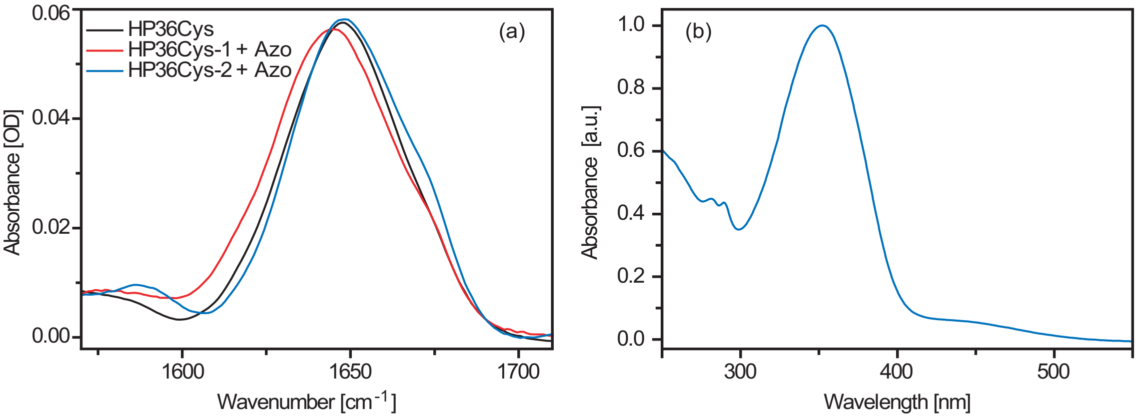

Figure 9.3: (a) FTIR spectra in the amide I region, recorded for nonlabeled villin headpiece 36 without local heater unit HP36Cys (black) and the two labeled isotopomers HP36Cys-1 (red) and HP36Cys-2 (blue) with azobenzene, at a concentration of 1-2 mM. Isotope labeling leads to an absorbance increase in the 1590 cm^{-1} region but the labels are not clearly separated. Linking with the azobenzene moiety leads to the appearance of a small shoulder around 1670 cm^{-1}, probably due to the C=O group of the linker unit. The absence of a large absorption feature at 1615 to 1620 cm^{-1} clearly shows that the proteins do not aggregate [49], even upon attachment of azobenzene. (b) UV/Vis spectrum of azobenzene-linked HP36Cys-2, recorded in the *trans*-state. The bands at 350 nm and 450 nm can be assigned to the $\pi\pi^*$ and $n\pi^*$ transitions of *trans*-azobenzene, respectively. The additional band at 280 nm is due to the tryptophan absorption of HP36.

ing and re-heating the sample reproducing the same unfolding curve (data not shown). However, it should be borne in mind that the low concentrations used in CD experiments ($\approx$10-20 μM) disfavor of aggregation. Therefore, the fact that the protein sample does not aggregate under the experimental conditions of CD measurements must not necessarily be true for IR experiments, carried out at a 50-100 times higher concentration ($\approx$1-2 mM, compare Section 9.3.3).

9.3.2 Steady state spectroscopy

Steady state absorption spectra were recorded with commercial FTIR (BioRad FTS 175C) and UV/Vis (PerkinElmer Lambda 35) spectrometers, respectively. Figure 9.3a shows the FTIR spectra of the nonlabeled villin headpiece 36 without heater unit HP36Cys (black), as well as the two labeled isotopomers HP36Cys-1 (red) and HP36Cys-2 (blue), both linked with azobenzene. All protein samples show a broad amide I band centered at approximately 1645 cm^{-1}, as it is expected in D_2O [49].

Whether a protein is in its native state or aggregated can be easily assessed from IR spectra because aggregated proteins exhibit a characteristically shaped amide I band with a dominating feature around 1618 cm^{-1} and a minor component at the high-frequency edge of the amide I region [49]. The absence of this aggregation signature in the measured FTIR spectra clearly shows that the azobenzene-linked proteins at room temperature remain intact, even at the high concentrations needed for the IR experiments.

Compared to the unlabeled compound HP36Cys, the FTIR spectra of the $^{13}C{=}^{18}O$ labeled samples HP36Cys-1 and HP36Cys-2 show an absorbance increase in the 1570-

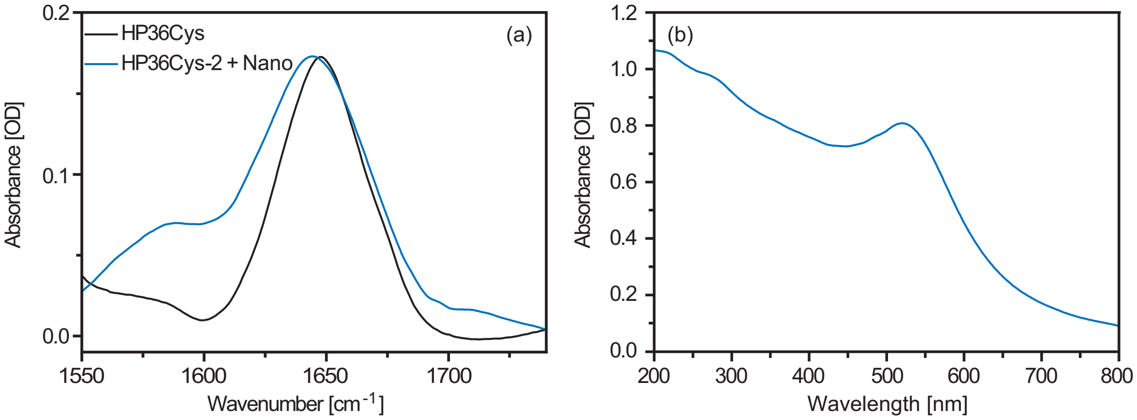

Figure 9.4: (a) FTIR spectrum in the amide I region and (b) UV/Vis spectrum around the gold nanoparticle plasmon resonance recorded for HP36Cys-2 proteins attached to a gold nanoparticle, recorded at an effective protein concentration of ≈5 mM. For comparison, the scaled spectrum of free HP36Cys is plotted in black. The absence of a characteristic aggregation feature at 1615 to 1620 cm^{-1} shows that the proteins remain intact [49]. The UV/Vis spectrum shows the plasmon resonance peak around 520 nm, and a small shoulder of the tryptophan absorption of the protein appearing around 280 nm.

1600 cm^{-1} region, without clearly separated isotope labels being observed, in accordance with Ref. [151]. The reason for this is a broad absorption of side-chain carboxylate (COO$^-$) groups of the aspartic acid (Asp44 and Asp46) and glutamic acid (Glu45 and Glu72) residues appearing in the region around 1560-1600 cm^{-1} [151], which overlaps the expected position of the isotope labeled amide I band (1572 cm^{-1} [150]).

The addition of azobenzene to the villin headpiece 36 samples does not significantly change the FTIR spectra recorded in the amide I region. The appearance of a shoulder around 1670 cm^{-1} is most probably due to absorbance of the C=O group in the linker unit of the azobenzene moiety (the chemical structure of AYC can be found in Appendix D, Fig. D.1).

Figure 9.3b shows the corresponding UV/Vis spectrum of azobenzene-linked HP36Cys-2, recorded in the *trans*-state of the photoswitch. The dominating band at 350 nm and the weak band around 450 nm can be assigned to the $\pi\pi^*$ and nπ^* transitions of *trans*-azobenzene, respectively. Illumination around 375 nm induces a *trans*-*cis* isomerization, leading to an intensity decrease of those bands and the appearance of a new band around 435 nm, belonging to the nπ^* transition of *cis*-azobenzene [160]. A complete set of UV/Vis spectra of the photoinduced isomerization of the water-soluble AYC moiety can be found in Appendix D, Figure D.2. The additional absorbance band appearing around 280 nm can be assigned to the tryptophan absorption (Trp64) of the HP36 protein [165].

Figure 9.4a shows the FTIR spectrum of HP36Cys-2 proteins linked to a small gold nanoparticle (blue). Compared to the free HP36Cys protein, whose scaled absorption spectrum is plotted for comparison (black), the amide I band of the nanoparticle-linked villin headpiece 36 is slightly shifted and broadened, indicating that the protein structure possibly changes when attached to the nanoparticle gold surface. However, the HP36 proteins incorporated in the nanoparticle capping do not aggregate, which, again, can be concluded from the absence of the corresponding absorption features in the amide I spectrum.

The corresponding UV/Vis spectrum is displayed in Figure 9.4b showing the plasmon resonance of the gold nanoparticles at the expected position around 520 nm [114]. In contrast to the 1-2 nm gold nanoparticles used for the experiments presented in Chapter 7 (compare Fig. 7.3b), the plasmon band absorption of these ≈5 nm particles is much more distinct. As already observed for the azobenzene-linked HP36 proteins, the tryptophan absorption of the protein can be identified as a shoulder around 280 nm.

9.3.3 Temperature-difference FTIR spectroscopy

To characterize the thermal stability of HP36Cys at the high sample concentrations necessary for the IR experiments, equilibrium FTIR spectra of the amide I region were recorded as a function of temperature in the range 2°C to 77°C in increments of 5°C. Absorbance spectra were calculated as the negative logarithm of the ratio between the single-beam spectra of protein sample and solvent background that were recorded separately at each temperature. To monitor the temperature-induced changes of the amide I band, difference spectra were calculated by subtracting the absorbance spectrum at the lowest temperature from each spectrum taken at higher temperature.

The thermal unfolding spectra obtained for HP36Cys without heater are displayed in Figure 9.5 and resemble those reported for HP36WT (compare Fig. 2a in Ref. [145]). The difference spectra show negative features in the frequency range of 1615-1650 cm^{-1}, which are due to the loss of secondary and tertiary structure, and positive features around 1650-1750 cm^{-1}, resulting from the formation of more disordered regions [145,150], both features increase in intensity with increasing temperature. The absence of a single isosbestic point indicates the presence of more than one unfolding transition and is a known characteristic of the melting behavior of villin headpiece 36 [145, 150]. The observed blueshift of the amide I band is a common feature of protein unfolding transitions, because the loss of secondary and tertiary structure goes along with a weakening or even breaking of the C=O...H−N hydrogen bonds [98], which increases the restoring force and, consequently, also the frequency of the C=O stretching vibration [49].

Contrary to what was reported for HP36WT [145], heating to temperatures above ≈45°C causes an additional feature to rise at 1618 cm^{-1}, indicating that the HP36Cys proteins aggregate when unfolded. Even while cooling the sample down to its initial temperature this peak is still increasing in intensity, obviously not as a function of temperature but rather dependent on the time spent in the unfolded state[b]. Comparing the lowest-temperature spectra recorded before and after heating (Fig. 9.5 inset), a residual absorbance increase with distinct features at 1618 cm^{-1} and also 1680 cm^{-1} evidences that part of the proteins has aggregated [49], rendering the melting process irreversible.

Hence, the mutated sequence HP36Cys is no longer as stable as the wild-type villin headpiece HP36WT; the thermally unfolded proteins have a propensity to aggregate at high sample concentration. The incorporation of a cysteine can of course lead to the formation of disulfide-bound dimers between thiol groups, whose effect on protein aggregation is not clearly understood [166]. However, it is unlikely that thiol-mediated dimerization is the cause of aggregation in this case, because blocking the thiol side chain by an azobenzene

---

[b] The measurement time for a complete heating-cooling cycle was about 6 h.

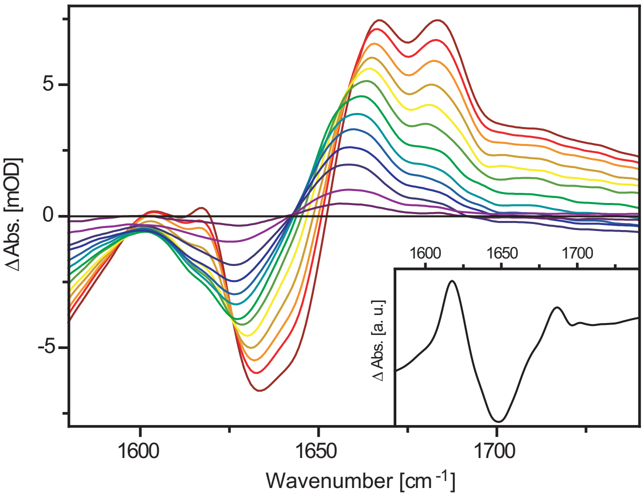

Figure 9.5: Difference FTIR spectra of HP36Cys without local heater unit recorded as a function of temperature from 2°C to 77°C in steps of 5°C, calculated by subtracting the spectrum at 2°C from each spectrum taken at higher temperature. The spectra are color coded from blue (cold, 2°C) to red (hot, 77°C). The inset depicts the residual difference between the spectra recorded at 2°C before and after the melt, showing a characteristic aggregation signature.

photoswitch does not ease the problem. On the contrary, temperature-induced aggregation becomes even more severe in the presence of the azobenzene (also the water-soluble version) and is particularly sensitive to the conditions during the linking reaction. If the same is true for nanoparticle-linked protein samples is still under examination.

Protein aggregation is a tedious problem at the high sample concentrations necessary for IR spectroscopy. However, by choosing a water-soluble azobenzene moiety or a suitable protocol for obtaining protein-functionalized nanoparticles, it is possible to attach local heaters to cysteine-containing villin headpiece mutants without disturbing their folded state at room temperature. As long as laser-induced heating does not cross a certain threshold temperature, irreversible protein aggregation should be avoidable.

9.3.4 Time-resolved spectroscopy

The intention of the time-resolved infrared spectroscopy experiments is to study energy transport in the HP36 protein by exciting the respective local heater attached to the Cys56 residue, and to follow the subsequent energy flow by employing backbone ^{13}C=^{18}O probes at different distances from the heat source as local thermometers. For this purpose UV pump/IR probe experiments were performed on the transient IR spectroscopy setup described in Section 5.2. The initial temperature gradients generated in such experiments, right after laser-excitation, can be estimated to be on the order of 1000 K for the azobenzene [43] and, depending on the particle size, around 300 K for the gold nanoparticles. Despite these high initial temperature gradients the final temperature jump – once the pump energy is dissipated into the bulk solvent – is only on the order of 1 K [43]. Hence, starting from room temperature, where the proteins are still folded, a laser-induced temperature jump of that order should not bring the protein into a temperature regime where aggregation starts.

In a first experiment, the water-soluble azobenzene photoswitch, that had been accumulated in its *cis*-state, was excited at a wavelength of 415 nm. The following photoinduced *cis-trans* isomerization deposits a large amount of vibrational energy into the attached HP36 protein. The obtained time-resolved UV pump/IR probe spectra recorded in the C=O stretching region of HP36Cys-2 are displayed in Figure 9.6a.

Upon excitation of the azobenzene chromophore, its ring modes can be observed at 1590 cm^{-1} and 1670 cm^{-1} (compare the FTIR spectrum of AYC, which is given in Appendix D, Fig. D.2b), decaying on a 5 ps time scale. Although located close to the local heater, no signal of the $^{13}\mathrm{C}{=}^{18}\mathrm{O}$ labeled Ala59 could be detected, meaning that no site-selective information can be extracted from this experiment. The spectral response of the protein amide I band shows a blueshift that appears on the 20 ps time scale.

Since the transient spectra closely resemble the equilibrium temperature-induced difference spectra presented in Section 9.3.3, this response can be attributed to the elevated temperature upon laser heating. The generated temperature rise leads to an ultrafast destabilization of the hydrogen bonds [98], which results in the previously discussed frequency increase of the C=O stretching vibrations [49]. However, large-scale structural changes like complete unfolding of the protein do not occur on these ultrafast time scales; the unfolding time of HP36 has been reported to be on the order of a few microseconds [145]. A similar behavior of the main amide I band was reported by Botan *et al.* in the case of azobenzene-induced energy transport in 3_{10}-helical peptides [43]. Also in the energy transport studies presented in Chapters 6 and 7, a blueshift could be measured, however, only as a secondary effect appearing on longer time scales, once the locally-deposited excess energy was dissipated into the bulk solvent.

Note, that in the course of this experiment the heated HP36 proteins accumulated on the used CaF_2 windows. Hence, all time-resolved data presented on the azobenzene-linked HP36 were measured, at least partially, in a protein film and not in solution so that in particular no cooling dynamics could be measured.

In a second experiment, small gold nanoparticles carrying a few HP36 proteins were excited at a wavelength of 400 nm. This pump wavelength was chosen for reasons of simplicity because it can easily be generated by frequency-doubling of the Ti:sapphire fundamental beam. As discussed in Chapter 7, after plasmonic heating of nanoparticles, the energy transport properties of the capping layer do not depend on the excitation wavelength. The time-resolved Vis pump/IR probe spectra recorded in the C=O stretching region are displayed in Figure 9.6b, a linear baseline determined from the edges of the spectral window was subtracted from all spectra to remove the contribution of free electrons in the metal core appearing at early times.

As already observed after pumping of the azobenzene chromophore, the measured response of the amide I band resembles the equilibrium unfolding data, indicating ultrafast hydrogen bond weakening in the attached proteins. In contrast to the azobenzene experiment, however, the blueshift partially decays on the time scale of the experiment. The inset in Figure 9.6b displays the main band dynamics as a cut through the transient spectra at 1670 cm^{-1}, showing the rise and decay of the blueshift with a 10 ps and 130 ps time constant, respectively, until a stable signal offset is reached. In accordance with Ref. [43], the partial decay of the temperature-induced frequency shift is assigned to heat diffusion from the first solvation shell into the bulk solvent, allowing the protein to restabilize.

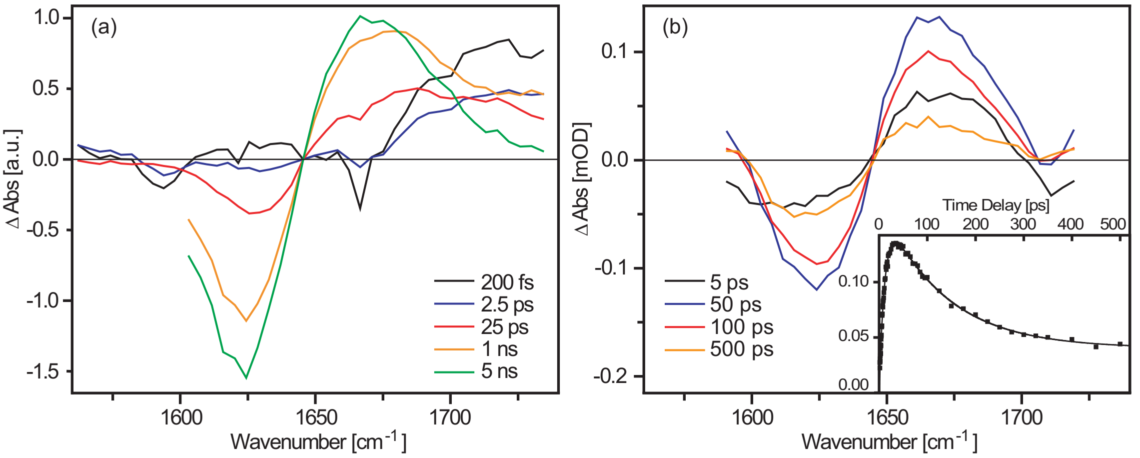

Figure 9.6: Transient IR spectra recorded in the amide I region at various delay times after local heating of HP36Cys-2. (a) Response after excitation of the water-soluble azobenzene moiety showing the decay of the azobenzene ring modes and the ultrafast destabilization of the protein hydrogen bonds. (b) Response after plasmonic heating of the gold nanoparticles. The inset shows the kinetics of the main band shift as a cut through the transient spectra at 1670 cm^{-1}. A biexponential fit through the obtained data reveals a rise time of 10 ps and a decay time of 130 ps.

9.4 Discussion and Outlook

In this chapter, it was successfully demonstrated how cysteine-containing villin headpiece 36 mutants can be coupled to two very different, thiol-reactive local heater units without causing the proteins to aggregate at millimolar concentrations and room temperature. Subsequently, both local heating mechanisms – the electronic excitation of a water-soluble azobenzene chromophore and the plasmonic heating of a small gold nanoparticle – were triggered with laser pulses in the UV spectral range without driving the attached proteins into temperature regimes where irreversible aggregation starts. In both heating schemes, the measured time-resolved IR spectra show a blueshift of the protein amide I band, indicating that laser excitation generates an ultrafast temperature jump, which destabilizes the hydrogen bonds of the protein.

The difficulty in all experiments was that the ^{13}C=^{18}O isotope labels could not be detected, neither in the absolute FTIR nor in the difference pump-probe spectra, so that no site-selective information could be obtained. While isotope labeling is well-established for small peptides, transferring this method to proteins is challenging. In contrast to tailored peptides, which consist of only a few different amino acids, in real proteins the stretching region of isotope labeled C=O groups is often overlapped by absorbance from multiple side chains. The most problematic side chains in this regard are the COO$^-$ bend of glutamic and aspartic acid, the NH$_2$ bend of asparagine and glutamine as well as the C=NH$_2$ mode of arginine [75].

A solution to this problem could be the use of other residue specific labels that absorb in uncongested areas of the protein IR spectrum. For example, the azido (N$_3$) group has been suggested as an alternative, nonperturbative IR probe [167], which can be incorporated into proteins by standard synthetic methods via substitution with the azido-bearing,

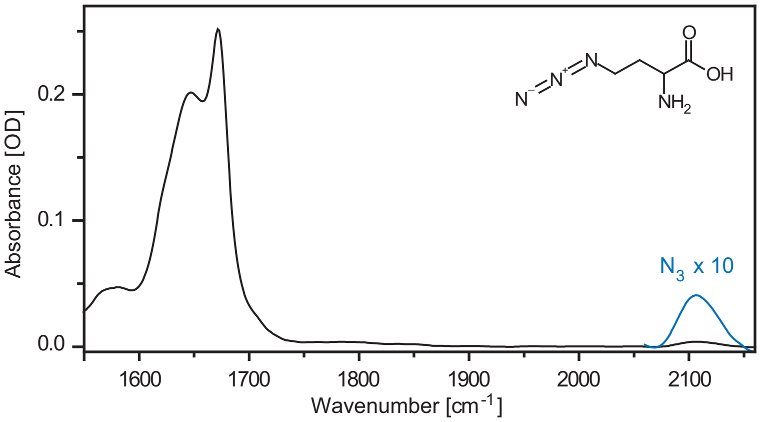

Figure 9.7: Chemical structure of Aha and FTIR absorption spectrum of HP36Cys-Aha in the spectral region of the amide I and the azido vibration, recorded at a protein concentration of 5-6 mM in buffered D_2O at pD 7. For better visibility the azido band is scaled up by a factor of 10 (blue). The sharp peak appearing at 1672 cm^{-1} is due to residual TFA absorption.

nonnatural amino acid azidohomoalanine (Aha) [168]. Similar to the C=D groups introduced in Chapter 6, the absorbance of the azido vibration lies in the “transparent window” between 1800 and 2600 cm^{-1} so that this reporter group, due to the large frequency separation to the remaining protein vibrations, can be considered largely localized.

To elucidate the applicability of Aha as a local reporter group for energy transport experiments in the villin headpiece 36 protein, commercially available Fmoc-protected Aha (Chiralix) was incorporated into HP36 by standard solid-phase Fmoc protocols. Since Aha can be viewed as an analogue of methionine, as a first test, Met53 in the HP36Cys sequence was replaced by an Aha residue, leading to a villin headpiece protein with the sequence MLSDEDFKAVFG-Aha-TRCAFANLPLWKQQNLKKEKGLF (HP36Cys-Aha). The FTIR spectrum of this azido labeled protein, measured at a concentration of 5-6 mM in phosphate buffered D_2O[c] is shown in Figure 9.7. As already displayed in Figure 9.3 the amide I band of HP36 can be observed at 1645 cm^{-1} (here, overlapped by a sharp TFA absorption at 1672 cm^{-1}), the azido band appears at 2105 cm^{-1}. From this measurement the extinction coefficient of the azido label can be estimated to $\approx$150 M^{-1}cm^{-1}, which is very similar to what was reported for Aha incorporated into the NTL9 protein [168] but does not reach the values reported for free Aha ($\approx$450 M^{-1}cm^{-1}) [167]. Still, the azido label is a relatively strong IR absorber that can almost compete with the molar absorptivity of a C=O vibration, which is on the order of 300 M^{-1}cm^{-1}. The IR absorption of the azido group is sensitive to its environment: for the azido group of Aha53 – which is situated in a solvent-exposed position between two α-helices – a spectral width of $\approx$40 cm^{-1} (FWHM) is measured, which is much broader compared to a C=O isotope label ($\approx$20 cm^{-1}). Consequently, difference signals caused by temperature-induced frequency shifts are expected to be smaller. Although the IR absorption of the

---

[c] The solvent D_2O was chosen to access both the amide I and the azido region. However, the steep rise of the D_2O background absorbance in the region of interest can cause strong offsets so that H_2O might be the better solvent for detecting azido labels in energy transport experiments.

azido vibration is weaker and broader compared to the C=O stretch, Aha is a promising protein label because its absorbance band appears in an uncongested region of the protein IR spectrum, where it can be identified in a nonambiguous manner.

In any case, detecting the transition of a single molecular group in a larger protein will be challenging. For the experiments on small peptides dissolved in organic solvents, highly-concentrated samples with relatively large optical path lengths could be prepared to obtain signal strengths detectable with the employed infrared pump-probe setup (compare Section 5.2). However, for low protein concentrations in thin, aqueous solution samples the sensitivity limit of this method will be reached. Hence, for the planned energy transport experiments on site-specifically labeled proteins a setup with improved detectivity is required. A well-established method for increasing the sensitivity of nonlinear optical measurements is to generate the third order signal in the transient-grating geometry and to heterodyne it with a reference field, the so-called local oscillator [169]. Therefore, the aim is to replace the classical pump-probe setup with a heterodyne-detected Vis-IR transient-grating setup, which is currently under construction, and is expected to improve the signal-to-noise ratio by one order of magnitude [170].

Chapter 10

Summary

Vibrational energy transport is not only relevant in the macroscopic world, but also on the microscopic scale of nanostructures and biomolecules. In this thesis, femtosecond infrared spectroscopy supported by numerical simulations was applied to investigate the transport of vibrational energy transport through peptides and proteins.

In a simulation study that was performed on a simple toy model mimicking the normal mode distribution of proteins, the flow of vibrational energy through a one-dimensional biomolecular chain was investigated. It was demonstrated that vibrational energy transport on length scales of a few chemical bonds and time scales of a few picoseconds is distinctively different from heat diffusion on macroscopic scales. The reason is that vibrational energy does not necessarily thermalize completely within individual amino acid sites and energy transport is mainly governed by intrasite IVR. Surprisingly though, all IVR-related effects are completely hidden when averaging the energy content of individual amino acid sites over all their vibrational modes. These findings provide the key to understanding several experimental observations, and also explain the deviating results of accompanying MD simulations [43, 51, 52].

Motivated by the results of the simulation study, a new experiment was designed aiming to measure the vibrational energy transport properties of a peptide helix after low-energy IR excitation. For this purpose, fully deuterated leucine was introduced as an alternative local heater, releasing a low amount of excess energy by vibrational relaxation of its side-chain C−D modes. Vibrational energy propagation after excitation of the C−D modes can be described as a diffusion-like process. The measured heat diffusion constant of $\approx 2\ \text{Å}^2\text{ps}^{-1}$ is in agreement with the result obtained by Botan *et al.* after UV excitation of an azobenzene chromophore [43], showing that the energy transport properties of biomolecular chains do not depend on how and how much energy is initially deposited. From a practical point of view, the fact that the linearity of vibrational energy diffusion is maintained over a wide range of initial temperature gradients is good news. It means that vibrational energy transport properties can be studied equally well after the deposition of high amounts of excess energy, which is advantageous because larger signals can be observed over longer distances. This opens the possibility to develop new efficient heaters, which will be necessary to extend vibrational energy transport studies to proteins.

Following this line of thought, plasmonically heated gold nanoparticles were introduced as a novel local heater for initiating vibrational energy transport through attached biomolecules. Due to their large optical cross section and low quantum yield, metal nanoparticles are extremely efficient photothermal converters [102]. The properties of this new heating mechanism were explored in an experiment, in which small spherical gold nanoparticles were completely covered by a capping layer of helical peptides. Upon plasmonic heating, vibrational energy propagates through the capping layer in a diffusive manner, as indicated by the sequential response of C=O reporter groups in the peptide backbone and the exponential kinetics. This experiment, at the same time, demonstrates a new method for measuring the rates and efficiencies of heat flow across organic capping layers over metal nanoparticles, giving important information relevant for many plasmonic applications such as optically activated drug delivery. In contrast to the previous experiment, where energy transport was studied along individual helical chains, the peptides in this experiment are arranged in an ordered three-dimensional structure around the heat source. The geometry and packing efficiency of this capping layer influence the dissipation of vibrational energy into the solvent; due to the increased solvent penetration, capping layers applied to small nanoparticles cool faster.

Having now different local heaters at hand, the next step is to move from exploring vibrational energy transport in small model peptides to a protein that folds into a three-dimensional, tertiary structure. For this purpose, the 36-residue villin headpiece protein was chosen as a model system. In a preparatory study, it was successfully demonstrated how cysteine-containing villin headpiece 36 mutants can be coupled to two very different, thiol-reactive local heater units – a specifically-designed electronically excited azobenzene chromophore, and a small plasmonically heated gold nanoparticle. Both local heating mechanisms were triggered with laser pulses in the UV spectral range; the measured time-resolved IR spectra show a blueshift of the protein amide I band, indicating that laser excitation generates an ultrafast temperature jump, which destabilizes the hydrogen bonds of the protein. The difficulty encountered in these experiments was that no site-selective information could be obtained, because the used $^{13}C{=}^{18}O$ isotope labels were overlapped by absorbance from multiple amino acid side chains. Therefore, to explore the use of alternative residue specific labels, the azido-bearing nonnatural amino acid azidohomoalanine [168] was incorporated into the HP36 sequence, where it could be identified in a nonambiguous manner. However, since the detection of a single molecular group in a larger protein is challenging, an experimental setup with improved detectivity will be required, which is currently under construction.

With the results presented in this thesis it is finally possible to answer all three questions raised in Chapter 1:

- Why is the experimentally measured thermal diffusivity so low?

  On the given ultrashort length and time scales, IVR rather than the actual transport along the chain is the rate-limiting step, which significantly slows down the observed energy propagation speed. The initial transport of nonthermalized vibrational energy can be described by a decreased apparent heat diffusion constant. On longer time scales, when vibrational energy has relaxed to an equilibrium Boltzmann distribution, heat transport can be described by the familiar bulk properties. The reason why accompanying MD simulations could not reproduce this effect, is that the experimentally measured observable, which is the transient redshift of a localized C=O group, does not reflect the overall residue energy, which was the basis for all MD simulations. Based on this idea, Stock and coworkers modified their MD simulations and calculated the energy content of the C=O modes instead of the total residue energy, which lead to an improved agreement with the experimental results [78].

- Does the thermal diffusivity depend on how and how much energy is deposited?

  The energy transport properties of biomolecular chains are largely insensitive to the amount of initially deposited energy. The simulation studies of vibrational energy transport along a molecular chain do not show any excitation energy dependence of the thermal properties. Also the experiments employing several distinctively different local heating mechanisms reveal very similar energy transport properties, showing that the energy transport hardly depends on the type of initial excitation. From this it can be concluded that vibrational energy transport is not mode-specific, and hence, vibrational energy must be largely randomized after either of the heating processes. The fourfold faster energy transport observed by Backus *et al.* [51] after IR pumping of a localized peptide C=O modes can be attributed to a special case of resonant energy transfer directly along the C=O oscillators. This interpretation is also supported by a recent paper by Stock and coworkers [101], who performed nonequilibrium MD simulations of the experimentally studied peptide helix, showing that resonant excitation of a localized C=O oscillator initiates coherent energy transport along the C=O modes, with an amplitude and speed much higher than for energy transfer via the backbone.

- Why does heat transport change from diffusive to ballistic at low temperatures, and at the same time becomes less efficient?

  The devised toy model intuitively demonstrates how controlling the rate of intrasite IVR can switch vibrational energy transport from ballistic but inefficient to diffusive and efficient. When IVR is suppressed, only the small fraction of energy that is already contained in the delocalized low-frequency modes can propagate, which happens ballistically, but the overall amount of transferred energy is decreased. Efficient intrasite IVR, in contrast, opens the channel for energy flow out of and back into the localized high-frequency modes, thus distributing vibrational energy efficiently over the entire biomolecule. Since the IVR dependence is completely hidden when averaging over all vibrational modes of individual amino acid residues, this effect could not be reproduced by the original MD simulations [52]. However, the modified MD simulations by Stock and coworkers, extracting the transport properties from the C=O energies, can also reproduce this experimentally measured temperature dependence [78].

In summary, the experimental and theoretical studies presented in this thesis have contributed to a better understanding of vibrational energy transport in biomolecular chains. Several open questions and apparent contradictions have successfully been resolved, leading to a unified picture of the topic. Finally, the first experiments on vibrational energy transport in a small protein provide a guideline for how to extend the underlying experimental concepts to more complex molecular structures.

Appendix A

Derivation of Hamiltonian in terms of ladder operators

For the quantum-mechanical simulations, the creation and annihilation operators

$$
\begin{aligned}
b_{ij} &= \frac{1}{\sqrt{2}}(\hat{q}_{ij} + i\hat{p}_{ij}) \\
b_{ij}^{\dagger} &= \frac{1}{\sqrt{2}}(\hat{q}_{ij} - i\hat{p}_{ij})
\end{aligned}
\tag{A.1}
$$

with the commutator

$$
[b_{ij}, b_{ij}^{\dagger}] = 1 \tag{A.2}
$$

are used to express the position ($\hat{q}$) and momentum ($\hat{p}$) coordinates:

$$
\begin{aligned}
\hat{q}_{ij} &= \frac{1}{\sqrt{2}}(b_{ij}^{\dagger} + b_{ij}) \\
\hat{p}_{ij} &= \frac{i}{\sqrt{2}}(b_{ij}^{\dagger} - b_{ij})
\end{aligned}
\tag{A.3}
$$

With this, the Hamiltonian from Eq. (3.6) transforms as follows. The harmonic part $H^{(2)}$ (Eq. (3.2)) can be rewritten as:

$$
\begin{aligned}
H^{(2)} &= \frac{1}{2}\sum_{i,j}\omega'_{ij}\left(p_{ij}^2 + q_{ij}^2\right) - \sum_{i=1}^{n-1} k_i q_{i,1} q_{i+1,1} \\
&= \frac{1}{2}\sum_{i,j}\omega'_{ij}\left(\left(\frac{i}{\sqrt{2}}(b_{ij}^{\dagger} - b_{ij})\right)^2 + \left(\frac{1}{\sqrt{2}}(b_{ij}^{\dagger} + b_{ij})\right)^2\right) \\
&\qquad - \sum_{i=1}^{n-1} k_i \frac{1}{\sqrt{2}}(b_{i,1}^{\dagger} + b_{i,1}) \frac{1}{\sqrt{2}}(b_{i+1,1}^{\dagger} + b_{i+1,1}) \\
&= \frac{1}{4}\sum_{i,j}\omega'_{ij}\left(-(b_{ij}^{\dagger} - b_{ij})^2 + (b_{ij}^{\dagger} + b_{ij})^2\right) - \frac{1}{2}\sum_{i=1}^{n-1} k_i (b_{i,1}^{\dagger} + b_{i,1})(b_{i+1,1}^{\dagger} + b_{i+1,1})
\end{aligned}
$$

$$\begin{aligned}
&= \frac{1}{2}\sum_{i,j}\omega'_{ij}\left(b^\dagger_{ij}b_{ij} + b_{ij}b^\dagger_{ij}\right) - \frac{1}{2}\sum_{i=1}^{n-1}k_i\left(b^\dagger_{i,1}b^\dagger_{i+1,1} + b^\dagger_{i,1}b_{i+1,1} + c.c\right) \\
&= \sum_{i,j}\omega'_{ij}\left(b^\dagger_{ij}b_{ij} + \frac{1}{2}\right) - \frac{1}{2}\sum_{i=1}^{n-1}k_i\left(b^\dagger_{i,1}b^\dagger_{i+1,1} + b^\dagger_{i,1}b_{i+1,1} + c.c\right)
\end{aligned} \tag{A.4}$$

For the anharmonic part $H^{(3)}$ (Eq. (3.5)) follows:

$$\begin{aligned}
H^{(3)} &= \Delta\sum_{i,j,k}q_{ik}q_{ij}^2 \\
&= \Delta\sum_{i,j,k}\frac{1}{\sqrt{2}}(b^\dagger_{ik} + b_{ik})\left(\frac{1}{\sqrt{2}}(b^\dagger_{ij} + b_{ij})\right)^2 \\
&= \Delta\frac{1}{\sqrt{8}}\sum_{i,j,k}(b^\dagger_{ik} + b_{ik})(b^\dagger_{ij} + b_{ij})(b^\dagger_{ij} + b_{ij}) \\
&= \Delta\frac{1}{\sqrt{8}}\sum_{i,j,k}\left(b^\dagger_{ik}b^\dagger_{ij}b^\dagger_{ij} + b^\dagger_{ik}b^\dagger_{ij}b_{ij} + b^\dagger_{ik}b_{ij}b^\dagger_{ij} + b^\dagger_{ik}b_{ij}b_{ij}\right) + c.c.
\end{aligned} \tag{A.5}$$

Appendix B

Mean square displacement in diffusive processes

It can be shown that for all processes that can be described by a diffusion equation the mean square displacement $\langle x^2 \rangle$ is proportional to the time t. For the one-dimensional case the proportionality constant is $2D$ (adapted from Ref. [171]):

Starting from the one-dimensional diffusion equation (compare Eq. (2.4))

$$\frac{\partial \rho(x,t)}{\partial t} = D \frac{\partial^2 \rho(x,t)}{\partial x^2} \tag{B.1}$$

the time dependence of the mean square displacement can be obtained by multiplying both sides with x^2 and integrating over x:

$$\begin{aligned} \int\limits_{-\infty}^{\infty} x^2 \frac{\partial \rho(x,t)}{\partial t} dx &= \int\limits_{-\infty}^{\infty} D x^2 \frac{\partial^2 \rho(x,t)}{\partial x^2} dx \\ \frac{\partial}{\partial t} \int\limits_{-\infty}^{\infty} x^2 \rho(x,t) dx &= D \int\limits_{-\infty}^{\infty} x^2 \frac{\partial^2 \rho(x,t)}{\partial x^2} dx \end{aligned} \tag{B.2}$$

With the definition of the mean square displacement

$$\langle x^2 \rangle = \frac{\int_{-\infty}^{\infty} x^2 \rho(x,t) dx}{\int_{-\infty}^{\infty} \rho(x,t) dx} = \frac{1}{N} \int\limits_{-\infty}^{\infty} x^2 \rho(x,t) dx \tag{B.3}$$

the left hand side can be simplified to

$$\frac{\partial}{\partial t} \int\limits_{-\infty}^{\infty} x^2 \rho(x,t) dx = N \frac{\partial \langle x^2 \rangle}{\partial t}. \tag{B.4}$$

Twofold integration by parts on the right hand side yields:

$$\begin{aligned} D\int_{-\infty}^{\infty} x^2\rho''(x,t)dx &= D\left([x^2\rho'(x,t)]_{-\infty}^{\infty} - 2\int_{-\infty}^{\infty} x\rho'(x,t)dx\right) \\ &= D\left(\underbrace{[x^2\rho'(x,t)]_{-\infty}^{\infty}}_{0} -2\underbrace{[x\rho(x,t)]_{-\infty}^{\infty}}_{0} +2\underbrace{\int_{-\infty}^{\infty}\rho(x,t)dx}_{N}\right) \\ &= 2DN \end{aligned} \tag{B.5}$$

Then follows with Eqns. (B.4) and (B.5)

$$N\frac{\partial\langle x^2\rangle}{\partial t} = 2DN \tag{B.6}$$

or after integration:

$$\langle x^2\rangle = 2Dt \tag{B.7}$$

For two- or three-dimensional diffusion processes the corresponding proportionality constants are $4D$ and $6D$, respectively.

Appendix C

Diffusive rate model for vibrational energy flow between discrete microstates

Part 1

Figure C.1 shows a system of n site-localized states which can exchange vibrational energy at equal forward and backward rates. The treatment of the dynamics of such a system is discussed in detail in Ref. [172]. The system can be described by a rate equation

$$\frac{d\vec{\epsilon}(t)}{dt} = K\vec{\epsilon}(t) \tag{C.1}$$

with the vector $\vec{\epsilon}(t)$ containing the time-dependent energies of the states and the matrix K containing the rate constants k for energy transfer between them. For a system of n states K is an $n \times n$ matrix.

To solve this system of coupled differential equations the matrix K can be diagonalized using a transformation matrix $Q = (q_1, q_2, ..., q_n)$ consisting of the eigenvectors of K. The resulting diagonal matrix

$$\Lambda = QKQ^{-1} = \mathrm{diag}(\lambda_1, \lambda_2, ..., \lambda_n) \tag{C.2}$$

contains the corresponding eigenvalues λ_i of K on its main diagonal ($\lambda_i \leq 0$). Then, the solution of the differential equation Eq. (C.1)

$$\vec{\epsilon}(t) = e^{Kt}\vec{\epsilon}(0) \tag{C.3}$$

can be rewritten as

$$\begin{aligned} \vec{\epsilon}(t) &= e^{Q^{-1}\Lambda Q t}\vec{\epsilon}(0) \\ &= Q^{-1}e^{\Lambda t}Q\vec{\epsilon}(0) \\ &= Q^{-1}\mathrm{diag}(e^{\lambda_1 t}, e^{\lambda_2 t}, ..., e^{\lambda_n t})Q\vec{\epsilon}(0). \end{aligned} \tag{C.4}$$

The resulting solutions are multiexponential functions with n time constants $\tau_i = 1/\lambda_i$.

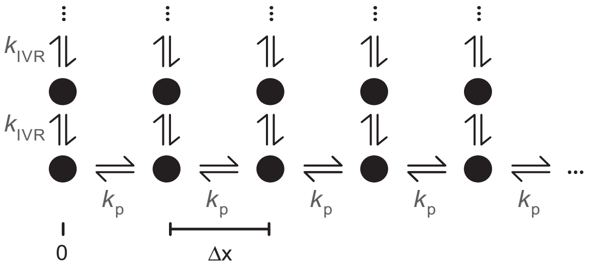

Figure C.1: System of n site-localized states at distance Δx which can exchange vibrational energy at equal forward and backward propagation rates k.

Part 2

First, only energy transport along the x-direction of the linear is considered, occurring at a propagation rate k_{p}. In this case, because of the one-dimensional connectivity, the matrix $K^{(\mathrm{p})}$ adopts the following tri-diagonal form:

$$K^{(\mathrm{p})} = \begin{pmatrix} -k_{\mathrm{p}} & k_{\mathrm{p}} & 0 & 0 & 0 & \cdots \\ k_{\mathrm{p}} & -2k_{\mathrm{p}} & k_{\mathrm{p}} & 0 & 0 & \cdots \\ 0 & k_{\mathrm{p}} & -2k_{\mathrm{p}} & k_{\mathrm{p}} & 0 & \cdots \\ 0 & 0 & k_{\mathrm{p}} & -2k_{\mathrm{p}} & k_{\mathrm{p}} & \cdots \\ \vdots & \vdots & \vdots & \vdots & \vdots & \ddots \end{pmatrix} \tag{C.5}$$

Due to the form of the matrix $K^{(\mathrm{p})}$, which in fact just contains discrete second x-derivatives, the rate equation system (Eq. (C.1)) can be rewritten as follows:

$$\begin{aligned} \frac{d\vec{\epsilon}(t)}{dt} &= K^{(\mathrm{p})}\vec{\epsilon}(t) \\ &= k_{\mathrm{p}} \begin{pmatrix} \ddots & \vdots & \vdots & \vdots & \\ \cdots & -2 & 1 & 0 & \cdots \\ \cdots & 1 & -2 & 1 & \cdots \\ \cdots & 0 & 1 & -2 & \cdots \\ & \vdots & \vdots & \vdots & \ddots \end{pmatrix} \begin{pmatrix} \vdots \\ \epsilon_{x-1} \\ \epsilon_x \\ \epsilon_{x+1} \\ \vdots \end{pmatrix} \\ &= D \begin{pmatrix} \vdots \\ (\epsilon_{x-1} - 2\epsilon_x + \epsilon_{x+1})/\Delta x^2 \\ \vdots \end{pmatrix} \\ &= D\,\frac{\Delta^2\vec{\epsilon}}{\Delta x^2} \end{aligned} \tag{C.6}$$

Hence, the deduced rate model for describing the flow of vibrational energy along a linear chain of discrete microstates can be viewed as a discretized version of the heat diffusion equation (Eq. (2.4)), in which the diffusion constant D and the propagation rate k_{p} are linked by

$$D = k_{\mathrm{p}}\Delta x^2. \tag{C.7}$$

Consequently, the solutions to Eq. (C.1) are diffusive-like functions, which again fulfill the criterion $\langle x^2 \rangle = 2Dt$.

Part 3

As a next step, also IVR within the modes j of the sites i is considered. Then, the connectivity matrix K adopts the following form:

$$K = K^{(\mathrm{p})} + K^{(\mathrm{IVR})}, \tag{C.8}$$

where $K^{(\mathrm{p})}$ is the previously defined matrix describing propagation along the linear chain (Eq. (C.5)) and $K^{(\mathrm{IVR})}$ is the relaxation matrix within each site, which is assumed to be the same for all sites. Apart from the assumption that the relaxation matrix is energy conserving, i.e. $\sum_j K_{jl}^{(\mathrm{IVR})} = 0$ for all l, it can have any arbitrary form, which is potentially more complicated as the one indicated in Figure C.1, i.e. any number of modes, branches, etc. Then, the rate equation (Eq. (C.1)) can be written as

$$\frac{d\epsilon_{i,j}}{dt} = \delta_{j,1}\left(k_\mathrm{p}\epsilon_{i-1,1} - 2k_\mathrm{p}\epsilon_{i,1} + k_\mathrm{p}\epsilon_{i+1,1}\right) + \sum_l K_{jl}^{(\mathrm{IVR})}\epsilon_{i,l}, \tag{C.9}$$

where $\epsilon_{i,j}$ is the vibrational energy in mode j of site i.

Now, calculating $\sum_i \epsilon_{i,j}$ over Eq. (C.9) one obtains:

$$\frac{d\sum_i \epsilon_{i,j}}{dt} = \sum_i \delta_{j,1}\left(k_\mathrm{p}\epsilon_{i-1,1} - 2k_\mathrm{p}\epsilon_{i,1} + k_\mathrm{p}\epsilon_{i+1,1}\right) + \sum_l K_{jl}^{(\mathrm{IVR})}\left(\sum_i \epsilon_{i,l}\right) \tag{C.10}$$

The first term of Eq. (C.10) cancels because of energy conservation. In the following, it is assumed that the prepared initial condition $\epsilon_{i,j}(t=0)$ is an equilibrium state of each site, but not necessarily an equilibrium state of the chain as a whole. That is, the temperature at one site might be elevated as compared to the other sites, but the energy is equilibrated within that one site. In other words, $\epsilon_{i,l}$ of each site i is an eigenvector of the matrix $K_{jl}^{(\mathrm{IVR})}$ with eigenvalue 0. As such, also $\sum_i \epsilon_{i,l}$ is an eigenvector, and therefore also the second term of Eq. (C.10) is zero. Hence, it is shown that

$$\frac{d\sum_i \epsilon_{i,j}}{dt} = 0 \Rightarrow \sum_i \epsilon_{i,j}(t) = \text{const.} = \sum_i \epsilon_{i,j}(t=0). \tag{C.11}$$

On the other hand, calculating $\sum_j \epsilon_{i,j}$ over Eq. (C.9) leads to

$$\sum_j \frac{d\epsilon_{i,j}}{dt} = k_\mathrm{p}\epsilon_{i-1,1} - 2k_\mathrm{p}\epsilon_{i,1} + k_\mathrm{p}\epsilon_{i+1,1}, \tag{C.12}$$

where the second term disappears again because of energy conservation.

The aim is now to calculate the mean square displacement of this system. As a demonstration, this step is first performed for the simple linear chain, whose kinetic equation is already known from Eq. (C.6) in Part 2 of this appendix:

$$\frac{d\epsilon_i}{dt} = k_\mathrm{p}\epsilon_{i-1} - 2k_\mathrm{p}\epsilon_i + k_\mathrm{p}\epsilon_{i+1} \tag{C.13}$$

Under the assumption that the initial excitation is at site 0 with $\epsilon_0 = 1$, and all other sites are not populated at $t = 0$, i.e. $\epsilon_i = 0$ for $i \neq 0$, the mean square displacement is given by:

$$\langle x^2 \rangle = \Delta x^2 \sum_i i^2 \epsilon_i \tag{C.14}$$

Then, the temporal change of this quantity can be calculated as:

$$\begin{aligned}\frac{d}{dt}\langle x^2\rangle &= \Delta x^2 \sum_i i^2 \frac{d}{dt}\epsilon_i \\ &= k_\mathrm{p}\Delta x^2 \sum_i i^2 \left(\epsilon_{i-1} - 2\epsilon_i + \epsilon_{i+1}\right) \qquad \text{(C.15)}\end{aligned}$$

Resorting the terms on the rhs., and utilizing energy conservation $\sum \epsilon_i = 1$, this expression simplifies to:

$$\frac{d}{dt}\langle x^2\rangle = 2k_\mathrm{p}\Delta x^2 \sum_i \epsilon_i = 2k_\mathrm{p}\Delta x^2 \qquad \text{(C.16)}$$

Finally, one obtains

$$\langle x^2\rangle = 2k_\mathrm{p}\Delta x^2 t \qquad \text{(C.17)}$$

That is, the process is diffusive with a diffusion constant $D = k_\mathrm{p}\Delta x^2$, which had already been shown in Eq. (C.7).

Along the same lines as for the simple linear chain the mean square displacement is now calculated for the full system including IVR. Again, it is assumed that initially only site 0 is populated, i.e. $\sum_j \epsilon_{0,j} = 1$, while all other sites are not populated, $\epsilon_{i,j} = 0$ for $i \neq 0$. The mean square displacement of the total energy summed over all modes j of a site, $\epsilon_i^{(\mathrm{tot})} = \sum_j \epsilon_{i,j}$, is given as:

$$\langle x^2\rangle = \Delta x^2 \sum_{i,j} i^2 \epsilon_{i,j} \qquad \text{(C.18)}$$

Plugging Eq. (C.12) into this expression and performing the same steps as before leads to:

$$\frac{d}{dt}\langle x^2\rangle = 2k_\mathrm{p}\Delta x^2 \sum_i \epsilon_{i,1} = 2k'_\mathrm{p}\Delta x^2 \qquad \text{(C.19)}$$

or

$$\langle x^2\rangle = 2k'_\mathrm{p}\Delta x^2 t \qquad \text{(C.20)}$$

Here, it was made use of Eq. (C.11), i.e. $\sum_i \epsilon_{i,1} = \text{const.} = \sum_i \epsilon_{i,1}(t=0)$. The effective propagation rate, and hence also the effective diffusion constant, is reduced by the relative energy of the transporting mode, which is proportional to the relative heat capacity:

$$k'_\mathrm{p} = \epsilon_{0,1}(t=0)k_\mathrm{p} \qquad \text{(C.21)}$$

This result only holds if the initial condition $\epsilon_{0,j}(t=0)$ is assumed to be equilibrated within site 0, so that Eq. (C.11) is true. In summary, when the total energy $\epsilon_i^{(\mathrm{tot})}$ is measured, a diffusive process on a simple 1D chain with some effective propagation rate k'_p is observed. All the complexity of the IVR process within the sites, which actually is rate-limiting on short length and time scales, is completely hidden.

Note that Eq. (C.20) does not imply that Eq. (C.12) can be reduced to a true 1D chain with an effective propagation rate k'_p:

$$\frac{d\epsilon_i^{(\mathrm{tot})}}{dt} = k'_\mathrm{p}\epsilon_{i-1}^{(\mathrm{tot})} - 2k'_\mathrm{p}\epsilon_i^{(\mathrm{tot})} + k'_\mathrm{p}\epsilon_i^{(\mathrm{tot})} \qquad \text{(C.22)}$$

This means that although the mean square displacement predicted by Eqs. (C.12) and (C.20) shows the same time dependence, the energies of the individual sites do not. Nevertheless, the differences between Eqs. (C.12) and (C.20) are small, in particular for sites not too close to the heating site, and might not be measurable in a real experiment.

Appendix D

Synthesis of water-soluble azobenzene and linking to a thiol-containing protein[†]

Azobenzene-based chromophores are extremely stable photoswitches that can be switched reversibly between their *cis*- and *trans*-states by choosing particular wavelengths of the light spectrum. Typically, isomerization can be triggered at wavelengths higher than 300 nm so that the irradiated light is not absorbed by biomolecules. The photoinduced *cis-trans* isomerization occurs on an ultrafast time scale (<1 ps) and exhibits a high quantum yield ($>50\%$) [143]. When synthesized with two thiol-reactive groups, azobenzene can cross-link two cysteine-residues in a protein and thus be used as a conformational photoswitch [173, 174]. Azobenzene chromophores with only one thiol-reactive group can be linked to a cysteine-containing protein in a single-sided manner and act as an ultrafast local heater injecting vibrational excess energy on a time scale determined by the photoinduced *cis-trans* isomerization [43].

The classical azobenzene photoswitch suffers from its poor water-solubility, which necessitates an organic cosolvent for linking reactions and also may lead to the aggregation of azobenzene-linked proteins in aqueous solution. Woolley and coworkers proposed a water-soluble variant of the original cross-linking reagent; by adding sulfonate groups to the azobenzene ring system, water-solubility can be achieved without altering the photochemical properties [159, 160]. Based on this design, a similar sulfonated azobenzene derivative for single-sided protein linking, 4-Chloroacetamido-azobenzene-3,4'-disulfonic acid (Acid yellow chloracetyl, AYC) was developed, the synthesis of which is described in detail below.

In a 100 ml round-bottom flask containing a magnetic stir bar, 2.33 g (20 mmol) sodium chloroacetate and 12 g (≈120 mmol) chloroacetic acid were heated to about 90°C in an oil bath. Note that the addition of sodium chloroacetate is crucial for the synthesis but not described in Refs. [159, 160]! 1.9 g (5 mmol) 4-Amino-azobenzene-3,4'-disulfonic acid sodium salt (Acid yellow 9, Sigma Aldrich) were added and the solution stirred for some minutes. Subsequently, 4.1 g (24 mmol, i.e. ≈5-fold molar excess) chloroacetic anhydride were added and stirring was continued. After approximately 1 h the mixture was diluted

---

[†] The synthetic part was contributed by Rolf Pfister.

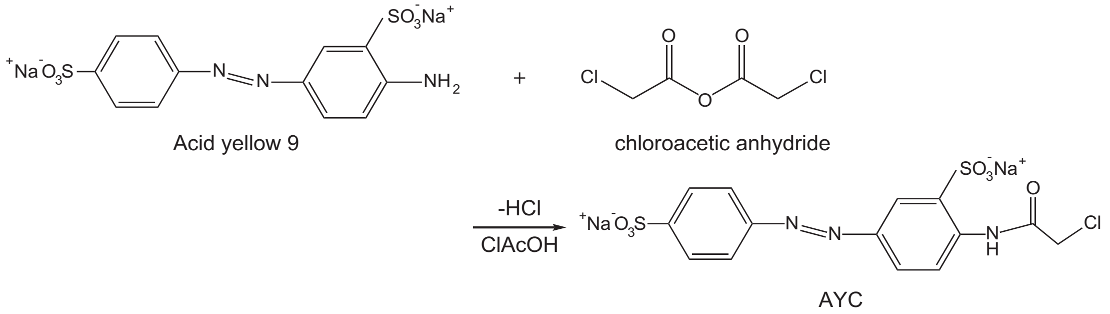

Figure D.1: Reaction scheme for the synthesis of the water-soluble azobenzene photoswitch 4-Chloroacetamido-azobenzene-3,4'-disulfonic acid (AYC).

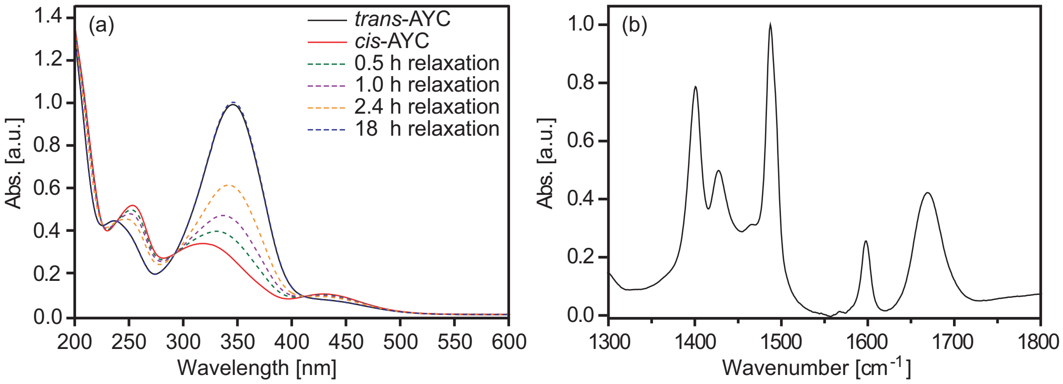

Figure D.2: (a) UV/vis spectra of AYC dissolved in H_2O, recorded in the dark-adapted *trans*-state (black, solid line) and after switching into the *cis*-state by UV-irradiation at 375 nm (red, solid line). The spectra plotted in dashed were recorded after switching off the UV-LED and illustrate the thermal relaxation back into the initial *trans*-state. (b) FTIR spectrum of AYC recorded D_2O showing the ring mode absorption bands at 1595 cm^{-1} and 1670 cm^{-1} that overlap the protein amide I absorption.

with additional 11 g chloroacetic acid and the resulting solution was stirred overnight at 90-95°C. Upon cooling, 25 ml dichloromethane were added, the obtained solution was filtered with a G3 suction strainer and washed with dichloromethane and then ether. For further purification the product was recrystallized in a water/ethanol mixture, removing a minor impurity (54 mg, 2.5%) of 4-Chloroacetamido-azobenzene-4'-disulfonic acid (i.e., the desired final product but with only one benzene ring sulfonated). Finally, the solution was heated to 40°C and ether was added until the solution became turbid and then biphasic. The formed aqueous phase was evaporated under high vacuum to give 1.72 g (80%) of the desired final product 4-Chloroacetamido-azobenzene-3,4'-disulfonic acid (reaction scheme Fig. D.1).

The UV/Vis and FTIR spectra of the obtained sulfonated azobenzene dissolved in H_2O and D_2O, respectively, are shown in Figure D.2. To analyze the photoisomerization of AYC the sample was irradiated for 1 minute with an LED emitting UV-light at a central wavelength of 375 nm and a power of 230 mW, which switches the sample from its *trans*- into the *cis*-state. Upon irradiation, the strong absorption maximum around 350 nm, which belongs to the $\pi\pi^*$ transition of *trans*-azobenzene loses intensity, while the

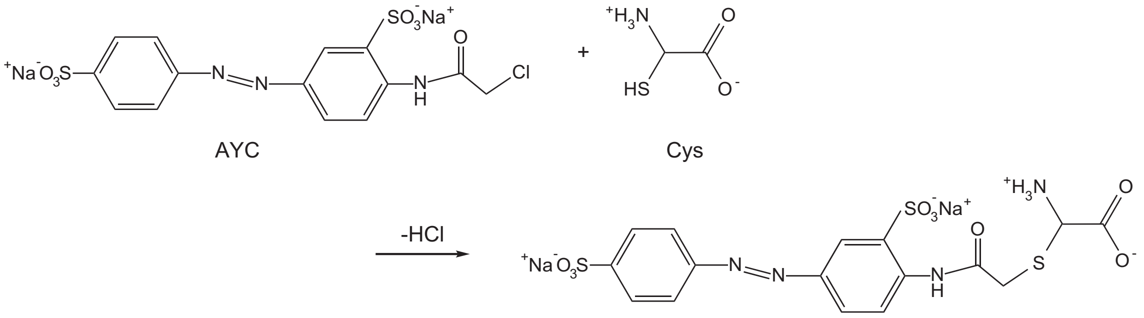

Figure D.3: Reaction scheme for the linking between AYC and a cysteine-containing protein.

absorption around 435 nm, corresponding to the nπ^* transition of *cis*-azobenzene, slightly increases, very similar to the spectra shown in [160]. To monitor the thermal relaxation back into the dark-adapted *trans*-state, further UV/Vis spectra were recorded over the following hours, showing that the photoisomerization is fully reversible. The FTIR spectrum of the AYC photoswitch shows the ring mode absorptions at 1595 cm^{-1} and 1670 cm^{-1} that could also be observed in the UV pump/IR probe spectra on the azobenzene-linked HP36 proteins (compare Figure 9.6a).

For coupling the thiol-reactive group of the AYC photoswitch to the solvent-exposed thiol side chain of Cys56 in villin headpiece 36, 5.1 mg (1.2 μmol) of the protein were dissolved in 2 ml, 10 mM Tris buffer (Tris/EDTA pH 8.0 or Tris/HCl pH 8.5). Then, 1.8 mg (4 μmol, i.e. 3.4-fold molar excess) AYC were dissolved in 0.2 ml H_2O and added dropwise to the protein solution. The obtained solution was incubated at room temperature overnight, filtered through a 0.45 μm PTFE filter and finally purified by 4 HPLC runs (reaction scheme Fig. D.3). As an alternative method, the proteins can be purified and concentrated by ultrafiltration (3 kDa molecular weight cutoff filter), which is especially suitable for Aha-labeled proteins whose azide groups possibly react under HPLC conditions.

As an undesirable side-reaction, disulfide bond formation between cysteine residues can block the thiol groups, thus preventing efficient linking to the azobenzene. In this case, Tris-(2-carboxyethyl) phosphine hydrochloride (TCEP) should be used as a reducing agent and buffered accordingly to maintain the correct pH for the linking reaction as described in Ref. [160].

If a protein is prone to aggregate under the conditions of the linking reaction, linking should be performed at low protein and high denaturant concentration. After successful linking, first, the denaturant concentration must be decreased to refold the proteins (e.g., by transferring the protein solution into a high volume of a suitable buffer) and then the solution of folded proteins can be concentrated. It is well-established that in the presence of heat a carbamylation reaction between urea and the proteins can occur, which can easily be identified by an increase of 43 mass units relative to original protein (a detailed discussion can be found in Ref. [175]). To avoid this unwanted effect, guanidinium chloride should be used as a denaturant during the linking reaction.

List of abbreviations

Aha	azidohomoalanine
Aib	α-aminoisobutyric acid
AYC	acid yellow chloracetyl (4-Chloroacetamido-azobenzene-3,4'-disulfonic acid)
BBO	β-barium borate (β-BaB_2O_4)
CD	circular dichroism (not to confuse with $C{-}D$, which is carbon-deuterium)
CPA	chirped pulse amplification
CW	continuous wave
DFG	difference-frequency generation
DMSO	dimethyl sulfoxide ($(CH_3)_2SO$)
EDTA	ethylenediaminetetraacetic acid
Fmoc	fluorenylmethyloxycarbonyl
FTIR	Fourier transform infrared
FWHM	full width at half maximum
HP36	villin headpiece protein subdomain with 36 amino acid residues
HPLC	high-performance liquid chromatography
IR	infrared
IVR	intramolecular vibrational energy redistribution
LED	light-emitting diode
Leu-d_{10}	fully deuterated leucine
MD	molecular dynamics
NMR	nuclear magnetic resonance
NOPA	noncollinear optical parametric amplifier
OPA	optical parametric amplifier
PEG	polyethylene glycol
PTFE	polytetrafluorethylen, also known under the brand name Teflon
SHG	second-harmonic generation
TCEP	tris-(2-carboxyethyl) phosphine hydrochloride
TEM	transmission electron microscopy
TFA	trifluoro acetic acid (CF_3CO_2H)
Ti:sapphire	titanium:sapphire (titanium-doped Al_2O_3)
Tris	tris(hydroxymethyl)aminomethane ($(HOCH_2)_3CNH_2$)
UV	ultraviolet
Vis	visible

Bibliography

[1] D. M. Leitner.
Vibrational energy transfer in helices.
Phys. Rev. Lett. **87**, 188102 (2001).

[2] H. Fujisaki and J. E. Straub.
Vibrational energy relaxation in proteins.
Proc. Natl. Acad. Sci. USA **102**, 6726–6731 (2005).

[3] A. S. Davydov.
Solitons in molecular systems.
Phys. Scr. **20**, 387–394 (1979).

[4] J. Edler, R. Pfister, V. Pouthier, C. Falvo, and P. Hamm.
Direct observation of self-trapped vibrational states in alpha-helices.
Phys. Rev. Lett. **93**, 106405 (2004).

[5] P. Hamm.
Femtosecond IR pump-probe spectroscopy of nonlinear energy localization in protein models and model proteins.
J. Biol. Phys. **35**, 17–30 (2009).

[6] D. M. Leitner.
Energy flow in proteins.
Annu. Rev. Phys. Chem. **59**, 233–259 (2008).

[7] S. W. Lockless and R. Ranganathan.
Evolutionarily conserved pathways of energetic connectivity in protein families.
Science **286**, 295–299 (1999).

[8] N. Ota and D. A. Agard.
Intramolecular signaling pathways revealed by molecular anisotropic thermal diffusion.
J. Mol. Biol. **351**, 345–354 (2005).

[9] K. Sharp and J. J. Skinner.
Pump-probe molecular dynamics as a tool for studying protein motion and long range coupling.
Proteins **65**, 347–361 (2006).

[10] B. F. Volkman, D. Lipson, D. E. Wemmer, and D. Kern.
Two-state allosteric behavior in a single-domain signaling protein.
Science **291**, 2429–2433 (2001).

[11] P. H. Nguyen, P. Hamm, and G. Stock.

Nonequilibrium molecular dynamics simulation of photoinduced energy flow in peptides: theory meets experiment.
In *Proteins: energy, heat and signal flow (computation in chemistry).* D. Leitner, J. Straub (Eds.), Taylor and Francis/CRC Press, London (2009).

[12] P. H. Nguyen, P. Derreumaux, and G. Stock.
Energy flow and long-range correlations in guanine-binding riboswitch: a nonequilibrium molecular dynamics study.
J. Phys. Chem. B **113**, 9340–9347 (2009).

[13] P. Li and P. M. Champion.
Investigations of the thermal response of laser-excited biomolecules.
Biophys. J. **66**, 430–436 (1994).

[14] D. M. Leitner.
Heat transport in molecules and reaction kinetics: the role of quantum energy flow and localization.
In *Geometric structures of phase space in multidimensional chaos: a special volume of Adv. Chem. Phys., Part B, Volume 130.* M. Toda, T Komatsuzaki, T. Konishi, R.S. Berry, and S.A. Rice. (Eds.), John Wiley & Sons, Inc. (2005).

[15] H. Matsuda and K. Ishii.
Localization of normal modes and energy transport in the disordered harmonic chain.
Suppl. Prog. Theor. Phys. **45**, 56–86 (1970).

[16] K. Ishii.
Localization of eigenstates and transport phenomena in the disordered one-dimensional system.
Suppl. Prog. Theor. Phys. **53**, 77–183 (1973).

[17] D. M. Leitner.
Vibrational energy transfer and heat conduction in a one-dimensional glass.
Phys. Rev. B **64**, 094201 (2001).

[18] X. Yu and D. M. Leitner.
Vibrational energy transfer and heat conduction in a protein.
J. Phys. Chem. B **107**, 1698–1707 (2003).

[19] X. Yu and D. M. Leitner.
Heat flow in proteins: computation of thermal transport coefficients.
J. Chem. Phys. **122**, 054902 (2005).

[20] J. Fabian.
Decay of localized vibrational states in glasses: a one-dimensional example.
Phys. Rev. B **55**, R3328–R3331 (1997).

[21] S. Alexander, O. Entin-Wohlman, and R. Orbach.
Phonon-fracton anharmonic interactions: the thermal conductivity of amorphous materials.
Phys. Rev. B **34**, 2726–2734 (1986).

[22] A. Jagannathan, R. Orbach, and O. Entin-Wohlman.
Thermal conductivity of amorphous materials above the plateau.
Phys. Rev. B **39**, 13465–13477 (1989).

[23] E. R. Henry, W. A. Eaton, and R. M. Hochstrasser.
Molecular-dynamics simulations of cooling in laser-excited heme-proteins.
Proc. Natl. Acad. Sci. USA **83**, 8982–8986 (1986).

[24] M. Tesch and K. Schulten.
A simulated cooling process for proteins.
Chem. Phys. Lett. **169**, 97–102 (1990).

[25] K. Moritsugu, O. Miyashita, and A. Kidera.
Vibrational energy transfer in a protein molecule.
Phys. Rev. Lett. **85**, 3970–3973 (2000).

[26] I. Okazaki, Y. Hara, and M. Nagaoka.
On vibrational cooling upon photodissociation of carbonmonoxymyoglobin and its microscopic mechanism from the viewpoint of vibrational modes of heme.
Chem. Phys. Lett. **337**, 151–157 (2001).

[27] D. E. Sagnella and J. E. Straub.
Directed energy "funneling" mechanism for heme cooling following ligand photolysis or direct excitation in solvated carbonmonoxy myoglobin.
J. Phys. Chem. B **105**, 7057–7063 (2001).

[28] P. H. Nguyen and G. Stock.
Nonequilibrium molecular-dynamics study of the vibrational energy relaxation of peptides in water.
J. Chem. Phys. **119**, 11350–11358 (2003).

[29] P. H. Nguyen, R. D. Gorbunov, and G. Stock.
Photoinduced conformational dynamics of a photoswitchable peptide: a nonequilibrium molecular dynamics simulation study.
Biophys. J. **91**, 1224–1234 (2006).

[30] T. Ishikura and T. Yamato.
Energy transfer pathways relevant for long-range intramolecular signaling of photosensory protein revealed by microscopic energy conductivity analysis.
Chem. Phys. Lett. **432**, 533–537 (2006).

[31] Z. Wang, J. A. Carter, A. Lagutchev, Y. K. Koh, N. H. Seong, D. G. Cahill, and D. D. Dlott.
Ultrafast flash thermal conductance of molecular chains.
Science **317**, 787–790 (2007).

[32] D. Schwarzer, P. Kutne, C. Schröder, and J. Troe.
Intramolecular vibrational energy redistribution in bridged azulene-anthracene compounds: ballistic energy transport through molecular chains.
J. Chem. Phys. **121**, 1754–1764 (2004).

[33] Z. Wang, A. Pakoulev, and D. D. Dlott.
Watching vibrational energy transfer in liquids with atomic spatial resolution.
Science **296**, 2201–2203 (2002).

[34] S. R. G. Naraharisetty, V. M. Kasyanenko, J. Zimmermann, M. C. Thielges, F. E. Romesberg, and I. V. Rubtsov.
C-D modes of deuterated side chain of leucine as structural reporters via dual-frequency two-dimensional infrared spectroscopy.

J. Phys. Chem. B **113**, 4940–4946 (2009).

[35] K. Haiser, F. O. Koller, M. Huber, N. Regner, T. E. Schrader, W. J. Schreier, and W. Zinth.
Nitro-phenylalanine: a novel sensor for heat transfer in peptides.
J. Phys. Chem. A **115**, 2169–2175 (2011).

[36] D. Kuciauskas, C. J. Wohl, M. Pouy, A. Nasai, and V. Gulbinas.
Nonlinear optical spectroscopic studies of energy transfer in phospholipid bilayer liposomes embedded with porphyrin sensitizers.
J. Phys. Chem. B **108**, 15376–15384 (2004).

[37] J. C. Deàk, Y. Pang, T. D. Sechler, Z. Wang, and D. D. Dlott.
Vibrational energy transfer across a reverse micelle surfactant layer.
J. Phys. Chem. B **306**, 473–476 (2004).

[38] R. J. D. Miller.
Vibrational energy relaxation and structural dynamics of heme proteins.
Annu. Rev. Phys. Chem. **42**, 581–614 (1991).

[39] T. Lian, B. Locke, Y. Kholodenko, and R. M. Hochstrasser.
Energy flow from solute to solvent probed by femtosecond IR spectroscopy: malachite green and heme protein solutions.
J. Phys. Chem. **98**, 11648–11656 (1994).

[40] Y. Mizutani and T. Kitagawa.
Direct observation of cooling of heme upon photodissociation of carbonmonoxy myoglobin.
Science **278**, 443–446 (1997).

[41] J. Deàk, H. L. Chin, C. M. Lewis, and R. J. D. Miller.
Ultrafast phase grating studies of heme proteins: observation of the low-frequency modes directing functionally important protein motions.
J. Phys. Chem. B **102**, 6621–6634 (1998).

[42] Y. Gao, M. Koyama, S. F. El-Mashtoly, T. Hayashi, K. Harada, Y. Mizutani, and T. Kitagawa.
Time-resolved Raman evidence for energy "funneling" through propionate side chains in heme "cooling" upon photolysis of carbonmonoxy myoglobin.
Chem. Phys. Lett. **429**, 239–243 (2006).

[43] V. Botan, E. H. G. Backus, R. Pfister, A. Moretto, M. Crisma, C. Toniolo, P. H. Nguyen, G. Stock, and P. Hamm.
Energy transport in peptide helices.
Proc. Natl. Acad. Sci. USA **104**, 12749–12754 (2007).

[44] C. Toniolo, M. Crisma, F. Formaggio, and C. Peggion.
Control of peptide conformation by the Thorpe-Ingold effect (c-alpha-tetrasubstitution).
Biopolymers **60**, 396–419 (2001).

[45] C. Toniolo, G. M. Bonora, V. Barone, A. Bavoso, E. Benedetti, B. Di Blasio, P. Grimaldi, F. Lelj, V. Pavone, and C. Pedone.
Linear oligopeptides part 121: conformation of pleionomers of alpha-aminoisobutyric-acid.

Macromolecules **18**, 895–902 (1985).

[46] M. Crisma, F. Formaggio, A. Moretto, and C. Toniolo.
Peptide helices based on alpha-amino acids.
Biopolymers **84**, 3–12 (2006).

[47] P. Hamm, S. M. Ohline, and W. Zinth.
Vibrational cooling after ultrafast photoisomerization of azobenzene measured by femtosecond infrared spectroscopy.
J. Chem. Phys. **106**, 519–529 (1997).

[48] J. Bandekar.
Amide modes and protein conformation.
Biochim. Biophys. Acta **1120**, 123–143 (1992).

[49] A. Barth and C. Zscherp.
What vibrations tell us about proteins.
Q. Rev. Biophys. **35**, 369–430 (2002).

[50] J. Torres, A. Kukol, J. Goodman, and I. T. Arkin.
Site-specific examination of secondary structure and orientation determination in membrane proteins: the peptidic 13C=18O group as a novel infrared probe.
Biopolymers **59**, 396–401 (2001).

[51] E. H. G. Backus, P. H. Nguyen, V. Botan, R. Pfister, A. Moretto, M. Crisma, C. Toniolo, G. Stock, and P. Hamm.
Energy transport in peptide helices: a comparison between high- and low-energy excitations.
J. Phys. Chem. B **112**, 9091–9099 (2008).

[52] E. H. G. Backus, P. H. Nguyen, V. Botan, R. Pfister, A. Moretto, M. Crisma, C. Toniolo, O. Zerbe, G. Stock, and P. Hamm.
Structural flexibility of a helical peptide regulates vibrational energy transport properties.
J. Phys. Chem. B **112**, 15487–15492 (2008).

[53] D. R. Lide.
CRC Handbook of chemistry and physics, 75 ed.
CRC Press, Boca Raton FL (1994).

[54] Y. P. Touloukian, R. W. Powelland, C. Y. Ho, and M. C. Nicolaou.
Thermal physical properties of matter.
Plenum, New York (1978).

[55] A. Dhar.
Heat transport in low-dimensional systems.
Adv. Phys. **57**, 457–573 (2008).

[56] P. Anderson.
Absence of diffusion in certain random lattices.
Phys. Rev. **109**, 1492–1505 (1957).

[57] D. N. Payton III, M. Rich, and W. M. Visscher.
Lattice thermal conductivity in disordered harmonic and anharmonic crystal models.
Phys. Rev. **160**, 706–711 (1967).

[58] H. Furstenberg.
Noncommuting random products.
Trans. Am. Math. Soc. **108**, 377–428 (1963).

[59] S. T. Ariaratnam and W. C. Xie.
Wave localization in randomly disordered nearly periodic long continuous beams.
J. Sound Vib. **181**, 7–22 (1995).

[60] S. T. Ariaratnam and W. C. Xie.
Buckling mode localisation in randomly disordered continuous beams using a simplified model.
Chaos, Solitions & Fractals **8**, 1127–1144 (1996).

[61] V. Ambegaokar, B. I. Halperin, and J. S. Langer.
Hopping conductivity in disordered systems.
Phys. Rev. B **4**, 2612–2620 (1971).

[62] S. Lepri, R. Livi, and A. Politi.
Thermal conduction in classical low-dimensional lattices.
Phys. Rep. **15**, 015118 (2005).

[63] E. Fermi, J. Pasta, and S. Ulam.
Studies of nonlinear problems.
Los Alamos Rep. LA-1940, Pap. 266 pp. 491–501 (1955).

[64] N. J. Zabusky and M. D. Kruskal.
Interaction of solitons in a collisionless plasma and recurrence of initial states.
Phys. Rev. Lett. **15**, 240–243 (1965).

[65] R. Livi, M. Pettini, S. Ruffo, M. Sparpaglione, and A. Vulpiani.
Equipartition threshold in nonlinear large Hamiltonian systems: the Fermi-Pasta-Ulam model.
Phys. Rev. A **31**, 1039–1045 (1985).

[66] E. A. Jackson, J. R. Pasta, and J. F. Waters.
Thermal conductivity of one-dimensional lattices.
J. Comp. Phys. **2**, 207–227 (1968).

[67] S. Lepri, R. Livi, and A. Politi.
Thermal conduction in classical low-dimensional lattices.
Phys. Rep. **377**, 1–80 (2003).

[68] J. S. Wang.
Quantum thermal transport from classical molecular dynamics.
Phys. Rev. Lett. **99**, 160601 (2007).

[69] G. Stock.
Classical simulation of quantum energy flow in biomolecules.
Phys. Rev. Lett. **102**, 118301 (2009).

[70] J. L. Skinner and K. Park.
Calculating vibrational energy relaxation rates from classical molecular dynamics simulations: quantum correction factors for processes involving vibration-vibration energy transfer.
J. Phys. Chem. B **105**, 6716–6721 (2001).

[71] J. S. Bader and B. J. Berne.
Quantum and classical relaxation rates from classical simulations.
J. Chem. Phys. **100**, 8359–8366 (1994).

[72] D. Segal, A. Nitzan, and P. Hänggi.
Thermal conductance through molecular wires.
J. Chem. Phys. **119**, 6840–6855 (2003).

[73] R. Marquardt and M. Quack.
The wave packet motion and intramolecular vibrational redistribution in CHX3 molecules under infrared multiphoton excitation.
J. Chem. Phys. **95**, 4854–4876 (1991).

[74] A. Beil, D. Luckhaus, M. Quack, and J. Stohner.
Intramolecular vibrational redistribution and unimolecular reaction: concepts and new results on the femtosecond dynamics and statistics in CHBrClF.
Ber. Bunsenges. Phys. Chem. **101**, 311–328 (1997).

[75] P. Hamm and M. Zanni.
Concepts and methods of 2D infrared spectroscopy.
Cambridge University Press, New York (2011).

[76] H. Tal-Ezer and R. Kosloff.
An accurate and efficient scheme for propagating the time-dependent Schrödinger-equation.
J. Chem. Phys. **81**, 3967–3971 (1984).

[77] M. Bounouar and C. Scheurer.
Reducing the vibrational coupling network in N-methylacetamide as a model for ab initio infrared spectra computations of peptides.
Chem. Phys. **323**, 87–101 (2006).

[78] P. H. Nguyen, S. Park, and G. Stock.
Nonequilibrium molecular dynamics simulation of the energy transport through a peptide helix.
J. Chem. Phys. **132**, 025102 (2010).

[79] P. Hamm, R. A. Kaindl, and J. Stenger.
Noise suppression in femtosecond mid-infrared light sources.
J. Opt. Lett. **25**, 1798–1800 (2000).

[80] J. Piel, M. Beutter, and E. Riedle.
20-50-fs pulses tunable across the near infrared from a blue-pumped noncollinear parametric amplifier.
Opt. Lett. **25**, 180–182 (2000).

[81] E. Riedle, M. Beutter, S. Lochbrunner, J. Piel, S. Schenkl, S. Spörlein, and W. Zinth.
Generation of 10 to 50 fs pulses tunable through all of the visible and the NIR.
Appl. Phys. B **71**, 457–465 (2000).

[82] R. Bloem, S. Garrett-Roe, H. Strzalka, P. Hamm, and P. Donaldson.
Enhancing signal detection and completely eliminating scattering using quasi-phase-cycling in 2D IR experiments.
Opt. Express **18**, 27067–27078 (2010).

[83] R. Kopelent.
Early picosecond events in the bacteriorhodopsin photocycle.
Student Report, Inst. Phys. Chem., Univ. Zurich, unpublished (2009).

[84] K. Gundogdu, M. W. Nydegger, J. N. Bandaria, S. E. Hill, and C. M. Cheatum.
Vibrational relaxation of C-D stretching vibrations in CDCl3, CDBr3, and CDI3.
J. Chem. Phys. **125**, 174503 (2006).

[85] K. Kumar, L. E. Sinks, J. P. Wang, Y. S. Kim, and R. M. Hochstrasser.
Coupling between C-D and C=O motions using dual-frequency 2D IR photon echo spectroscopy.
Chem. Phys. Lett. **432**, 122–127 (2006).

[86] S. R. G. Naraharisetty, D. V. Kurochkin, and I. V. Rubtsov.
C-D Modes as structural reporters via dual-frequency 2DIR spectroscopy.
Chem. Phys. Lett. **437**, 262–266 (2007).

[87] M. W. Nydegger, W. Rock, and C. M. Cheatum.
2D IR Spectroscopy of the C-D stretching vibration of the deuterated formic acid dimer.
Phys. Chem. Chem. Phys. **13**, 6098–6104 (2011).

[88] J. K. Chin, R. Jimenez, and F. E. Romesberg.
Direct observation of protein vibrations by selective incorporation of spectroscopically observable carbon-deuterium bonds in cytochrome c.
J. Am. Chem. Soc. **123**, 2426–2427 (2001).

[89] L. B. Sagle, J. Zimmermann, P. E. Dawson, and F. E. Romesberg.
A high-resolution probe of protein folding.
J. Am. Chem. Soc. **126**, 3384–3385 (2004).

[90] J. Zimmermann, K. Gundogdu, M. E. Cremeens, J. N. Bandaria, G. T. Hwang, M. C. Thielges, C. M. Cheatum, and F. E. Romesberg.
Efforts toward developing probes of protein dynamics: vibrational dephasing and relaxation of carbon-deuterium stretching modes in deuterated leucine.
J. Phys. Chem. B **113**, 7991–7994 (2009).

[91] J. Zimmermann, M. C. Thielges, W. Yu, P. E. Dawson, and F. E. Romesberg.
Carbon-deuterium bonds as site-specific and non-perturbative probes for time-resolved studies of protein dynamics and folding.
J. Phys. Chem. Lett. **2**, 412–416 (2011).

[92] I. L. Karle and P. Balaram.
Structural characteristics of alpha-helical peptide molecules containing Aib residues.
Biochemistry **29**, 6747–6756 (1990).

[93] B. V. V. Prasad and P. Balaram.
The stereochemistry of peptides containing alpha-aminoisobutyric-acid.
CRC Crit. Rev. Biochem. **16**, 307–348 (1984).

[94] L. A. Carpino.
1-hydroxy-7-azabenzotriazole - An efficient peptide coupling additive.
J. Am. Chem. Soc. **115**, 4397–4398 (1993).

[95] M. Schade, A. Moretto, M. Crisma, C. Toniolo, and P. Hamm.

Vibrational energy transport in peptide helices after excitation of C-D modes in Leu-d10.
J. Phys. Chem. B **113**, 13393–13397 (2009).

[96] G. Valle, M. Crisma, C. Toniolo, R. Beisswenger, A. Rieker, and G. Jung.
1st observation of a helical peptide containing a chiral residue without a preferred screw sense.
J. Am. Chem. Soc. **111**, 6828–6833 (1989).

[97] C. Toniolo, A. Polese, F. Formaggio, M. Crisma, and J. Kamphuis.
Circular dichroism spectrum of a peptide 3(10)-helix.
J. Am. Chem. Soc. **118**, 2744–2745 (1996).

[98] G. C. Pimentel and A. McClellan.
The hydrogen bond.
Freeman, San Francisco (1960).

[99] T. Dahinten, J. Baier, and A. Seilmeier.
Vibrational energy transfer processes in dye molecules after ultrafast excitation of skeletal modes.
Chem. Phys. Lett. **232**, 239–245 (1998).

[100] C. Toniolo and E. Benedetti.
The polypeptide-3(10)-helix.
Trends Biochem. Sci. **16**, 350–353 (1991).

[101] M. Kobus, P. H. Nguyen, and G. Stock.
Coherent vibrational energy transfer along a peptide helix.
J. Chem. Phys. **134**, 124518 (2011).

[102] N. J. Halas.
Plasmonics: an emerging field fostered by Nano Letters.
Nano Lett. **10**, 3816–3822 (2010).

[103] D. Pissuwan, S. M. Valenzuela, and M. B. Cortie.
Therapeutic possibilities of plasmonically heated gold nanoparticles.
Trends Biotechnol. **24**, 62–67 (2006).

[104] L. R. Hirsch, R. J. Stafford, J. A. Bankson, S. R. Sershen, B. Rivera, R. E. Price, J. D. Hazle, N. J. Halas, and J. L. West.
Nanoshell-mediated near-infrared thermal therapy of tumors under magnetic resonance guidance.
Proc. Natl. Acad. Sci. USA **100**, 13549–13554 (2003).

[105] C. Loo, A. Lin, L. Hirsch, M. H. Lee, J. Barton, N. Halas, J. West, and R. Drezek.
Nanoshell-enabled photonics-based imaging and therapy of cancer.
Technol. Cancer Res. Treat. **3**, 33–40 (2004).

[106] D. P. O’Neal, L. R. Hirsch, N. J. Halas, J. D. Payne, and J. L. West.
Photo-thermal tumor ablation in mice using near infrared-absorbing nanoparticles.
Cancer Lett. **209**, 171–176 (2004).

[107] C. M. Pitsillides, E. K. Joe, X. Wei, R. R. Anderson, and C. P. Lin.
Selective cell targeting with light-absorbing microparticles and nanoparticles.
Biophys. J. **84**, 4023–4032 (2003).

[108] S. R. Sershen, S. L. Westcott, N. J. Halas, and J. L. West.
Temperature-sensitive polymer-nanoshell composites for photothermally modulated drug delivery.
J. Biomed. Mater. Res. **51**, 293–298 (2003).

[109] J. L. West and N. J. Halas.
Applications of nanotechnology to biotechnology.
Curr. Opin. Biotechnol. **11**, 215–217 (2000).

[110] A. G. Skirtach, A. A. Antipov, D. G. Shchukin, and G. B. Sukhorukov.
Remote activation of capsules containing Ag nanoparticles and IR dye by laser light.
Langmuir **20**, 6988–6992 (2004).

[111] B. Radt, T. A. Smith, and F. Caruso.
Optically addressable nanostructured capsules.
Adv. Mater. **16**, 2184–2189 (2004).

[112] A. S. Angelatos, B. Radt, and F. Caruso.
Light-responsive polyelectrolyte/gold nanoparticle microcapsules.
J. Phys. Chem. B **109**, 3071–3076 (2005).

[113] K. Kelly, E. Coronado, L. L. Zhao, and G. C. Schatz.
The optical properties of metal nanoparticles: the influence of size, shape, and dielectric environment.
J. Phys. Chem. B **107**, 668–677 (2003).

[114] S. Link and M. A. El-Sayed.
Size and temperature dependence of the plasmon absorption of colloidal gold nanoparticles.
J. Phys. Chem. B **103**, 4212–4217 (1999).

[115] M. Hu and G. V. Hartland.
Heat Dissipation for Au particles in aqueous solution: relaxation time versus size.
J. Phys. Chem. B **106**, 7029–7033 (2002).

[116] G. V. Hartland.
Measurements of the material properties of metal nanoparticles by time-resolved spectroscopy.
Phys. Chem. Chem. Phys. **6**, 5263–5274 (2004).

[117] J. Hodak, I. Martini, and G. V. Hartland.
Ultrafast study of electron-phonon coupling in colloidal gold particles.
Chem. Phys. Lett. **284**, 135–141 (1998).

[118] M. Perner, P. Bost, U. Lemmer, G. von Plessen, J. Feldmann, U. Becker, M. Mennig, M. Schmitt, and H. Schmidt.
Optically induced damping of the surface plasmon resonance in gold colloids.
Phys. Rev. Lett. **78**, 2192–2195 (1997).

[119] T. V. Shahbazyan, I. E. Perakis, and J. Y. Bigot.
Size-dependent surface plasmon dynamics in metal nanoparticles.
Phys. Rev. Lett. **81**, 3120–3123 (1998).

[120] T. S. Ahmadi, S. L. Logunov, and M. A. El-Sayed.
Picosecond dynamics of colloidal gold nanoparticles.
J. Phys. Chem. **100**, 8053–8056 (1996).

[121] C. Bauer, J. P. Abid, and H. H. Girault.
Size dependence investigations of hot electron cooling dynamics in metal/adsorbates nanoparticles.
Chem. Phys. **319**, 409–421 (2005).

[122] T. W. Roberti, B. A. Smith, and J. Z. Zhang.
Ultrafast electron dynamics at the liquid-metal interface: Femtosecond studies using surface plasmons in aqueous silver colloid.
J. Chem. Phys. **102**, 3860–3866 (1994).

[123] R. Pfister, J. Ihalainen, P. Hamm, and C. Kolano.
Synthesis, characterization and applicability of three isotope labeled azobenzene photoswitches.
Org. Biomol. Chem. **6**, 3508–3517 (2008).

[124] J. A. Carter, Z. Wang, H. Fujiwara, and D. D. Dlott.
Ultrafast excitation of molecular adsorbates on flash-heated gold surfaces.
J. Phys. Chem. A **113**, 12105–12114 (2009).

[125] P. D. Jadzinsky, G. Calero, C. J. Ackerson, D. A. Bushnell, and R. D. Kornberg.
Structure of a thiol monolayer-protected gold nanoparticle at 1.1 Å resolution.
Science **318**, 430–433 (2007).

[126] M. Schade, A. Moretto, P. M. Donaldson, C. Toniolo, and P. Hamm.
Vibrational energy transport through a capping layer of appropriately designed peptide helices over gold nanoparticles.
Nano Lett. **10**, 3057–3061 (2010).

[127] L. Fabris, S. Antonello, L. Armelao, R. L. Donkers, F. Polo, C. Toniolo, and F. Maran.
Gold nanoclusters protected by conformationally constrained peptides.
J. Am. Chem. Soc. **128**, 326–336 (2006).

[128] M. M. Alvarez, J. T. Khoury, T. G. Schaaff, M. N. Shafigullin, I. Vezmar, and R. L. Whetten.
Optical absorption spectra of nanocrystal gold molecules.
J. Phys. Chem. B **101**, 3706–3712 (1997).

[129] H. Susi and D. Byler.
Protein-structure by Fourier transform infrared spectroscopy 2nd derivative spectra.
Biochem. Biophys. Res. Commun. **115**, 391–397 (1983).

[130] H. S. Mandal and H. B. Kraatz.
Effect of the surface curvature on the secondary structure of peptides adsorbed on nanoparticles.
J. Am. Chem. Soc. **129**, 6356–6357 (2007).

[131] N. Matsuo, H. Muto, K. Miyajima, and F. Mafune.
Single laser pulse induced aggregation of gold nanoparticles.
Phys. Chem. Chem. Phys. **9**, 6027–6031 (2007).

[132] F. Mafune, J. Kohno, Y. Takeda, and T. Kondow.
Dissociation and aggregation of gold nanoparticles under laser irradiation.
J. Phys. Chem. B **105**, 9050–9056 (2001).

[133] A. Plech, V. Kotaidis, S. Gresillon, C. Dahmen, and G. von Plessen.
Laser-induced heating and melting of gold nanoparticles studied by time-resolved x-ray scattering.
Phys. Rev. B **70**, 195423 (2004).

[134] R. Levy, N. T. K. Thanh, R. C. Doty, I. Hussain, R. J. Nichols, D. J. Schiffrin, M. Brust, and D. G. Fernig.
Rational and combinatorial design of peptide capping ligands for gold nanoparticles.
J. Am. Chem. Soc. **126**, 10076–10084 (2004).

[135] R. Levy.
Peptide-capped gold nanoparticles: towards artificial proteins.
ChemBioChem **7**, 1141–1145 (2006).

[136] Y. Liu, M. K. Shipton, J. Ryan, E. D. Kaufman, S. Franzen, and D. L. Feldheim.
Synthesis, stability, and cellular internalization of gold nanoparticles containing mixed peptide-poly(ethylene glycol) monolayers.
Anal. Chem. **79**, 2221–2229 (2007).

[137] K. Sung, D. W. Mosley, B. R. Peelle, S. Zhang, and J. M. Jacobson.
Synthesis of monofunctionalized gold nanoparticles by Fmoc solid-phase reactions.
J. Am. Chem. Soc. **126**, 5064–5065 (2004).

[138] J. G. Worden, Q. Dai, A. W. Shaffer, and Q. Huo.
Monofunctional group-modified gold nanoparticles from solid phase synthesis approach: solid support and experimental condition effect.
Chem. Mater. **16**, 3746–3755 (2004).

[139] R. Levy.
A generic approach to monofunctionalized protein-like gold nanoparticles based on immobilized metal ion affinity chromatography.
ChemBioChem **7**, 592–594 (2006).

[140] Z. Ge, D. G. Cahill, and P. V. Braun.
AuPd metal nanoparticles as probes of nanoscale thermal transport in aqueous solution.
J. Phys. Chem. B **108**, 18870–18875 (2004).

[141] Z. Ge, Y. Kang, T. A. Taton, P. V. Braun, and D. G. Cahill.
Thermal transport in Au-core polymer-shell nanoparticles.
Nano Lett. **5**, 531–535 (2005).

[142] J. Alper and K. Hamad-Schifferli.
Effect of ligands on thermal dissipation from gold nanorods.
Langmuir **26**, 3786–3789 (2010).

[143] T. Nägele, R. Hoche, W. Zinth, and J. Wachtveitl.
Femtosecond photoisomerization of cis-azobenzene.
Chem. Phys. Lett. **272**, 489–495 (1997).

[144] Y. Tang, M. J. Grey, J. McKnight, A. G. Palmer, and D. P. Raleigh.
Multistate folding of the villin headpiece domain.
J. Mol. Biol. **355**, 1066–1077 (2006).

[145] S. H. Brewer, D. M. Vu, Y. Tang, Y. Li, S. Franzen, D. P. Raleigh, and R. B. Dyer.

Effect of modulating unfolded state structure on the folding kinetics of the villin headpiece subdomain.
Proc. Natl. Acad. Sci. USA **102**, 16662–16667 (2005).

[146] C. McKnight, P. Matsudaira, and P. Kim.
NMR structure of the 35-residue villin headpiece subdomain.
Nat. Struct. Biol. **4**, 180–184 (1997).

[147] T. K. Chiu, J. Kubelka, R. Herbst-Irmer, W. A. Eaton, J. Hofrichter, and D. R. Davies.
High-resolution x-ray crystal structures of the villin headpiece subdomain, an ultrafast folding protein.
Proc. Natl. Acad. Sci. USA **102**, 7517–7522 (2005).

[148] J. Kubelka, J. Hofrichter, and W. A. Eaton.
Experimental tests of villin subdomain folding simulations.
J. Mol. Biol. **329**, 625–630 (2003).

[149] J. Kubelka, J. Hofrichter, and W. A. Eaton.
The protein folding speed limit.
Curr. Opin. Struc. Biol. **14**, 76–88 (2004).

[150] S. H. Brewer, B. Song, D. P. Raleigh, and R. B. Dyer.
Residue specific resolution of protein folding dynamics using isotope-edited infrared temperature jump spectroscopy.
Biochemistry **46**, 3279–3285 (2007).

[151] S. Bagchi, C. Falvo, S. Mukamel, and R. M. Hochstrasser.
2D-IR experiments and simulations of the coupling between amide-I and ionizable side chains in proteins: Application to the villin headpiece.
J. Phys. Chem. B **113**, 11260–11273 (2009).

[152] D. C. Urbanek, D. Y. Vorobyev, A. L. Serrano, F. Gai, and R. M. Hochstrasser.
The two-dimensional vibrational echo of a nitrile probe of the villin HP35 protein.
J. Phys. Chem. Lett. **1**, 3311–3315 (2010).

[153] J. K. Chung, M. C. Thielges, and M. D. Fayer.
Dynamics of the folded and unfolded villin headpiece (HP35) measured with ultrafast 2D IR vibrational echo spectroscopy.
Proc. Natl. Acad. Sci. USA **108**, 3578–3583 (2011).

[154] Y. Duan and P. A. Kollman.
Pathways to a protein folding intermediate observed in a 1-microsecond simulation in aqueous solution.
Science **282**, 740–744 (1998).

[155] S. A. Islam, M. Karplus, and D. L. Weaver.
Application of the diffusion-collision model to the folding of three-helix bundle proteins.
J. Mol. Biol. **318**, 199–215 (2002).

[156] B. Zagrovic, C. D. Snow, M. R. Shirts, and V. S. Pande.
Simulation of folding of a small alpha-helical protein in atomistic detail using worldwide-distributed computing.
J. Mol. Biol. **323**, 927–937 (2002).

[157] A. Fernandez, M. Y. Shen, A. Colubri, T. R. Sosnick, R. S. Berry, and K. F. Freed.
Large-scale context in protein folding: villin headpiece.
Biochemistry **42**, 664–671 (2003).

[158] G. Srinivas and B. Bagchi.
Folding and unfolding of chicken villin headpiece: Energy landscape of a single-domain model protein.
Curr. Sci. **82**, 179–185 (2002).

[159] Z. Zhang, D. C. Burns, J. R. Kumita, O. S. Smart, and G. A. Woolley.
A water-soluble azobenzene cross-linker for photocontrol of peptide conformation.
Bioconjugate Chem. **14**, 824–829 (2003).

[160] D. C. Burns, F. Zhang, and G. A. Woolley.
Synthesis of 3,3'-bis(sulfonato)-4,4'-bis(chloroacetamido)azobenzene and cysteine cross-linking for photo-control of protein conformation and activity.
Nat. Protoc. **2**, 251–258 (2007).

[161] H. Mühlpfordt.
The preparation of colloidal gold particles using tannic acid as an additional reducing agent.
Experientia **9**, 1127–1128 (1982).

[162] N. J. Greenfield.
Using circular dichroism spectra to estimate protein secondary structure.
Nat. Protoc. **1**, 2876–2890 (2006).

[163] N. J. Greenfield.
Using circular dichroism collected as a function of temperature to determine the thermodynamics of protein unfolding and binding interactions.
Nat. Protoc. **1**, 2527–2534 (2006).

[164] R. Huang, L. Wu, D. McElheny, P. Bouř, A. Roy, and T. A. Keiderling.
Cross-strand coupling and site-specific unfolding thermodynamics of a Trpzip beta-hairpin peptide using 13C isotopic labeling and IR spectroscopy.
J. Phys. Chem. B **113**, 5661–5674 (2009).

[165] C. N. Pace, F. Vajdos, L. Fee, G. Grimsley, and T. Gray.
How to measure and predict the molar absorption coefficient of a protein.
Protein Sci. **4**, 2411–2423 (1995).

[166] N. A. Ciaccio and J. S. Laurence.
Effects of disulfide bond formation and protein helicity on the aggregation of activating transcription factor 5.
Mol. Pharm. **6**, 1205–1215 (2009).

[167] K. I. Oh, J. H. Lee, C. Joo, H. Han, and M. Cho.
Beta-azidoalanine as an IR probe: application to amyloid A-beta(16-22) aggregation.
J. Phys. Chem. B **112**, 10352–10357 (2008).

[168] H. Taskent-Sezgin, J. Chung, P. S. Banerjee, S. Nagarajan, R. B. Dyer, I. Carrico, and D. P. Raleigh.
Azidohomoalanine: a conformationally sensitive IR probe of protein folding, protein structure, and electrostatics.
Angew. Chem. Int. Ed. **49**, 7473–7475 (2010).

[169] G. D. Goodno, G. Dadusc, and R. J. D. Miller.
Ultrafast heterodyne-detected transient-grating spectroscopy using diffractive optics.
J. Opt. Soc. Am. B **15**, 1791–1794 (1998).

[170] P. M. Donaldson, H. Strzalka, and P. Hamm.
UV/visible pump, infrared probe experiments for challenging samples: transient gratings and heterodyne detection.
Abstracts of the fifteenth international conference on time-resolved vibrational spectroscopy (TRVS XV) (2011).

[171] F. Reif.
Statistische Physik und Theorie der Wärme, 2 ed.
Walter de Gruyter, Berlin, New York (1985).

[172] P. Hamm, J. Helbing, and J. Bredenbeck.
Stretched versus compressed exponential kinetics in alpha-helix folding.
Chem. Phys. **323**, 54–65 (2006).

[173] J. R. Kumita, O. S. Smart, and G. A. Woolley.
Photo-control of helix content in a short peptide.
Proc. Natl. Acad. Sci. USA **97**, 3803–3808 (2000).

[174] J. A. Ihalainen, B. Paoli, S. Muff, E. H. G. Backus, J. Bredenbeck, G. A. Woolley, A. Caflisch, and P. Hamm.
Alpha-helix folding in the presence of structural constraints.
Proc. Natl. Acad. Sci. USA **105**, 9588–9593 (2008).

[175] J. McCarthy, F. Hopwood, D. Oxley, M. Laver, A. Castagna, P. G. Righetti, K. Williams, and B. Herbert.
Carbamylation of proteins in 2-D electrophoresis - myth or reality?
J. Proteome Res. **2**, 239–242 (2003).

Acknowledgments

With this thesis difficult and challenging years in Switzerland are finally brought to an end. Many people have supported me through this time and contributed to the completion of this work in one or the other way. In the following I would like to thank some people explicitly:

Prof. Dr. Peter Hamm for giving me the opportunity to do my Ph.D. in his group and for letting me benefit from his experience and wide knowledge over laser spectroscopy and physics in general. I would also like to express my gratitude for the conditions he provided me when writing up this thesis under special circumstances.

Dr. Alessandro Moretto and Prof. Dr. Claudio Toniolo from the University of Padova for the fruitful collaboration on the 3_{10}-helix projects, the excellent samples and their expertise in peptide chemistry. Alessandro, furthermore, for his kind hospitality in Italy and the unforgettable tour through Venice.

Dr. Jan Helbing for sharing his expertise on ultrafast spectroscopy, all his critical remarks on my work and of course for the perfect conditions and all his help in Lab 1.

Rolf Pfister for all his effort on the synthesis and purification of the azobenzene-linked protein samples and also for the organization of the annual SOLA relay race.

Dr. Paul Donaldson for guiding me through the relevant literature on nanoparticles and for all his advice on the paper and the interpretation of the experimental data.

Dr. Sean Garrett-Roe for sitting next door and being an invaluable expert in all questions of science and English.

Shabir Hassan for the good teamwork on the nanoparticle-linked protein samples, many interesting discussions on the perspectives of the energy transport project and for his courage to continue the work on it.

Julien Réhault and Fivos Perakis for their help and the good collaboration in Lab 1 and for always being willing to share their measurement time. Please inform the student administration office that they can now exmatriculate me, the student ID I will recycle on my own.

Mateusz Donten for the help with the experiments on the students' setup and many interesting discussions on physical chemistry and cross-border politics.

My former office mate Mathias Ponmarin (by now Dr. Bonmarin) for the very motivating working atmosphere („nix funktion(n)iert“), the plant-growing competition, for building the French quality OPA and, most important, for saving us all from the swine flu.

My new office mates Halina Strzalka and Biplab Dutta, the guys from the office with the water connection Alexander Rodenberg and Robbert Bloem, and all the other current and former members of the Hamm group for the friendly and helpful working atmosphere. I will never forget all our great retreats and tours through Switzerland and the many long evenings we spent.

Dr. Ellen Backus for introducing me to the new project and for guiding me through the very first months of my Ph.D. work.

Rachel Helbling for her help with running calculations on the Matterhorn computer cluster.

Dr. Philipp Antoni and PD Dr. Bernhard Spingler from the institute of inorganic chemistry for providing access to and help with the CD spectrometer.

Maja Gossweiler for all her effort with the administration and of course for getting me the nice apartment in Höngg as a place to stay for the first months in Zurich.

Roland Zehnder and Herrn Kühne from the mechanics workshop as well as Martin Haller from the electronics workshop for solving all technical problems, and Sascha Giger for his computer support.

The graduate school of chemical and molecular sciences Zurich (CMSZH) for financial support, the monthly apéros and the annual retreats.

Finally, and most important, Maria for her patience and support over the last years and of course our son Eyvind for providing the final trigger for this thesis being completed.

Curriculum Vitae

First name:	Marco
Name:	Schade
Place and date of birth:	Homberg (Efze), Germany; April 26th, 1982
Citizenship:	German

Education and training:

2008-pres.	*Ph.D. Program in Physical Chemistry* Universität Zürich, Zürich, Switzerland
2002-2008	*Studies in Physics* Julius-Maximilians-Universität Würzburg, Würzburg, Germany *Diploma Thesis*: Time-resolved infrared spectroscopy and quantum control in the liquid phase Diploma in Physics (Dipl.-Phys.)
2005-2006	*Erasmus Exchange Program* Uppsala Universitet, Uppsala, Sweden *Research Project at Ångström Laboratory*: Industrial adaptation of coating technique for absorber surfaces in solar collectors
2001-2002	*Civilian Service* Burgfeld Krankenhaus, Kassel, Germany
2001	*Abitur* Geschwister-Scholl-Schule, Melsungen, Germany